Chair of Materials Physics

Doctoral Thesis

Implementation of femtosecond laser processing for materials testing and research

Dipl.-Ing. Manuel Pfeifenberger, BSc

August 2019

Part of this work (publication C) has been carried out within the framework of the EUROfusion Consortium and has received funding from the Euratom research and training programme 2014-2018 and 2019-2020 under grant agreement No 633053. The views and opinions expressed herein do not necessarily reflect those of the European Commission.

Erich Schmid Institute of Materials Science
Austrian Academy of Sciences
Jahnstrasse 12
A–8700 Leoben

This thesis was typeset by the use of KOMA-Script and LaTeX 2_ε.

Affidavit

I declare on oath that I wrote this thesis independently, did not use other than the specified sources and aids, and did not otherwise use any unauthorized aids.

I declare that I have read, understood, and complied with the guidelines of the senate of the Montanuniversität Leoben for "Good Scientific Practice".

Furthermore, I declare that the electronic and printed version of the submitted thesis are identical, both, formally and with regard to content.

Date 09.08.2019

Signature Author
Manuel Pfeifenberger
Matriculation Number: 00831365

Talente finden Lösungen,
Genies entdecken Probleme

Hans Krailsheimer

Danksagung

Zuallererst bedanke ich mich bei Prof. Dr. Reinhard Pippan für die Möglichkeit die Arbeit für meine Dissertation unter seinen Fittichen am Erich Schmid Institut durchzuführen. Ich danke ihm aufrichtig für die ausgezeichnete Betreuung, das mir entgegengebrachte Vertrauen und seine immerwährende Bereitschaft all meine Fragen zu beantworten. Beeindruckt von seiner Erfahrung, seiner Zuversicht und vor allem seiner Begeisterung beim Lösen ungeklärter Fragen, konnte ich in den letzten Jahren fachlich und überdies persönlich sehr viel lernen.

Ein weiterer großer Dank geht an Assoz. Prof. Dr. Daniel Kiener und an Dr. Anton Hohenwarter für die vielen Diskussionen, die Unterstützung bei fachlichen Fragen, die kreativen Einfälle bei neuen Experimenten und für die vielen Stunden des Korrekturlesens. Darüberhinaus waren mir die persönlichen Gespräche beim gemütlichen Beisammensein nach Feierabend immer ein ganz besonderer Genuss.

An meine Bürokollegen, Thomas, Karo, Alexander, die beiden Michaels, Vladislav und Stanislav richte ich einen ganz besonderen Dank für die vielen unterhaltsamen und mehr oder weniger tiefsinnigen Gespräche und den kurzweiligen Arbeitsalltag. Es war mir eine Freude, eine großartige Zeit bei diversen Feiern, auf Konferenzen und Reisen oder beim Mittagessen mit Benjamin, Vladica, Markus, Andrea, Daniela, Inas, Barbara, Megan, Reinhard, Bernhard, Andreas, Roland, Lisa, Stefan, Michael, Severin, Lukas, Christoph, Jakub, David und allen anderen Komplizen teilen und erleben zu dürfen. Ich bin sehr dankbar für die vielen Freundschaften, die während dieser Zeit enstanden sind.

Ich möchte mich bei allen Kollegen am Institut für die erstklassige Unterstützung bedanken, welche einen entscheidenden Teil zum Gelingen dieser Arbeit beigetragen hat. Im Besonderen gebührt großer Dank Daniela und Sabine für ihren meisterhaften Einsatz bei organisatorischen Themen. Auf Franz und Robin konnte ich immer zählen wenn ich wieder einmal Spezialanfertigungen benötigte. Gabi und Silke waren eine immense Hilfe bei unterschiedlichsten Fragen zur Probenpräparation. Meinem Laser-Kompagnon Alexander schulde ich vielen Dank für die großartige Unterstützung an der Auriga. Ich möchte mich bei allen für die angenehme und produktive Arbeitsatmospähre bedanken, die Zusammenarbeit war mir stets eine wahre Freude.

An all meine Freunde richte ich ein herzliches Dankeschön für den Support und die Freundschaft über all die Jahre hinweg. Zu guter Letzt danke ich meinen Eltern von ganzem Herzen für die allseitige Unterstützung und den beständigen Rückhalt, womit sie mein Studium und meine Dissertation erst ermöglichten. Vielen Dank!

Abstract

In the last two decades research on material processing using femtosecond lasers gained massive interest, due to its unique combination of properties - high material removal rates in addition to a minimized influence on the material surrounding the processing area. Particularly, for micro-processing this opens up a new world of possible applications.

The main focus of this thesis was the development of a novel system, which combines a scanning electron microscope, a focused ion beam and a femtosecond laser. This system is based on the Zeiss Auriga™ laser system, originally equipped with a nanosecond laser. After the successful adaption, it was used to investigate its potential for the processing of specimens in materials research, with an emphasis on the fabrication of specimens for mechanical experiments on the meso-scale. First, the processing of various types of materials, such as metals, polymers or biological materials, was evaluated. Critical parameters for the fabrication of micro-mechanical specimen geometries, regarding structural quality, geometrical precision and processing speed, were identified and an optimization of the laser processing parameters was conducted.

In detail, following studies were performed in which the newly developed system was applied to cutting-edge material research questions.

The resulting quality of specimens processed by a femtosecond laser and a nanosecond laser was compared by the fabrication of bending cantilevers in rolled tungsten foils. The specimen processed by the femtosecond laser yielded a higher surface quality and no grain coarsening underneath the processed surfaces as it was found for samples cut with the nanosecond laser. Especially, for the fabrication of specimens for mechanical tests on the scale of multiple hundred micrometer this negligible influence represents a significant advantage. Furthermore, the femtosecond laser processing parameters were optimized in terms of the efficiency. The advantage of the femtosecond laser compared to the focused ion beam technique is the high material removal rate and was demonstrated by the fabrication of a set of hundred cantilevers with a size of $420 \times 60 \times 25\,\mu\mathrm{m}^3$ in about 30 minutes, outperforming a conventional focused ion beam system by orders of magnitude.

The preparation of meso-scale tensile specimens from heat-sensitive materials by means of the femtosecond laser as well as the mechanical testing of the samples was successfully shown in two further studies. First, experiments on spruce wood displayed the potential of the technique to fabricate pristine biological specimens and to characterize local mechanical properties. Second, tensile experiments on three

different polymer foils allowed the local determination of strength and ductility, as well as the investigation of the influence of the femtosecond laser processing on these properties. In addition, these experiments were used to determine the effect of electron irradiation on the local tensile properties of the polymer foils. Finally, an approach for a depth-resolved measurement of tensile properties, was presented.

Furthermore, femtosecond laser processed single leg bending specimens enabled the measurement of the fracture toughness for intergranular crack growth in ultrafine grained tungsten materials. These experiments evaluated the crack growth resistance along the elongated microstructure of cold rolled tungsten foils with a thickness of 100 μm and cold drawn tungsten wires with a diameter of 150 μm. Such measurements have not been able to be performed so far with classical approaches. The fracture toughness found for the wires is 5.3 $\mathrm{MPa}\sqrt{\mathrm{m}}$. The foils yielded a significantly lower value of 2.4 $\mathrm{MPa}\sqrt{\mathrm{m}}$. This difference was linked to a distinct difference of the fracture surface roughness.

Contents

1

Motivation and aim of the work

In 1958 the concept of a *laser* (acronym for light ampilfication by stimulated emission of radiation) was proposed by Charles H. Townes and Arthur L. Schawlow [1], the acronym itself was coined a year before by Gordon Gould [2]. Soon after, in 1960, Theodore Maiman build the first laser [3], and back then he referred to it as a *"solution seeking a problem"* [4]. He knew at that time little about the impact lasers would have on future technologies. Since then a myriad of applications for various types of lasers have emerged.

In 2018 the basic principle of a special type of laser gained great attention. That year the Nobel prize in Physics was awarded to Arthur Ashkin, Gérard Mourou and Donna Strickland *"for groundbreaking inventions in the field of laser physics"* [5]. Gérard Mourou and Donna Strickland developed the method of chirped pulse amplification (CPA), to generate high-intensity, ultrashort pulses, laying the foundation of todays widespread use of ultrashort pulsed lasers [6]. The ability of these ultrashort pulsed lasers, to confine a high amount of energy to a defined volume of irradiated material with little to no effect on the surroundings, opens up a variety of ways to process or alter the material on a small scale. Soon after the development of these lasers this so called "cold ablation" found great interest in the material processing community and was seen as precursor for pushing the limits of precision in rapid fabrication on the micro-scale [7]. Nowadays ultrashort pulsed lasers already found commercial use in various applications e.g. fabrication of coronary stents, eye surgery (laser assisted in situ keratomileusis - LASIK), the micro-structuring of components in diesel injector systems [8] or the precision cutting of ultrathin glass for smartphone displays [9].

The ongoing miniaturization in the areas of micro-electro-mechanical systems (MEMS), small medical devices or microelectronics pose diverse challenges towards the technological advancements regarding functional materials. But, besides their functionality also the structural reliability of these products is of essential importance for any successful application. Mechanical properties are subject to significant change, when the material dimension is reduced to the length-scale of micrometers or below [10]. The need for understanding mechanical properties in this size regime is driving the development of methodologies, which enable their proper determination on the small scale. In the material research community respective investigations

made essential progress in the last decade, when the focused ion beam (FIB) technique became commercially available, as it represents a simple and variable method to produce mechanical samples on the nano- and micro-scale [11]. Nevertheless, due to its limited material removal rate the technique has two essential drawbacks: the maximum size of specimens and the number of specimens are constrained by the time a researcher is able to or can afford to spend on their preparation. This leads to limitations regarding the statistics of results or to a limitation on the sample dimensions for experiments investigating size effects. Hence, strategies for a faster preparation of samples on a larger scale and a rapid, site-specific pre-preparation are of great interest for the material science community.

This is where ultrashort pulsed lasers come into play. This technology represents an ideal candidate to tackle the issue of time-consuming sample preparation, due to its orders of magnitude higher material removal rate. Furthermore, it enables a localized processing on a small scale and it ideally has a negligible impact on the surrounding material. Additionally, ultrashort pulsed laser ablation is independent of the type of processed material, hence, the processing of metals, semiconductors or dielectrics is possible. However, the minimal processable feature size using a fs-laser is about 10 micrometers and is determined primarily by the minimum beam diameter at focus. Therefore, a FIB and an ultrashort pulsed laser ideally complement each other and a combination of both will open up new fabrication possibilities for applications in the fields of micro-mechanics and material characterization.

The aim of the present work was to develop a novel system, which exploits and combines the beneficial properties of an ultrashort pulsed laser and a focused ion beam. Based on the processing opportunities of this system possible contributions to the advancement of methodologies in the field of micro-mechanics were explored. Limitations and chances as well as an outline for potential future directions of this technique are discussed.

2 Introduction

Since the development of the first laser in 1960 [3], this technology has become essential in science and industry, covering a wide field of applications. Basically, lasers can be classified in different operation modes: the continuous wave mode and the pulsed mode, where the power output happens continuously or pulsed, respectively. Continuous wave lasers find use in processing applications, which are based on thermal impact, for instance melt cutting or welding [12]. Pulsed lasers provide a very high peak power intensity (e.g. up to few terawatt for femtosecond lasers [13]), which enables multiple ways of material alteration. Hence, upon their development particular interest for the use in material processing applications, especially using ultrashort pulsed lasers emerged [13]. Pulse durations vary over multiple orders of magnitude, from milliseconds down to the shortest pulse duration achieved in the laboratory so far in the low attosecond regime [14]. However, also commercially available laser sources operate already in the low femtosecond range. To illustrate the duration of such pulses: light travels at a speed of $3\times10^8\,\mathrm{m/s}$, hence, in one second a distance corresponding 7.5 times the length of the equator. In 100 femtoseconds it would cover a distance of only $30\,\mu\mathrm{m}$, about half the thickness of a human hair.

2.1 Pulsed laser technology

There exist multiple strategies to achieve certain durations of laser pulses. Common methods are - in decreasing order of achievable pulse duration - gain switching, quality switching (Q-switching) and mode locking [15]. Mode locking allows to produce laser pulses with a pulse duration in the ps- to fs-regime and is a suitable method for material processing applications as it provides an adequate trade-off between a satisfactorily pulse energy and a sufficiently high pulse repetition rate. The technique is based on the constructive interference of longitudinal modes with constant phase relationship in a laser resonator.

Pulses with pulse durations in the femtosecond regime exhibit the issue of exceeding the optical damage threshold of materials used for optical components, due to the high energy density of the pulses. Especially, for the components used for power

amplification of laser pulses this poses a severe problem. Therefore, the achievable pulse energy of ultrashort pulsed laser had been limited until the development of the CPA method in 1985. The CPA method alleviates the damaging issue by a temporally stretching of the pulses prior to the amplification and therefore lowering their energy density. Successively it is amplified and finally temporally compressed again. This temporal alteration of the pulses is achieved using optical gratings, which, depending on their dispersion, act as stretcher or compressor [6, 16]. The principle of the method is sketched in Fig. 2.1

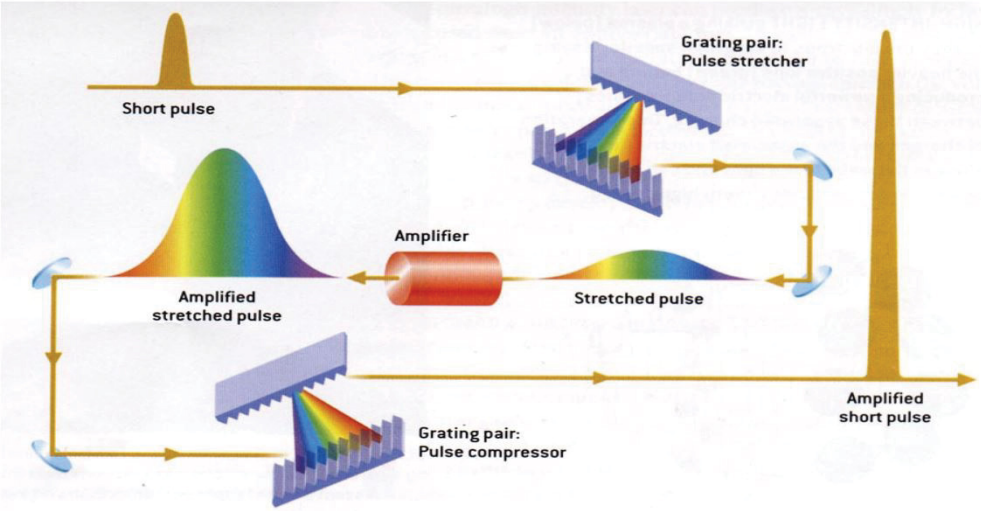

Figure 2.1 Principle of a chirped pulse amplifier. Figure taken from [17].

2.1.1 Important parameters for pulsed laser radiation

For further discussion important quantities and parameters for pulsed laser radiation need to be defined. The specifications of a pulsed laser usually include the average power P_{av} and the pulse duration t_p. Additionally, the pulse repetition rate R and the wavelength λ are essential parameters.

Starting from that information, the pulse energy E_p can be calculated via

$$E_p = \frac{P_{av}}{R} \tag{2.1}$$

Further, the peak power, P_{peak}, of a single pulse is defined by

$$P_{peak} = \frac{E_p}{t_p} \tag{2.2}$$

Most of the classifications and investigations on the interaction of ultrashort pulsed lasers with matter are presented in terms of the *fluence*, which corresponds to the energy density of the radiation. Typically the laser beam profile has a spatial Gaussian distribution of its intensity, although beam shaping techniques allow to provide other profiles like for example a rectangular tophat profile [12]. The description of such a Gaussian beam deviates significantly from geometrical optics approach and needs to be considered properly when configuring optical components.

Considering a laser beam diameter ω_0, which depicts the diameter, where the optical intensity of the Gaussian transverse profile of the laser beam drops to $1/e^2$ of the maximum value, the maximum fluence is calculated according to

$$F = \frac{E_p}{\frac{\pi\,\omega_0^2}{8}} \tag{2.3}$$

Commonly, the fluence values are presented in $\mathrm{J/cm^2}$. The pulses exhibit also a temporal Gaussian distribution.

2.2 Material interaction with ultrashort laser pulses

The extremely high energy density of the ultrashort laser pulses initiates various processes and mechanisms in different kinds of material, which are still not fully understood in all of their aspects. The interaction of a laser pulse is considered to be "non-thermal" for pulse durations below 1-10 ps [17]. The regime of this pulse durations is referred to as ultrashort (also sometimes ultrafast [8, 18]) pulse regime. For lasers with longer pulse durations or for continuous wave lasers thermal processes dominate the interaction with the material [17].

The description of the ultrashort pulsed laser-matter interaction for materials (especially metals) is mainly based on the two-temperature model [19], which treats the temperature evolution of the electron and the lattice system separately (the atomic/ionic system is referred to as lattice for crystalline and amorphous materials for simplicity).

Ultrashort laser pulses interact primarily with the electrons of the irradiated material, leading to an excitation of the electronic states. The fast thermalization of the electrons leads to an increased temperature of the system within the duration of the laser pulse. This temporary thermodynamic strong non-equilibrium between the electronic and the atomic system, triggers rapid heating due to the energy transfer from the electrons to atomic vibrations, which happens on the picosecond timescale [16]. This hyperthermal process leads to a rapid input of very high energy in a small volume, which is confined in a "cold" surrounding. Successively this high energy leads to a vaporization of the irradiated lattice ions before any energy is transferred

to the surrounding lattice [20]. Hence, the heat transfer into the remaining material can be neglected.

Other processes connected to this fast and high energy input are triggered on longer time-scales. For metals, for instance, thermal conduction due to phonon-phonon interaction starts around 100 ps [12]. Effects on the microstructure, solidification of melted material and surface morphology modifications start to happen after about 1 ns, therefore those processes are already completely decoupled from the initial pulse [18].

The consideration of the interaction of a ultrashort laser pulse with matter can primarily be separated into two classes of materials: interaction with opaque materials (e.g. *metals*) and interaction with transparent materials (e.g. *dielectrics*) [17, 18, 21].

In the case of metals the laser pulse energy is directly absorbed by the conduction band electrons. On the contrary, the energy of a single photon is generally not sufficient to excite electrons in semiconductors and dielectrics. First, the electrons need to be exited across the bandgap [18]. Hence, commonly wide-bandgap semiconductors and dielectrics are transparent in the wavelength range of visible light. Hence, for the high energy intensity of ultrashort pulsed laser light absorption occurs, due to non-linear optical coupling. The non-linear processes are multiphoton and avalanche ionization [21]. Therefore, the exposure of semiconductors and dielectrics to an ultrashort laser pulse leads initially to an electron excitation and therefore a high concentration of free electrons. This separation from the remnant positive charge in the surface layer of the solid leads to a high electric field strength near the surface. When the according repulsive electrostatic force exceeds the binding energy of the atoms, a Coulomb explosion - the emission of ions in the vicinity of the surface - occurs [17]. The high energy densities of ultrashort laser pulses can be used to modify materials, which are transparent for the laser wavelength. Using high enough pulse energies and focusing the laser beam inside a glass allows to confine the multiphoton absorption in the vicinity of the focal spot. This enables an internal modification of materials [12].

The interaction of laser light with matter also leads to the generation of X-ray and UV radiation for intensities above $10^{15}\,\mathrm{W/cm^2}$, which are achievable with ultrashort pulsed lasers [22]. Hence, an adequate shielding of the processing environment needs to be ensured.

2.2.1 Applications

The unique types of interaction of the ultrashort, high energy density laser pulses with matter lead to manifold applications. For example surface micro- or nanostructuring to control optical properties (e.g. black silicon, which yields a distinct reduction in reflectance; colouring of metals [23]) or wetting properties (e.g. to create superhydrophobic or superhydrophilic surfaces) [24]. Another application, laser

stereolithography, enables the fabrication of 3D microstructures by two-photon photopolymerization [16]. Furthermore, ultrashort lasers are used for internal processing of transparent materials, which, for instance, enables to directly write optical waveguides or other 3D optical micro-devices [16, 25].

The focus of the present work is, however, on the surface micro-processing and micro-structuring of materials, which will be contemplated in more detail in the following sections.

2.3 Ultrashort pulsed laser micro-processing - Fundamentals

Ultrashort pulsed lasers provide an ideal technique for surface micro-processing. The non-thermal ablation impedes the generation of a heat affected zone. Hence, ultrashort pulsed lasers enable high quality surface micro-processing with a good reproducibility [7, 26]. The small amount of heat also allows to process heat-sensitive materials, such as polymers or biological materials [27].

Material ablation occurs after a certain material dependent energy density threshold is exceeded. This value depends mainly on the reflectivity, the linear absorption coefficient and the thermal diffusivity of the material [21]. Therefore, each material exhibits a certain ablation threshold fluence F_{th}. For metals and dielectrics a linear dependence of F_{th} on the pulse duration exists, whereas no dependence on the pulse duration is found as long as it is in the ultrashort regime. Generally, F_{th} is higher for dielectrics, as initially energy is required to generate free electrons [28]. The processing atmosphere was found to influence F_{th} for several metals, being lower at atmospheric conditions compared to vacuum conditions. Exemplary values of F_{th}: copper 0.5-0.6 J/cm^2 (780 nm, vacuum), fused silica 1.2-1.5 J/cm^2 (526 nm, vacuum) [28].

Above this value ultrashort pulsed laser processing shows two typical ablation regimes, the low fluence and the high fluence regime. The fluence value of transition between those regimes F_{tr} is material dependent. These separated domains differ in the slope of the material removal rate with increasing fluence, as shown in Fig. 2.2 for various materials. For low fluence values above the ablation threshold the material removal rate increases slowly. A significant faster increase is observed above the transition fluence value F_{tr}. This behaviour was reported for metals, semiconductors and dielectrica [29, 30]. The surface quality of processed surfaces depends strongly on the fluence regime. Whereas surfaces processed in the low fluence regime yield a high quality, surfaces processed in the high fluence regime exhibit a thin layer of molten material [31] and extensive debris in the vicinity of the processed area [32, 33].

Studies of material alteration underneath femtosecond laser ablated surfaces revealed e.g. dislocation injection, recrystallization, phase changes or amorphization,

depending on the processed material. A possibility of reducing this damage is given by using a glancing incidence of the laser beam, hence, limiting the fluence during ablation to the low fluence regime [34]. In this low fluence regime the damage layer can be confined to a few hundred nm.

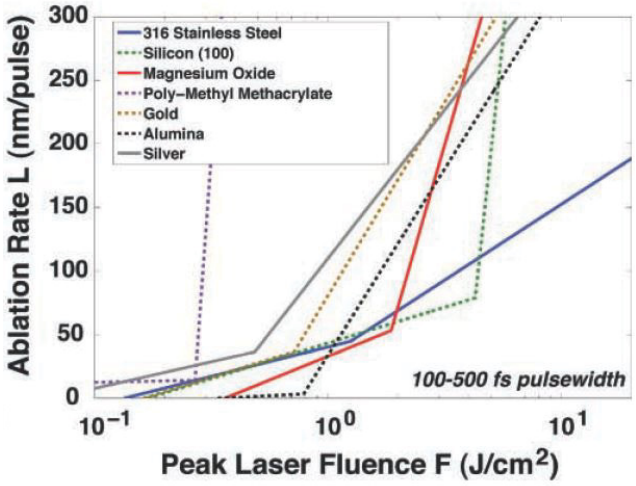

Figure 2.2 The material removal rate per pulse versus the laser fluence for the irradiation of various materials shows two different ablation regimes, which are typical for the processing of materials using ultrashort pulsed lasers. The low fluence regime allows a gentle material ablation, whereas above a material dependent threshold value in the high fluence regime the processed areas exhibit a decreasing quality. Graph taken from [35].

The ablation threshold is influenced by multiple processing parameters. Commonly this ablation threshold is determined by the onset of surface damage induced by a single laser pulse. Multiple-pulse irradiation was found to lead to a decrease of this value for metals and dielectrics [36–38]. However, above approximately 100 pulses the ablation threshold saturates. The decrease is attributed to the surface defect generation during the first pulses, which lead to a more efficient energy coupling.

The same applies to existing surface defects, like micropores or cracks, which lower locally the damage threshold [39] and therefore they act as initiation sites for further surface damage. Hence, assuming randomly distributed defects in a material matrix, also the area of irradiation (the beam spot diameter) has an effect on the ablation threshold. An increasing beam radius covers a larger number of defects, therefore, a decrease of the ablation threshold (F_{th}) value is found [39, 40].

The efficiency of ablation is influenced by the generated plasma or by ablated particles. In the sub-ns time regime plasma formation around the processed area occurs due to emitted surface electrons and ions. After several nanoseconds additionally a

plume consisting of vaporized target material is formed. For high repetition rates the plasma and the particles shield incoming pulses and lead to a reduction of the ablation efficiency [41, 42].

2.3.1 Heat accumulation

Material exposed to an ultrashort laser pulse is only ablated above a material dependent threshold fluence value, as depicted in Fig. 2.3. The remaining energy of the pulse is absorbed by the material without ablation [43]. This excessive energy leads to a heating of the surrounding material. In the case of high fluence values ($F > F_{tr}$) or high repetition rates this local heating induces subsequent melting of the material. Especially in the case of heat sensitive materials those two parameters (fluence and pulse repetition rate) need to be chosen carefully to avoid damage of the processed specimens due to the accumulation of heat. Also the fabricated geometry influences the amount of heat accumulation. For instance, the fabrication of holes with a high aspect ratio is distinctively sensitive regarding the processing parameters, due to the confined deposition of energy.

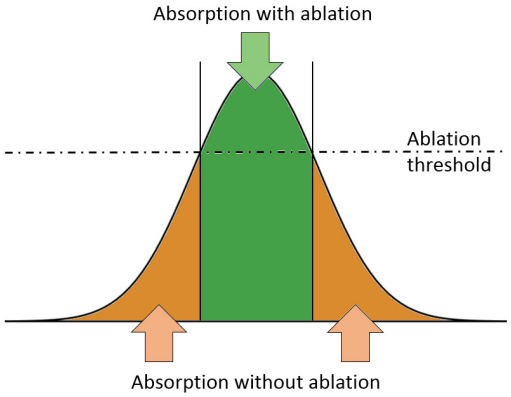

Figure 2.3 Sketch of the Gaussian spatial energy distribution of a single laser pulse. Ablation occurs above a material dependend threshold. The energy below that threshold is absorbed and leads to heating of the material. Adapted from [43]

Vorobyev *et al.* [44] showed that also for fs-laser material interaction this residual heat energy is not negligible. They found that for the single pulse irradiation of aluminium at atmospheric conditions, using fluence values well above the ablation threshold, up to 70 % of the incident laser pulse energy contributes to the heating of the material. The fluence and the ambient gas pressure were identified to be the main parameters determining the amount of thermal energy absorbed by the material after a single pulse irradiation. With higher ambient gas pressure a larger plasma is produced leading to an enhanced coupling of laser energy to the sample.

Thus, reducing the ambient gas pressure, while processing, reduced the residual thermal effect.

2.3.2 Laser induced periodic surface structures

Pulsed laser processing is also of high interest for surface nanostructuring, due to the formation of quasi-periodic structures upon irradiation. For this structures the term *laser induced periodic surface structures* (LIPSS) has been established [45]. These structures can be generated on almost any solid material using linearly polarized laser pulses [46]. Such periodic surface structures were already observed soon after the development of the first laser on surfaces of multiple semiconductors, which were exposed to laser radiation [47]. Interpulse feedback phenomena are responsible for the evolution of these LIPSS, when the surface is exhibited to multiple pulses [48].

Two types of LIPSS can be usually observed: structures with a spatial periodicity near to the radiation wavelength - *low spatial frequency* LIPSS (LSFL) and structures with a spatial periodicity significantly below the radiation wavelength - *high spatial frequency* LIPSS (HSFL) [48, 49]. The LSFL were explained by the interaction of the electro-magnetic field of the incident laser beam with surface scattered waves (surface plasmons) stemming from surface inhomogeneities. The origin of the HSFL is still under scientific debate [17, 46]. The appearance of the LIPSS is depending on the wavelength and the polarization of the radiation. The wavelength of the laser determines the period of the structures and the polarization dictates the orientation. The periodicity of the LSFL is approximately equal to the incident laser's wavelength and their orientation is typically perpendicular to the laser beam polarization [48, 49]. In addition, the fluence and the number of pulses have an influence on the formation of these structures. Long *et al.* [50] showed in a study on copper for a fluence of $0.43\,\mathrm{J/cm^2}$ that continuous periodic structures occur only above a certain accumulated number of laser pulses. Further, they identified a threshold fluence value, below which ripples were observed only on spatially separated areas. Milovanovic *et al.* [51] found a similar behaviour for steel and a titanium alloy. Additionally, the ambient pressure during processing has also been found to be an effective parameter to influence the appearance of the LIPSS [52]. With increasing pressure the spatial period of the structures decreases, whereas the depth increases.

2.3.3 Processing artefacts

Most of the fs-laser processed material is vaporized and partly redeposited as debris around the cutting region. The amount of this redeposited material is lower compared to processing using lasers with longer pulse durations above the ultrashort pulse regime [53]. Further, when the laser processing is conducted under vacuum

conditions the debris, redeposited in the vicinity of the processed area, is significantly reduced compared to atmospheric conditions [32, 54]. Regarding the ablation efficiency the generation of debris has a negative influence, as the redeposited material needs to be removed again.

A further challenge for certain applications of fs-laser fabrication is the evolution of a taper on processed surfaces. This taper develops due to the reduction of the energy density when the laser beam irradiates an inclined surface. The fluence of a laser beam incident on an inclined surface is reduced due to the elliptical distortion of the spot area. The area increases by the factor of $cos(\beta)$, where β is the angle of incidence. For an angle of $\beta = 80°$, this results in an approximately 6-fold decrease of the maximum fluence value [55]. Furthermore, energy is lost due to an increased reflectivity of the laser beam on the inclined surface compared to the case of perpendicular incidence [56]. Multiple strategies to reduce the taper of a processed surface, based on the variation of the incidence angle of the laser beam, exist and can be classified in two approaches: steering of the laser beam or adapting the position of the sample using a tilt-able stage.

The reduction of the fluence on inclined surfaces, which also correlates with a reduced ablation rate compared to horizontal surfaces, can lead to a phenomenon called preferential ablation [57], which means that areas perpendicular to the laser beam are removed faster than inclined areas, leading to the formation of so called cone-like structures. Pre-existing surface features or an agglomerate of ablated debris, which cause an adequate, local fluence reduction, will be ablated to a lower extent and can develop also into such cone structures [58]. The shape of these cones is ellipsoidal for linearly polarized laser light, because the reflectivity and, therefore, the amount of energy available for ablation, depends on the polarization of the laser light.

2.4 Ultrashort pulsed laser micro-processing - Applications

Besides the already mentioned commercial or industrial applications of the ultrashort pulsed laser processing technology (e.g. LASIK and the fabrication of injection nozzles in diesel engines) further applications, especially in research and development, were established. Examples are the fabrication of MEMS structures [59], microfluidic devices [25] or micro-lenses [12].

In the field of mechanical testing and especially micro-mechanical testing, applications of the femtosecond laser ablation for sample preparation only began to appear a few years ago. An exemplary usage depicts the introduction of sharp notches in macroscopic fracture specimens, mostly for either tensile fracture specimens [60, 61] or single edge V-notched beam samples [62, 63]. The fs-laser technique depicts a fast and optimal method for the introduction of a sharp notch for samples on the

macro-scale. Especially for brittle materials, which easily fracture during preparation, it is advantageous compared to established techniques, like cutting the notch using a razor blade or a diamond wheel. On top of that the fs-laser allows to produce notches with a smaller tip radius ($< 0.5\,\mu$m) [62, 63]. For certain materials such sharp tip radii are required for a proper evaluation of the fracture toughness. This was demonstrated e.g. for nanostructured tungsten alloys [63]. Further, it was shown for fine-grained alumina ceramic samples, that possible thermal stresses induced on the surface of the femtosecond laser cut notches have no effect on the fracture toughness [64].

Besides this application to macroscopic mechanical samples, also in the area of micro-mechanical testing few approaches were reported. Lim *et al.* [65] demonstrated a successful fabrication of cylindrical micropillars in bovine cortical bone by means of a femtosecond laser. Unfortunately, those specimens were not mechanically tested. Furthermore, such a processing of cylindrical structures on the micro-scale was also shown for metals [66]. Recently, mechanical tests on fs-laser processed micro-pillars were performed on rectangular single crystal copper pillars [67]. This study revealed an influence of the fs-laser processing on the flow-stress linked to an increase in dislocation density. Also the preparation of micro-mechanical tensile specimens using a fs-laser for metals, polymers and ceramics was demonstrated [68–70].

These promising studies showed the potential of the ultrashort pulsed laser technique for the fabrication of specimens in the size regime of few hundred μm and emphasize therefore the relevance of further research into this topic.

2.5 Femtosecond laser and focused ion beam - A winning team

In materials science the FIB technique is an established method for either, the preparation of local cross-sections for microstructural analyses, TEM sample preparation or for the fabrication of samples for micro- and nano-mechanical experiments [71–73].

A FIB allows a precise processing of various sample geometries for mechanical experiments down to the 100 nm range [74]. However, a drawback is the slow material removal rate (see Fig. 2.4), hence, the sample's size and the amount of samples feasible to fabricate is usually limited. An improvement in this regard is depicted by the plasma FIB (typically using xenon ions in commercially available devices). A plasma FIB provides a 2-3 orders of magnitude higher material removal rate [75]. Nevertheless, a comparison of the removal rate of a laser to the removal rate of a Ga^+ FIB and a plasma FIB, shows orders of magnitude higher values for the laser (see Fig. 2.4) [76, 77]. However, the achievable precision of the laser is lower due to a distinctly larger spot diameter (about 20 μm) compared to the FIB technique.

Therefore, the processable feature dimensions for the laser start in the 10 μm regime.

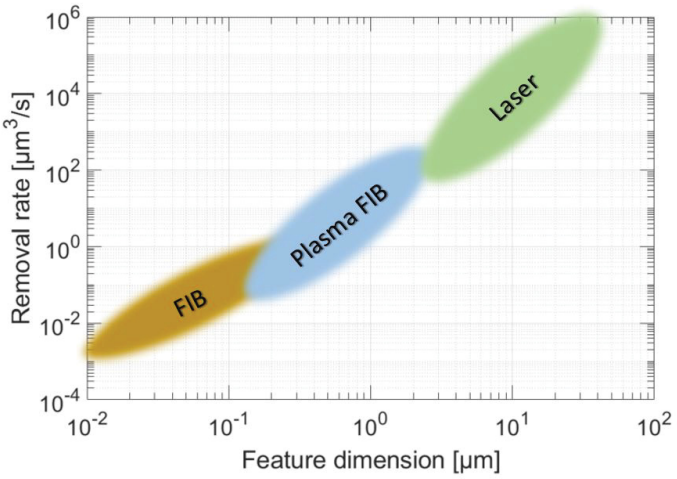

Figure 2.4 Comparison of the material removal rates of a gallium FIB, a xenon plasma FIB and a laser. The removal rates are plotted against the processable feature dimensions. Figure was adapted from [76].

Hence, a combination of both a fs-laser and a FIB yields the possibility for a fast material removal and a precise rework of regions of interest. A first prototype of that kind was developed in 2012 by Echlin *et al.* [35]. This device combined a scanning electron microscope (SEM), a FIB and a fs-laser in a single high vacuum chamber. Therefore, the setup is ideally suited for fast 3D material tomography. Nevertheless, since the fs-laser, the electron gun, the FIB gun and diverse detectors share the same chamber severe issues regarding contamination arise, because of the high amount of redeposit of ablated material. Additionally, geometries, where cut-off parts are produced, can not be fabricated in such a single chamber solution, due to the danger of damaging the turbo-pump.

Further, in other recent studies the combined application of a fs-laser and the FIB technique has found use (not necessarily combined in a single device). In [78] a procedure for the preparation of cylindrical samples for X-ray nano-CT is reported. Voisin *et al.* [79] developed a fabrication route for transmission electron microscopy (TEM) samples directly from bulk materials. Lavenstein *et al.* [80] fabricated micro-cantilever specimens for high frequency fatigue testing using a combined approach of fs-laser and FIB processing.

Finally, it needs to be stated that FIB processing influences the processed material as well. It can lead to defects in the near-surface layer due to implantation of gallium ions [71, 81]. Especially for mechanical experiments on the micro-scale this ion damage has a significant effect on the results [82]. Compression experiments on

polycrystalline aluminium using micro-pillars fabricated using a plasma FIB suggest a reduced influence of the xenon ions on the yield strength compared to specimens fabricated using gallium ions [83].

3
Summary of the results

A description of the newly developed system combining a fs-laser and a FIB and a summary of the experiments utilizing this system are presented here. In section 3.1 a brief introduction of the system setup is given. The findings on process parameter optimizations regarding sample quality are outlined subsequently. In sections 3.3 and 3.4 successful application-studies of the system are presented. First, applications of the fs-laser as preparation technique for material characterization and as pre-preparation method for following FIB milling are discussed. Finally, examples of fs-laser fabricated samples for mechanical experiments on the meso-scale are shown and results of respective experiments are presented and discussed.

3.1 System setup

The novel system at the Erich Schmid Institute is based on the Auriga nanosecond laser system (Zeiss, Oberkochen, Germany). The setup is displayed in Fig. 3.1 and its single constituents are indicated. It consists of 2 vacuum chambers. The large main chamber (Fig. 3.1a) contains the SEM and the FIB column. The laser processing is performed in the small chamber (Fig. 3.1b). These two chambers are separated via an airlock. In the small chamber medium vacuum conditions of about 7×10^{-3} mbar prevail, whereas the turbopump attached to the main chamber enables a high vacuum of about 1×10^{-6} mbar.

The originally equipped ns-laser was substituted by an ultrashort pulsed laser (Origami 10 XP™, Onefive GmbH, Regensdorf, Switzerland). The specifications of the fs-laser unit are summarized in Tab. 3.1. The available wavelengths for processing are 515 and 1030 nm. The third wavelength of 343 nm cannot be used in the present setup as certain optical components only have an anti-reflective coating for the other two wavelength. The average output power is not constant for different pulse repetition rates. For the wavelength of 515 nm, which is the one primarily used, the maximum available average output power is at 100 kHz. Therefore, this value is listed in the table for both wavelengths. Other specifications of the system are listed in Tab. 3.2. The system allows to adjust the following process parameters: average power, repetition rate, scan speed and the focal height.

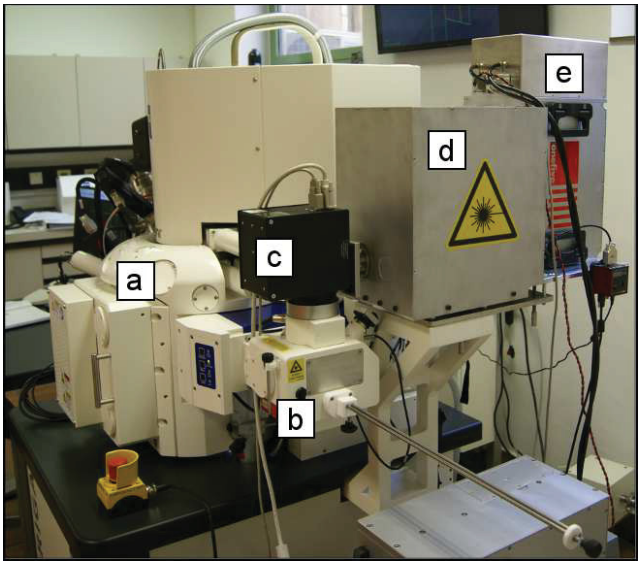

Figure 3.1 Setup of the newly developed system: (a) Main chamber containing the SEM and FIB gun, (b) laser processing chamber, (c) galvano scan head, (d) optical unit and (e) femtosecond laser unit. Figure is taken from the appended *publication A*.

The laser pulses are generated in the femtosecond laser unit (see Fig. 3.1e). Successively the laser beam passes the optical unit (Fig. 3.1d and in detail in Fig. 3.2). The beam expander (Fig. 3.2c) consists of a dispersive and a collective lens, functioning similar to an inverse Galilean telescope. The distance between those lenses determines the distance of the focal spot with respect to the final objective, hence, the height of processing with respect to the sample holder in the laser chamber. The variation of the distance between the lenses is realized using a stepper motor. After the beam expander the laser beam proceeds to a galvanometer scanner (Fig. 3.1c). This scan head consist of two perpendicular oriented, rotatable mirrors (Fig. 3.2d), which have a special anti-reflective coating for wavelengths at 515 and 1030 nm.

Feature	Unit	
Wavelengths	[nm]	1030, 515, (343)
Pulse duration	[fs]	< 500
Max. pulse repetition rate	[MHz]	1
Pulse energy variance	[%]	0.93
Average output power of 1030 nm at 100 kHz	[W]	4.1
Average output power of 515 nm at 100 kHz	[W]	2.1

Table 3.1 Specifications of the integrated fs-laser unit Origami 10 XP™.

These mirrors allow to move the laser beam laterally in the X and Y direction in the processing chamber. Following to the scanhead a f-theta objective (Fig. 3.2e) is used to focus the beam on a flat focal plane. Finally, the laser beam passes an about 12 mm thick entrance window on top of the processing chamber, which allows the evacuation of the chamber. The observation of the sample holder's position and the cutting process is conducted by means of an UsB camera, located on the backside of the laser chamber.

The exit windows for different wavelengths of the laser unit are located on different heights (see Fig. 3.2). Therefore, a periscope with special mirrors for ultrashort pulsed lasers is used to guide the laser beam with 1030 nm into the same path of the laser beam as for 515 nm. The lower mirror of this periscope is fixed on a flip mount, hence, allowing a fast removal and re-positioning with high accuracy.

The optical components along the beam path have a limited transmissivity or reflectivity, hence, the laser pulses lose a certain amount of power along their way to the sample surface. A thermopile sensor (Coherent FieldMaxII-Top™) was used to determine this energy loss. Measurements of different pulse energies directly after the laser unit were compared to respective measurements in the laser chamber after passing all optical components. In the ideal case a total transmissivity of 62% was found for the wavelength of 515 nm.

Feature	Unit	
Scan speed	[mm/s]	> 1
Size of scan field	[mm×mm]	50×50
Diameter of focal spot	[μm]	$\approx$25
Focal height variation	[mm]	$\approx$20

Table 3.2 Specifications of the fs-laser system.

The positioning of the fs-laser cuts on the sample is realized using a special specimen holder. This holder contains 4 apertures. In the SEM mode the region of interest on the sample is captured and the relative position to the apertures is determined and saved. After transferring the sample holder into the laser processing chamber, the 4 apertures are located above 4 photodiodes. This photodiodes register a signal when the laser scans across the aperture hole. By knowing the position of the apertures, the relative position of the region of interest can be loaded into a CAD program, which then allows to position and to define the scan patterns for the laser processing. This approach allows an absolute positioning accuracy of about 20 μm. The galvo-scan head itself allows a relative positioning accuracy of about 1 μm.

The two separated vacuum chambers of the system setup yield critical advantages. First of all, due to the high material removal rate of the fs-laser a high volume of

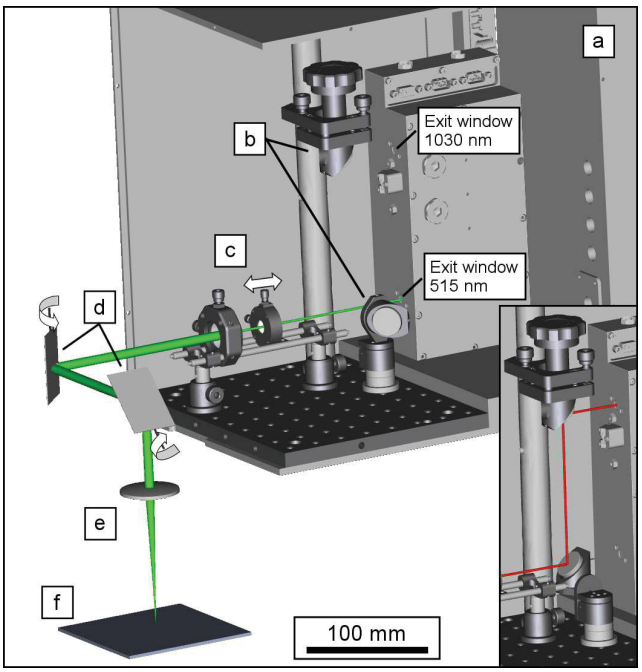

Figure 3.2 Detailed sketch of the optical unit: (a) Laser unit with the two exit windows for the laser with 515 nm and the 1030 nm wavelength located on different heights, (b) periscope with flipable, lower mirror mount, (c) beam expander to vary the focal height (d) mirrors of the galvano scan head, which enable the lateral movement of the laser spot, (e) f-θ objective to focus the laser beam onto the flat sample surface independent of the lateral position (f) sample surface. Figure is taken from the appended *publication A*.

ablated material is distributed as debris in the laser processing chamber. Hence, the airlock avoids any contamination of the main chamber. However, the debris also coats the entrance window of the laser as well as the cover glass of the UsB camera. Especially the debris on the entrance window can lead to a significant power-loss of the laser pulses. Therefore, those components need to be cleaned on a regular basis.

In addition to the protection against contamination this separation also enables to process samples under other atmospheric conditions, for example under non-evacuated or under noble gas atmospheres. This can particularly be advantageous for biological materials, where an exposure to vacuum can yield unwanted impact on the material.

3.2 Processing quality - Essential considerations

The quality of fs-laser processed structures is significantly influenced by the selection of the processing parameters. Especially, the fluence, repetition rate and the scan speed determine the condition of the result. Furthermore, the scanning route plays an essential role in terms of re-deposition.

3.2.1 Heat accumulation

The heat accumulation is primarily caused by the excess energy of each pulse, which is not used for ablation. Particularly for materials with a low heat conductivity, the time between pulses, defined by the pulse repetition rate, determines the processing quality. Hence, for a potential fast fabrication of structures in such materials the maximum pulse repetition rate avoiding damage needs to be determined.

An evaluation of optimal parameters for a high quality processing of three different kinds of polymer foils: a 25 μm thick Upilex-S foil, a 127 μm thick fluorinated ethylene propylene (FEP) foil and a 127 μm thick polyethylene terephthalate (PET) foil, was conducted. For this rectangular cuts were fabricated using a fluence of 1.18 J/cm^2, a scan speed of 2 mm/s and a wavelength of 515 nm. The amount of laser pulses, hence, the total energy input, was kept constant for each cut by using decreasing pulse repetition rates (50, 25, 10, 5, 1 kHz) with accordingly increasing number of scan repetitions (1, 5, 10, 25, 50). This resulted in a respective increase in the processing duration, varying from 1.5 s to 75 s.

Exemplarily, Fig. 3.3 shows SEM details of the upper and lower edge of the rectangular cuts with decreasing pulse repetition rates from 50 kHz (Fig. 3.3a) to 1 kHz (Fig. 3.3e). For 50 and 25 kHz massive melting and the formation of cracks was found up to a distance of 200 μm around the processed area. For 10 kHz no cracks but still a thin molten layer is evident on the upper edge. The two cuts with a repetition rate of 5 and 1 kHz exhibited a smooth and clean cutting surface. The behaviour of the PET foil was similar. However, here only the cut performed with 1 kHz displayed a sufficient quality. On the contrary, the FEP foil did not show cracks or molten structures even for 50 kHz, but exhibited the formation of debris to a greater extend. Also the material removal rate was found to be lower. Therefore, higher scan repetition numbers were required to cut through the 127 μm thick foil. Only the cut processed with 1 kHz and 50 scan repetitions yielded a continuous cut.

A similar result was found for the processing of single line cuts in thin slices of spruce wood using a fluence of 0.72 J/cm^2 and a scan speed of 1 mm/s. For repetition rates above 5 kHz massive damage and carbonization of the material was observed. However, a repetition rate around 1 kHz yielded clean cuts, with no damage observable under a light microscope.

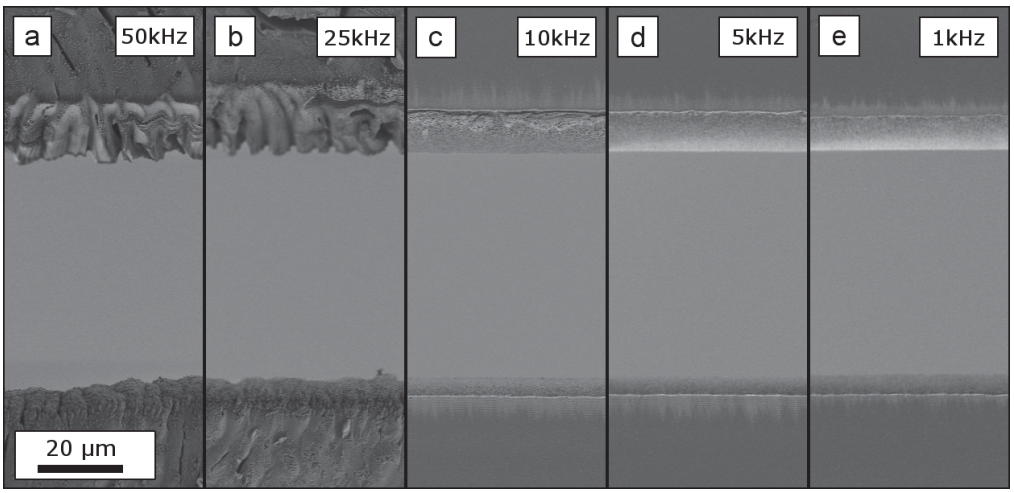

Figure 3.3 Upper and lower edge of a rectangular cut in a Upilex-S foil with a thickness of 25μm. Due to heat accumulation the formation of cracks, a molten layer and rough cut surfaces is found for high repetition rates (a),(b),(c). For lower repetition rates (d) and (e) well defined cuts with minimal debris are observed. The scale bar indicated in the lower left applies for all figures. Figure is taken from the appended *publication B*.

3.2.2 Re-deposition of ablated material

Fs-laser processing leads to the formation of a significant amount of debris, due to the high volume material removal. This redeposited material consists primarily of rapidly cooled nanoparticles.

Cutting under non-evacuated conditions increases the amount of debris, especially in the vicinity of the processed region. This can be explained by the reduced mean free path of each particle under atmospheric conditions compared to medium vacuum conditions of about 10^{-3} mbar. The redeposited nanoparticles and agglomerates are loosely bonded with the surface and can therefore be widely removed in an ultrasonic bath. Particularly, if soap water is used a considerably good removal is observed.

Besides reducing the surface quality, redeposited material can lower the machining efficiency and also effect the final structure of laser processed specimen geometries. The redeposition of the ablated material can be influenced by the scanning strategy of the laser beam. An example is given in Fig. 3.4. Two rectangular cuts at the edge of a W foil with a thickness of 25 μm are displayed. For this the laser beam was scanned in rows towards the upper edge of the cut (as sketched in Fig. 3.4a). First, a single-pass scanning strategy was used i.e. each line was scanned right to left 20 times and then shifted up for 8 μm. The ablated material is extensively redeposited on the lower edge of the cut (see Fig. 3.4b), nearly covering the whole process area again. Second, a multipass scanning strategy was performed, where each line was

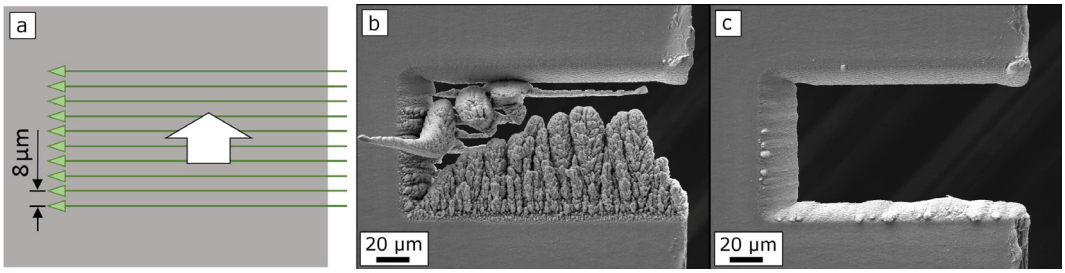

Figure 3.4 Evaluation of rectangle cuts in a W foil with a thickness of 25 μm with regard to redeposit. (a) Scan pattern for the two examples shown in (b) and (c). 10 parallel lines (green arrows), each scanned from right to left, are successively scanned towards the upper edge (indicated by the white broad arrow). (b) Single-pass scanning leads to a distinctively higher amount of redeposit compared to (c) multi-pass scanning. Figures are taken from the appended *publication A*.

scanned 5 times and the whole pattern was repeated 4 times, thus, keeping the total energy input the same as before. A significantly lower amount of redeposited material was observed in this case (see Fig. 3.4c). This multi-pass approach is also a common strategy for reducing redeposit when structuring materials using a FIB [84].

This demonstrates the importance of a proper scanning strategy when the fs-laser is utilized for an efficient fabrication of e.g. micro-mechanical specimens.

3.2.3 Laser induced periodic surface structures

For certain applications, especially the preparation of smooth cross-sections, LIPSS are an unwanted feature, as the increased surface roughness impedes most analyses on the micro-scale. For example LIPSS lead to a distinct reduction of the image quality of electron backscatter diffraction (EBSD) scans, which can impede a proper data acquisition particularly for fine grained materials. Hence, their avoidance is of interest for diverse investigations.

An investigation on the capabilities of the fs-laser for the processing of high-quality cross-sections for further analyses was conducted. For this trenches were cut into the edge area of copper samples (as sketched in Fig. 3.5), enabling a fast characterization in the SEM. Prior to the fs-laser processing the surfaces of the samples were mechanically and electrolytically polished. The trenches were cut by scanning the laser beam along 10 parallel lines covering a rectangle with a dimension of $300 \times 50\,\mu m^2$ (see Fig. 3.5a).

A dependence of the initial LIPSS generation on the amount of fs-laser pulses impacting the sample surface was reported for scans with perpendicular laser beam incidence [50]. A parameter variation revealed a similar correlation of the amount of

the number of laser pulses and the resulting surface quality for the fabrication of the trenches. For a more detailed evaluation and quantification of the LIPSS formation a new parameter was introduced - the pulses per spot (PPS). The PPS describe the accumulated number of pulses, which impact on a single spot in the processed area. To calculate this number, we require the distance a_p between each laser pulse striking the surface when scanning the laser beam with a scan speed S and a pulse repetition rate R_p

$$a_p = \frac{S}{R_p} \tag{3.1}$$

The PPS can then be calculated as follows

$$PPS = n_{sr} \frac{D}{a_p} \frac{D}{a_l} \tag{3.2}$$

where n_{sr} is the number of scan repetitions, D is the focal diameter and a_l is the distance between the parallel scanning lines.

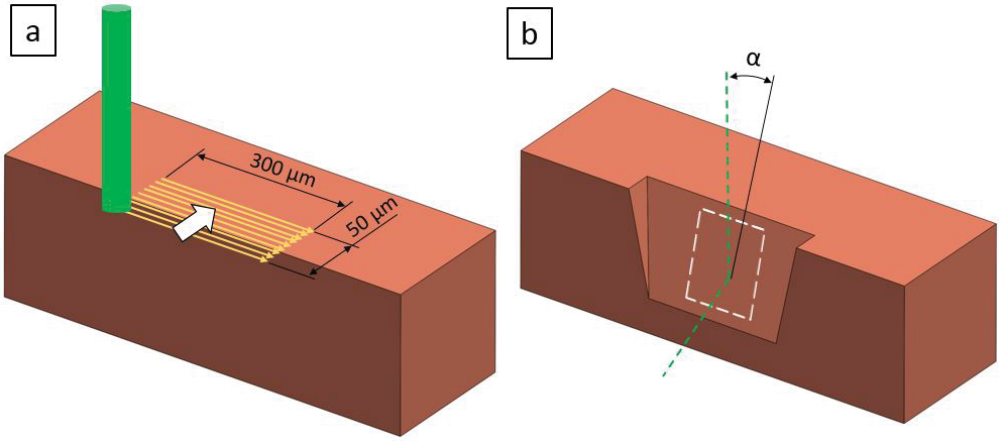

Figure 3.5 Processing of trenches for fs-laser parameter investigations. (a) The scanning route consists of 10 parallel lines, each shifted a distance of 5 μm in the direction of the broad arrow. The direction of incidence of the laser beam is indicated. (b) The resulting trenches show a parameter dependent taper angle α. The surface of the trench wall was evaluated regarding its quality using the SEM. The respective position of the micrographs in Fig. 3.6 is indicated by the dashed rectangle.

In Fig. 3.6 SEM micrographs of the trench surface are shown. The first LIPSS start to form between 18.75 kPPS and 25 kPPS. For further increasing PPS values LIPSS are observed on an increasing part of the area until for 62.5 the whole area is covered. Hence, to achieve the best surface quality the PPS need to be kept below a certain, material dependent threshold.

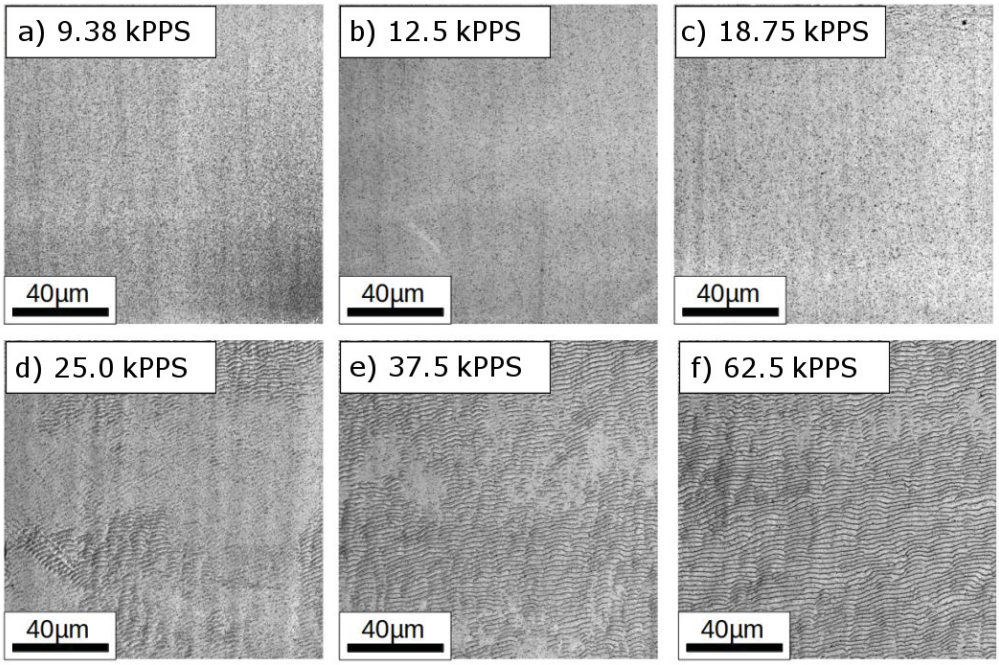

Figure 3.6 SEM-micrographs of the surface of the trenches cut in a copper sample using a fs-laser. The process parameters were: a fluence of 1.26 J/cm^2, 1 mm/s scan speed, 1 kHz pulse repetition rate and a focal diameter of 25 μm. LIPSS start to evolve with increasing number of pulses per spot (PPS). Figure taken from [85].

3.2.4 Taper

The walls of the trenches cut into the copper samples exhibited a significant taper. Therefore, additionally to the surface quality an evaluation of the inclination angle of the trench walls was performed. Profiles of the trenches were recorded in the centre of the trench using a confocal laser scanning microscope. The results are displayed in Fig. 3.7. The zero-point corresponds to the upper edge of the trench. With increasing PPS a decrease of the taper angle was found, which is expected as more material is removed with each scan repetition. The taper angle α starts to saturate at a certain value of PPS. This saturated angle is determined mainly by the fluence value and the material. The higher the fluence the smaller α will be. The saturation occurs when the fluence at the sample surface does not suffice any more to exceed the ablation threshold of the present material. This reduction in fluence does have two reasons: i) due to the inclined surface the spot is not a circle but a strongly pronounced ellipse, hence, the larger irradiated area reduces the fluence is reduced; ii) the inclined surface also leads to an increase in the reflectivity, therefore, a smaller amount of the energy is available for the ablation.

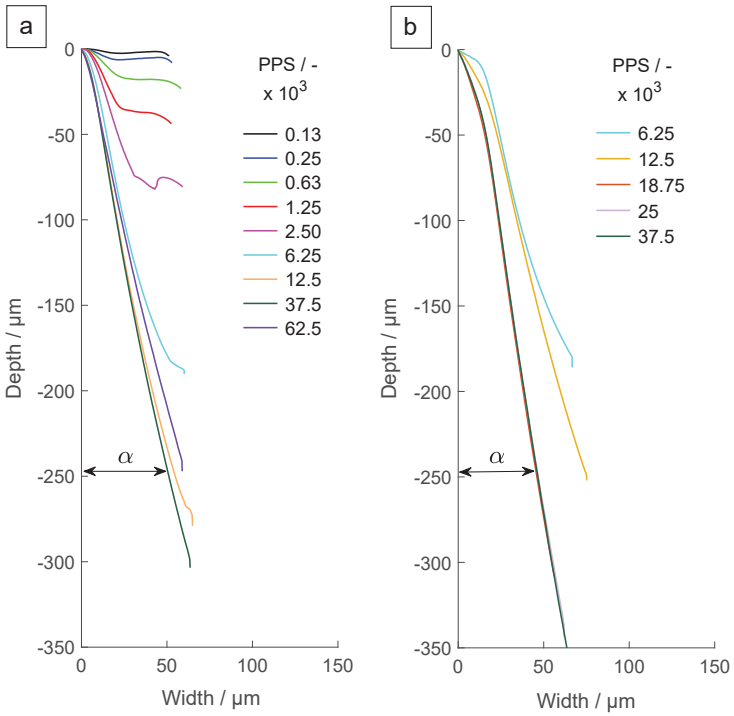

Figure 3.7 Profiles of trenches shown for increasing PPS values and a fluence of (a) $0.98\,\mathrm{J/cm^2}$ and (b) $2.62\,\mathrm{J/cm^2}$. Increasing PPS values exhibit a decrease in the taper angle. In (a) the angle starts to saturate to a value of about $\alpha = 10.4°$ around 10×10^3 PPS. In (b) the saturation leads to a final angle $\alpha = 8.7°$ begins at about 15×10^3 PPS. The curves for 18.75, 25 and 37.5 kPPS overlap.

As presented in the previous subsection the avoidance of LIPSS requires the reduction of the PPS. Hence, if in addition to a LIPSS free surface a small taper angle is needed, a compromise is required to be made. For the achievement of taper and LIPSS free surfaces the sample needs to be tilted to the minimum taper angle, which can be processed without LIPSS formation. This task is not straight-forward as prior knowledge about both features is required beforehand.

Furthermore, it was found that for the investigated trench geometry, reflections off the side-walls can lead to an additional material removal along the reflected beam path. This is displayed in Fig. 3.8. As a result, for the preparation of cross-sections for analyses, which require a defect free surface, a large enough width should be ensured to obtain an unaffected area in the middle of the trench.

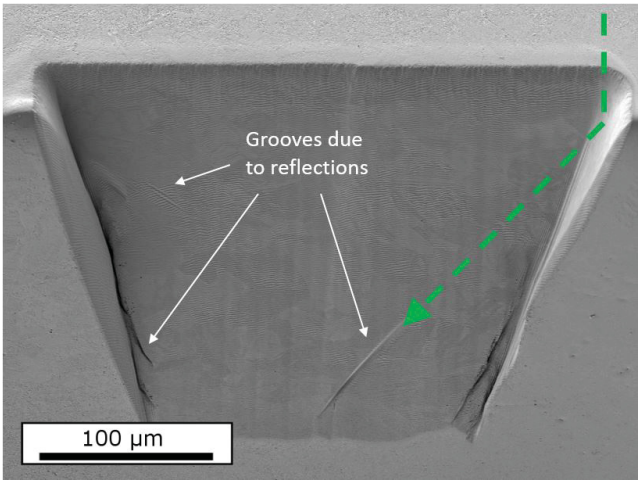

Figure 3.8 Reflections off the side-walls of the trench can lead to the formation of grooves, showing that a significant amount of the incident pulse energy is not used for ablation if the laser beam strikes an inclined surface. For an arbitrary groove the path of a reflected laser beam is indicated. Figure adapted from [85].

3.3 Femtosecond laser processing as pre-preparation technique

The developed fs-laser system is an ideal tool for pre-preparation of specific sites on a specimen for further FIB processing or other analyses used for material characterization, like e.g. EBSD. The combined SEM allows to precisely locate and image a determined region of interest for the fabrication of a cross-section. In addition an essential advantage of the fs-laser processing is its universal material ablation capability. Hence, the processing of cross-sections in multilayer materials is possible, as long as the ablation threshold of all included materials is exceeded.

As example for a site specific micro-processing the preparation of cross-sections on nanoindentation buckles is shown in Fig. 3.9. The investigated material is a silicon wafer with a thin film system consisting of 800 nm borophosphosilicate glass, 400 nm silicon nitride and 300 nm tungsten-titanium. Residual compressive stresses in the W-Ti film lead to the formation of buckles after a nanoindentation induced delamination. The buckles exhibited dimensions up to 80 μm in diameter. This implies that the fabrication of multiple cross-sections, to investigate any deformation and fracture of film and substrate, using the FIB is a time consuming task. Utilizing the fs-laser to remove material prior to the FIB milling, significantly reduces the total processing time.

Fig. 3.9 shows the combined processing route. For each cross-section, first, a

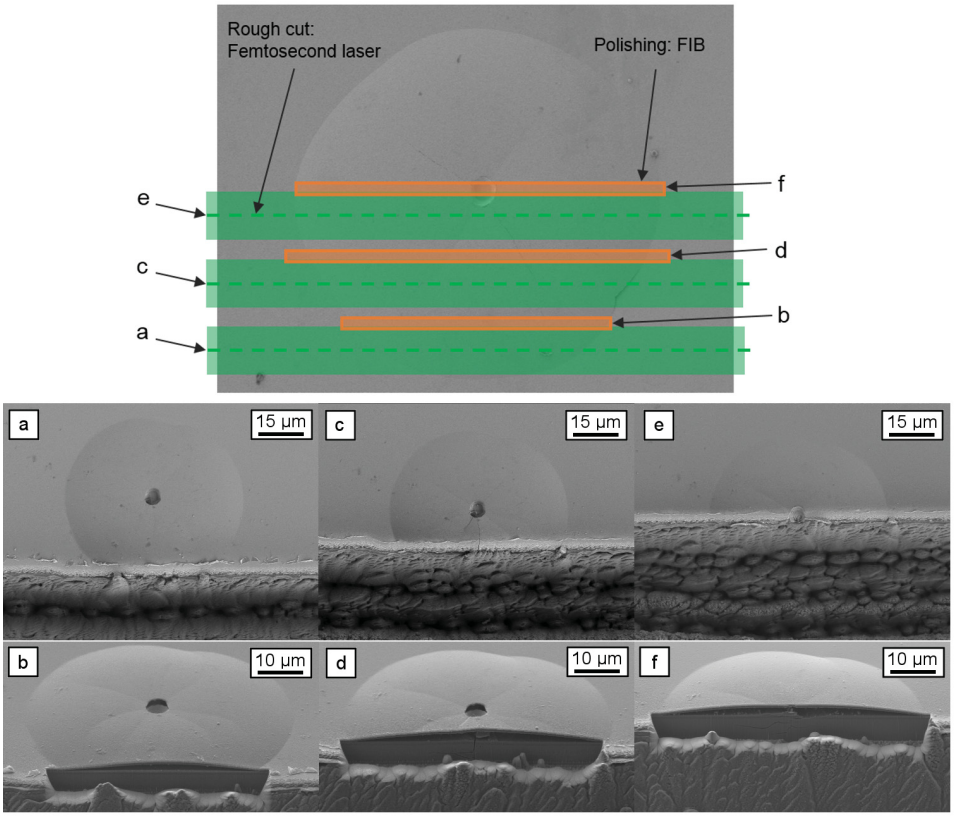

Figure 3.9 Processing route for cross-sections of large indentation buckles using the fs-laser and the FIB. (a), (c) and (e) display the fs-laser cuts in top view. (b), (d) and (f) show the successive FIB cross-sections, which allow to evaluate any delamination and fracture of the thin film system, in a tilted view. Figure is taken from *publication D*.

150 μm long, single line was cut with the fs-laser (indicated by the green rectangle). The laser parameters were a fluence of 0.52 J/cm^2 and a pulse repetition rate of 1 kHz. The beam was scanned with a speed of 1 mm/s for 60 passes, which corresponds to a processing time of about 10 s. Fig. 3.9(a,c,e) displays three laser cuts approaching the centre of a buckle from a top view. Successively the FIB cross-section was processed on the edge of the laser groove (indicated by the orange rectangle). The FIB polishing was conducted with a beam current of 2 nA and an acceleration voltage of 30 kV. In Fig. 3.9(b,d,f) the results of the successive FIB polishing steps are given in a tilted view, revealing details of any delamination or fracture of the thin film system.

The presented method was also used for the rapid preparation of cross-sections of buckles, occurring after scratch testing experiments. Further details on these

experiments can be found in *publications D* and *F*.

Besides this site-specific pre-preparation of cross-sections, the preparation of wedges for X-ray nanodiffration analyses [86] or for further FIB processing depicts an ideal field of application of the fs-laser ablation. Especially for brittle materials or hard coatings, conventional grinding is extremely demanding. Hard coatings delaminate easily and thin wedges of brittle materials are fragile and therefore impede handling for further investigations. Fig. 3.10a shows a 150 μm thick slice of silicon with a locally thinned area, which was fabricated via fs-laser processing. This wedge acted as precursor for further FIB processing of micro-scale fracture cantilevers (see Fig. 3.10b).

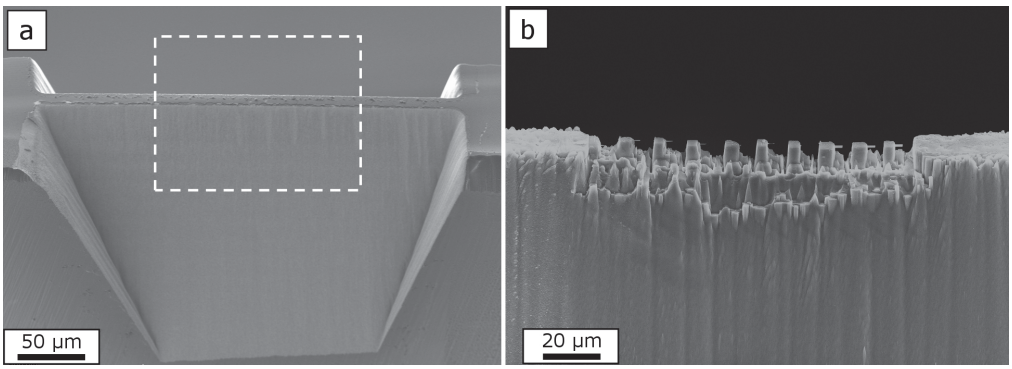

Figure 3.10 Locally thinning of a silicon sample using a fs-laser for further FIB processing. (a) The specimen thickness was initially thinned down to 150 μm by means of conventional grinding. The fs-laser enabled a further reduction of the thickness down to 10 μm at the top surface. (b) Bending cantilevers cut via FIB into the area indicated by the dashed rectangle in (a).

3.4 Femtosecond laser fabrication of mechanical samples on the meso-scale

The high material removal rate and the low influence on the material surrounding process zone do provide optimal prerequirements for the preparation of samples for successive FIB processing. In addition, the fs-laser represents an ideal method for the fabrication of mechanical samples on the meso-scale without any post-processing. Furthermore, the fs-laser allows to investigate materials, where such samples can not be processed on this scale using other methods. The possibility of a rapid fabrication of such small samples enables a high resolution mapping of mechanical properties. In the following sections studies on different specimen geometries and materials are presented.

3.4.1 Bending cantilever specimens

Initially, the capabilities of the new femtosecond laser system and the original nanosecond laser system were compared for the processing of mechanical specimens. The specimens of choice for this investigation were bending cantilevers.

The cantilevers were cut out of cold rolled tungsten foils with thicknesses of 25, 50 and 100 μm. Tungsten has a very low sputter rate for FIB processing [84], thus, the fabrication of mechanical samples is limited to dimensions of a few μm [87]. This is an issue if one aims for a proper aspect ratio of the cantilevers (length to height ratio of ideally $\approx$5:1). The bending cantilevers were fabricated with dimensions of about $420 \times 60 \times 25\,(50,\,100)\,\mu\text{m}^3$.

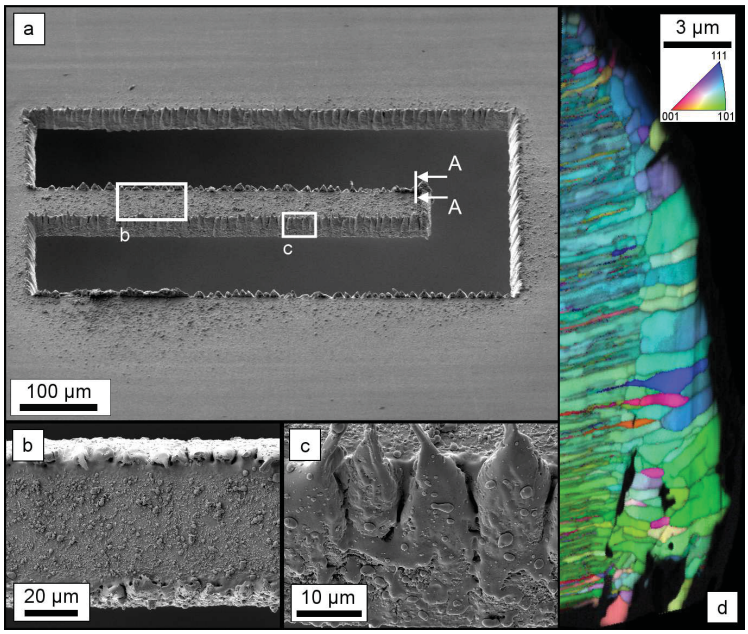

Figure 3.11 (a) Cantilever cut into a cold rolled tungsten foil with a thickness of 25 μm by means of a ns-laser. The locations of the details (b) and (c) and the FIB polished cross-section (d) are indicated. (b) On the top surface of the cantilever extensive debris was observed. (c) Additionally, the processed surfaces exhibited distinct molten structures. (d) An EBSD orientation map of the cross-section A-A at the tip of a cantilever shows grain coarsening up to 4 μm underneath the surface. Figure is taken from the appended *publication A*.

Fig. 3.11 and Fig. 3.12 show a cantilever cut with a nanosecond laser and a femtosecond laser respectively. The specimen cut with the nanosecond laser showed a large amount of debris on the top surface (see Fig. 3.11b). Furthermore, a distinct molten layer on the processed surface as well as a pronounced burr was found

(see Fig. 3.11c). Regarding mechanical tests those features can lead to a non-ideal contact between the loading element and the cantilever. A different behaviour was observed for samples cut via the femtosecond laser. A well-defined geometry was achieved and on the top surface less debris was found (see Fig. 3.12b). Additionally, on the processed surfaces only LIPSS were visible (see Fig. 3.11c).

Besides the surface quality a different extent of material modification was found underneath the processed surface. The heat produced during the nanosecond laser processing lead to a coarsening of the initially lamellar microstructure. An EBSD analysis revealed a layer of coarsened, equiaxed grains. This coarsening was found up to 4 μm underneath the processed surface (see Fig. 3.11d). On the contrary, the same analysis performed on a fs-laser processed specimen exhibited no grain coarsening (see Fig. 3.12b).

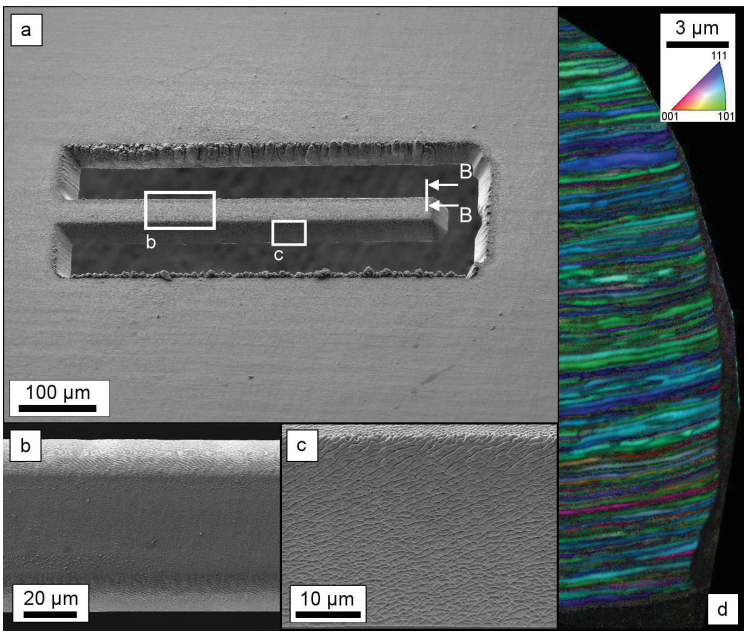

Figure 3.12 (a) Cantilever cut into a cold rolled tungsten foil with a thickness of 25 μm by means of a fs-laser. The locations of the details (b) and (c) and the FIB polished cross-section (d) are indicated. The cantilevers showed a well defined structure, (b) less debris on their top surface and (c) no molten features on the processed surface, instead the typical LIPSS could be observed. (d) An EBSD analysis revealed no grain coarsening for these samples on the FIB polished cross-section B-B. Figure is taken from the appended *publication A*.

To utilize these cantilevers for experiments evaluating the fracture toughness an introduction of sharp notches is required. The processing of the notches for macroscopic fracture samples using the fs-laser was already successfully applied (see Sec. 2.4). However, for the thickness of the presented cantilevers the fs-laser is not

suitable for the introduction of a notch. A single line cut exhibits for a small number of beam passes, and therefore small depths ($< 1/2$ spot size), a round profile (i.e. a blunt notch). With increasing number of beam passes and accordingly increasing depths, the cross-section of a single line groove evolves a profile with a sharper tip [88]. Thus, the introduction of relatively sharp notches for fracture mechanics specimens will only be reasonable starting from a notch depth larger than the spot size ($\approx 25\,\mu$m). Therefore, for the fabrication of notches with a minimal tip radius ($\approx 10\,$nm [89]) the FIB is still the method of choice.

A demonstration of the speed of the fs-laser processing was performed by cutting an array of 100 cantilever into a W foil with a thickness of $25\,\mu$m. This array was fabricated in about half of an hour. However, here the focus was put on a fast fabrication, rather than on the achievement of the best quality. Nevertheless, removing the same amount of material using the FIB takes about one and a half year of continuous milling, when assuming a relatively high material removal rate of $10\,\mu\text{m}^3/s$.

Details on the preparation of bending cantilevers in cold rolled tungsten foils can be found in the *publication A*.

3.4.2 Tensile specimens

Tensile experiments on metals, polymers and ceramics using fs-laser fabricated specimens were already reported [68–70]. However, the influence of the laser processing, especially on heat sensitive materials still requires further investigations. The present work contributes experiments in this regard on spruce wood and three different kinds of polymer foils. On the one hand, these experiments demonstrate the wide applicability of the fs-laser processing in terms of different material classes. On the other hand, these experiments demonstrate the broadening of the field of applicability of the developed system compared to the original Auriga ns-laser system. Replacing the ns-laser with the fs-laser enables to ablate these heat-sensitive materials as well as optical transparent materials. The original equipped ns-laser inhibits a defined processing of this material classes, due to the significantly higher amount of thermal impact of each single pulse. Biological materials as well as polymers show a severe influence on their structural integrity, due to heat damage. However, also the fs-laser processing can lead to a severe degradation, if the wrong parameters are chosen (see Sec. 3.2.1).

Furthermore, the ns-laser did not allow a processing of materials, which are optically transparent for the wavelength of the laser. Contrary to that, due to multiphoton ionization, a femtosecond laser enables the processing of such materials. This was demonstrated by the processing of the polymer foils, which are highly transparent for the used wavelength of 515 nm.

Polymer foils

Three types of polymer foils were investigated: Polymide Upilex-S with a thickness of 25.4 μm thickness, PET (Polyethylene terephthalate) with 127 μm and FEP (Fluorinated ethylene propylene) with 127 μm. The Upilex-S and FEP foils were coated with a vapour deposited aluminium (VDA) thin film with 100 nm thickness on one side. The PET foil was uncoated.

Two subjects were investigated in these experiments. First, an evaluation of proper process parameters for a well defined fabrication of tensile samples for the three types of polymer foils was performed. The influence of the fs-laser fabrication on the mechanical properties of the polymer foils was determined. Secondly, the tensile specimens were utilized to evaluate the influence of electron beam irradiation on the materials. This influence is of special interest for the FEP VDA and the Upilex-S VDA foils, which are commonly used as multilayer heat insulation of spacecraft. In space various types of irradiation lead to a degradation of the structural integrity of components. Hence, the understanding of this process is of prime interest for future developments in space science. Additionally to the heat insulation polymer foils, PET foils were investigated, because their tensile properties are situated in the middle range between the high ultimate tensile strength (of about 500 MPa) of the Upilex-S foils and the high ultimate tensile strain (of about 350%) of the FEP foils.

The evaluation of the optimal parameters, especially regarding the heat accumulation, was already outlined in section 3.2.1. The parameters used for the fabrication of the samples were optimized with regard towards the disappearance of flaws on the sample surface and to reasonable processing times.

Compared to macroscopic tensile experiments the micro-tensile samples yielded similar results for the Upilex-S VDA and the PET samples. The FEP VDA samples exhibited a comparable yield strength but did not show the characteristic strain hardening at about 200% strain, which is commonly observed for macroscopic specimens. This suggests that the responsible mechanisms leading to strain hardening are affected by the fs-laser processing.

Besides the heat accumulation it was found that the laser processing atmosphere plays a critical role, especially for the fabrication of the FEP VDA samples. Particularly, the FEP VDA samples were severely impacted. Fig. 3.13 shows a comparison of tensile curves of FEP VDA samples processed with different fs-laser fluences under vacuum and under atmospheric conditions. It could be observed, that the ultimate tensile strain decreased significantly with increasing fluence when the samples are fabricated under atmospheric conditions. However, also for vacuum conditions a lower value was found for the maximum fluence value compared to the optimized value. Besides the reduced ultimate tensile strength this is a further indication that the FEP VDA material was effected by the fs-laser processing. For FEP an influence of the exposure environment on the amount of degradation was also reported

for other types of irradiation. The effect was associated mainly with a higher yield of polymer chain scission when irradiated in air [90].

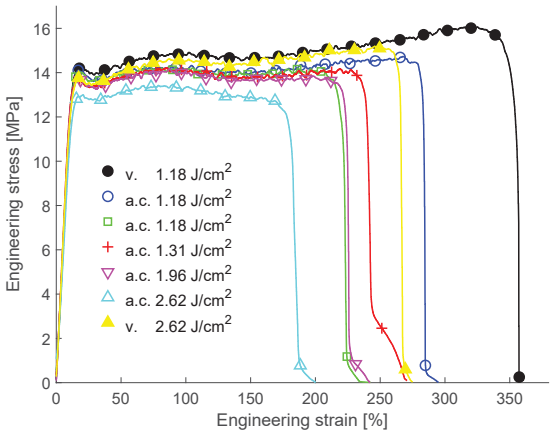

Figure 3.13 FEP VDA samples exhibited a severe degradation of the ultimate tensile strain with increasing fluence when processed under atmospheric conditions. Also for processing under vacuum conditions a decrease of the ultimate tensile strain was found, however, to a smaller extent compared to the atmospheric conditions. Figure is taken from the appended *publication B*.

The Upilex-S VDA and the PET samples did not exhibit any degradation in terms of the tensile properties when processed under non-vacuum conditions and with increasing fluence values (see Fig. 3.14a and b). Even for the highest fluence values similar ultimate tensile strain and strength values were reached. In summary, the fs-laser processed tensile samples showed a good reproducibility of the results for constant process parameters.

Successively, this micro-tensile samples processed with optimized laser parameters were used to determine the influence of electron irradiation on the ductility and strength of the polymer foils. The Upilex-S VDA samples did not exhibit a degradation of their tensile properties for electron irradiation doses up to 1 MGy. The tensile properties of the PET samples yielded a distinct orientation dependence for non-irradiated specimens. This is related to the fabrication procedure and commonly referred to as transverse direction (TD) and machine direction (MD). The electron irradiation yielded a slight reduction of the yield strength and for both orientations a decrease in the ultimate tensile strength and ultimate tensile strain was found (see Fig. 3.15a). The FEP VDA specimens were severely degraded already upon a electron irradiation of 250 kGy. The ultimate tensile strain of the irradiated specimens was less than 20% of the ultimate tensile strain of the non-irradiated specimens (see Fig. 3.15b). Furthermore, the yield strength exhibited an increased variation for the irradiated samples.

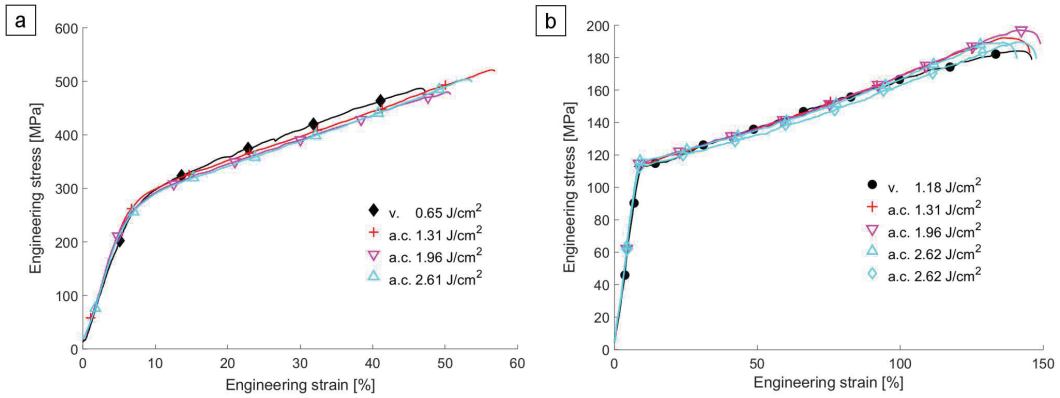

Figure 3.14 (a) Upilex-S VDA samples and (b) PET samples fabricated under atmospheric conditions with increasing fluence values did not show an effect on the tensile properties. Figure is taken from the appended *publication B*.

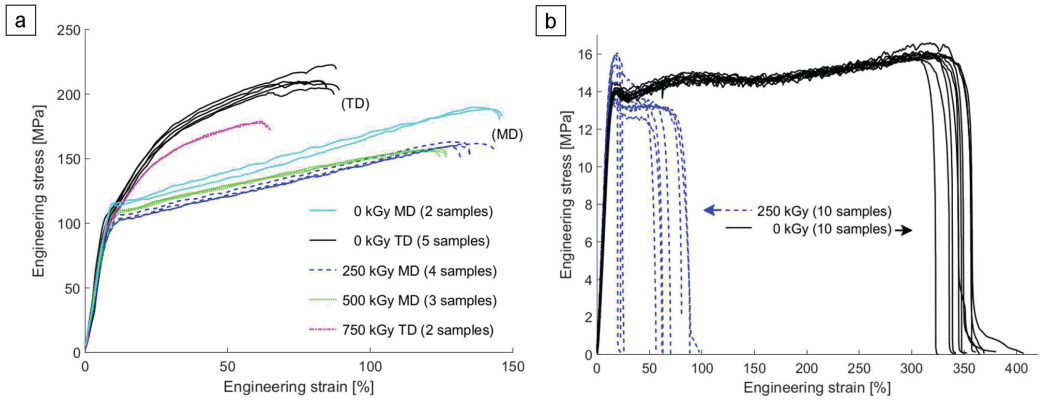

Figure 3.15 (a) Stress-strain curves of PET foils exposed to different electron irradiation doses. Different behaviour was found regarding the fabrication direction of the foil. The MD direction exhibited a reduction of the ultimate tensile strength, whereas for the TD direction both the ultimate tensile strain and the ultimate tensile strength yielded lower values for a irradiation dose of 750 kGy. (b) An electron irradiation of 250 kGy lead to a severe degradation of the FEP VDA samples. Figures are taken from the appended *publication B*.

For investigations on the degradation behaviour of materials not only a high lateral resolution is of interest. As irradiation may lead to a depth dependent alteration of material properties, mechanical tests using samples from different depths could deliver relevant informations to understand the evolution of the degradation process. Therefore, an evaluation of the possibility for a local thinning of the foil specimens using the fs-laser was conducted. For this the specimen needs to be positioned

according to the material's and the laser parameter dependent taper angle to achieve material removal parallel to the foil surfaces (as sketched in Fig. 3.16a). In Fig. 3.16b an example of a thinned section with a thickness of about 80 μm is shown. A tensile sample cut into this section is presented in Fig. 3.16c. This local thinning of foils or wedges and the subsequent fabrication of mechanical specimens has the potential to measure depth-resolved mechanical properties with a maximum resolution of about 20 μm.

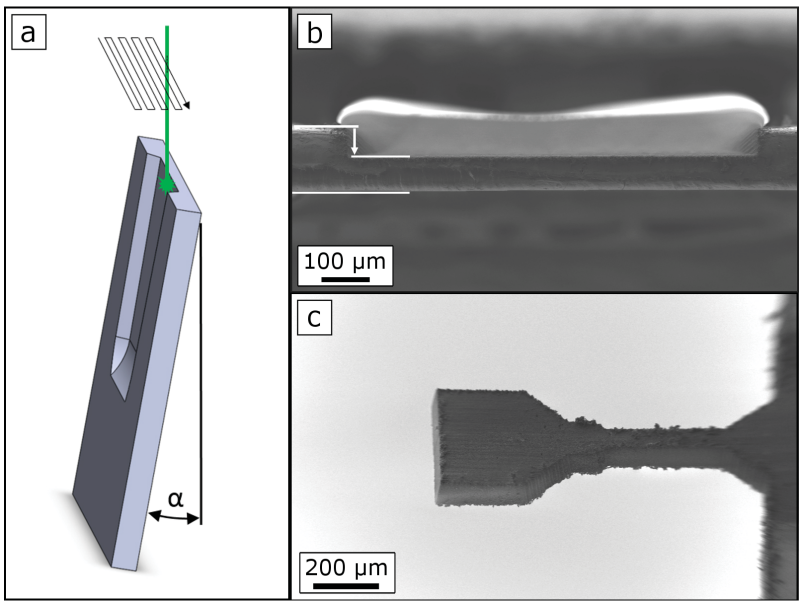

Figure 3.16 The fs-laser enables a local thinning of the foil samples. (a) Scanning route of the laser beam with the foil tilted to the expected taper angle α. (b) FEP VDA foil sample with a thickness reduced window of approximately 800 μm width. (c) Tensile sample with a thickness of about 80 μm. Figure is taken from the appended *publication B*.

Details on the study of electron irradiation effects on the tensile properties of polymer foils can be found in the appended *publication B*.

Wood

Investigations on the mechanical properties of wood are usually confined to macroscopically sized samples [91] or on the other end of the size scale to the testing of single fibres [92]. The size gap in between was not extensively studied so far. This is because the preparation of small samples to evaluate local mechanical properties of biological materials is difficult for established techniques. However, if one seeks to understand the interaction response of single fibres or any hierarchical effects a variation of the sample size is necessary. The typical cell size of spruce wood is

roughly $20 \times 20\,\mu$m, thus, if one aims to understand the mechanical behaviour of the interaction of multiple cells, the low material removal rate of the FIB does not allow to fabricate samples with proper dimensions in a reasonable time. Additionally, the FIB technique can lead to a significant amount of ion implantation [93] and requires high vacuum conditions for processing.

The method of micro electro discharge machining, which could cover a larger scale starting from feature sizes of few $100\,\mu$m, is only available for conductive materials. Pulsed laser processing, however, enables a precise and versatile tool for the fabrication of specimens in this size regime.

Still, using pulse durations above the ultrashort regime can result in carbonization of the material [94, 95]. On the contrary, the use of ultrashort pulsed lasers compared to short pulsed lasers leads to significantly less damage and no carbonization [96, 97]. Nevertheless, as discussed in Sec. 3.2.1 for materials with a low heat conductivity, like wood, the possible accumulation of heat with the successive deterioration of the material needs to be kept in mind.

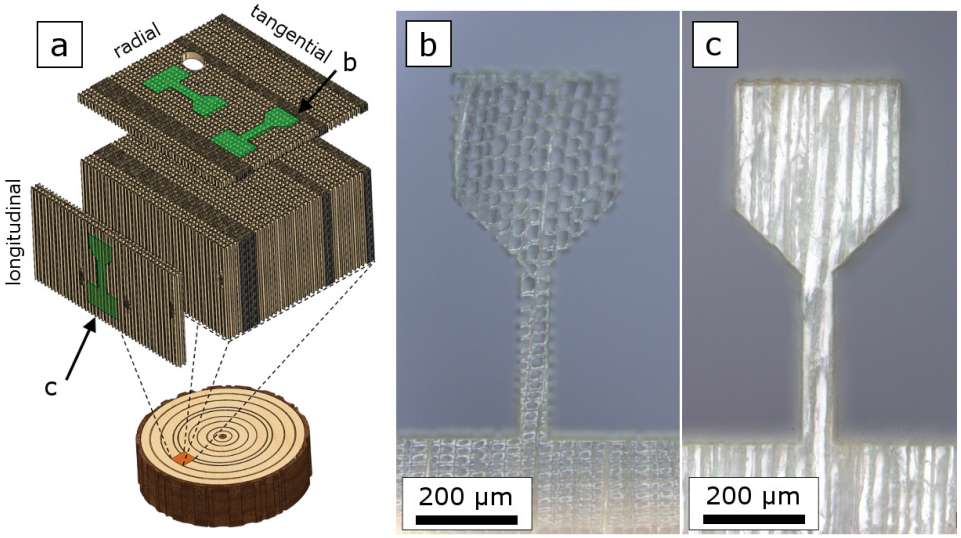

Figure 3.17 (a) A microtome was used to fabricate thin sections in longitudinal-tangential (lt) and radial-tangential (rt) orientation. Optical micro-graphs of tensile samples cut via a fs-laser into (b) a rt-section and (c) a lt-section, as indicated by the green specimen sketches in (a), clearly reveal the orientation of the cell structure and to not exhibit any observable damage due to the fs-laser processing. Figures were taken from *publication E* and were adapted.

By chosing the processing parameters carefully, the fs-laser provides access to mechanical properties of biological materials on the meso-scale size regime. This was demonstrated by cutting tensile and compression samples out of thin sections of

spruce wood. Two orientations of this thin sections were prepared using a microtome: radial-tangential (rt) and longitudinal-tangential (lt) (see Fig. 3.17a). Samples were successively cut into these thin sections in different orientations with the fs-laser. The laser parameters were: fluence of $0.65\,\mathrm{J/cm^2}$, pulse repetition rate of $1.25\,\mathrm{kHz}$ and a scan speed of $2\,\mathrm{mm/s}$. Fig. 3.17b shows a tensile sample in a rt-section and Fig. 3.17c a tensile sample in a lt-section.

In addition to that, an examination of the samples using an optical microscope and a SEM did not show any observable damage. Consequently, the influence of the fs-laser ablation is assumed to be negligible for properly chosen parameters. On the contrary, tensile samples fabricated from an alternative production route, using an ion slicer and a respective mask, yielded besides a non-defined structure a severe embrittlement of the material.

The mechanical testing of tensile and compression samples fabricated using the fs-laser exhibited results in good agreement with the respectively scaled values extracted from experiments on single wood fibres. An exemplary load displacement curve is displayed in Fig. 3.18a for a sample loaded in longitudinal direction and in Fig. 3.18b for a sample loaded in tangential direction. The orientations exhibit distinctively different failure mechanisms. Optical micrographs recorded during the loading, enabled to link features of the curves to certain deformation states of the specimen. In Fig. 3.18 micrographs of selected events are given. It was found that the longitudinal samples show primarily intra-wall fracture, whereas the tangential samples fail through cell wall rupture and fibre debonding.

Details on the characterization of local mechanical properties of spruce wood can be found in *publication E*.

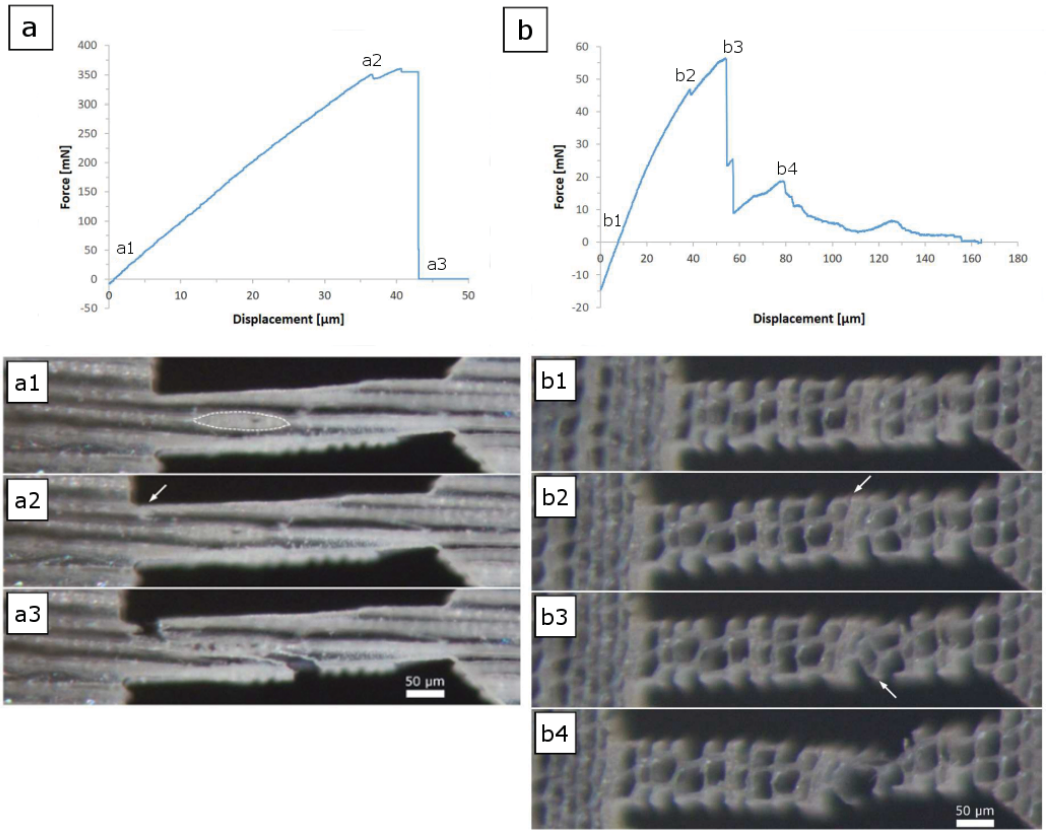

Figure 3.18 (a) Representative force displacement diagram of a longitudinal specimen. Three optical micrographs (a1-a3) were recorded at the loading states indicated in the diagram. (a1) The state prior to any loading with an intersecting wood ray being indicated by the white dashed line. (a2) The initiation point of a crack is indicated by a white arrow. (a3) Intrawall fracture leads to final failure at a force of about 350 mN. (b) Representative force displacement diagram of a tangential specimen. Four optical micrographs (b1-b4) were recorded at the loading states indicated in the diagram.(b1) displays the specimen prior to loading. The white arrow indicates the rupture of a cell wall in (b2) and fibre debonding in (b3). (b4) The remaining single cell wall gets pulled apart. Figures are taken from *publication E* and were adapted.

3.4.3 Single leg bending specimens

Structural applications are a severe challenge for tungsten materials due to their inherent brittleness at room temperature. Promising approaches, like laminated or fibre-reinforced tungsten composites were developed to overcome this low ductility [98]. The components of this composites are ultra fine grained (UFG) polycrystalline tungsten foils and wires, respectively. The fabrication routes of this UFG materials,

cold rolling and drawing, lead to the formation of a typically elongated microstructure, which exhibits a distinct anisotropy in mechanical properties. Perpendicular to the rolling (RD) and drawing (DD) direction a high fracture resistance was found [99, 100]. This high value is based on crack deflection and delamination toughening mechanisms as along the elongated microstructure pronounced delaminations were observed. This delaminations indicate a significantly lower fracture resistance for crack propagation along the RD and the DD compared to the perpendicular direction.

Fracture toughness evaluation for crack propagation in this "weak" direction using classical macro-scale fracture mechanics samples is not possible due to the limited dimensions of the initial material (i.e. thickness of 100 μm of the foils and a diameter of 150 μm of the wires). The other typical approach of processing FIB micro-fracture samples is not feasible in the present case due to: 1) the low material removal rate of a FIB especially for tungsten; 2) the observation of a possible R-curve (K versus Δa) behaviour, due to bridging effects, requires multiple grains along the crack propagation path. Hence, for the grain sizes of the investigated materials a sample size of at least few tens of micrometers is needed. Therefore, for the evaluation of the intergranular crack growth fracture resistance along the elongated microstructure an experimental method was developed based on macroscopic single leg bending (SLB) experiments. The specimens were fabricated using the fs-laser. The final notch was introduced using the FIB. The typical dimension of the specimens were: notch length $a \approx 500\,\mu$m, thickness $b \approx 45\,\mu$m, calmping length $c \approx 1200\,\mu$m, height of the legs $t_1, t_2 \approx 50\,\mu$m for the foil specimens and $t_1, t_2 \approx 75\,\mu$m for the wire specimens.

The experiments were performed in-situ in a SEM, to observe the crack propagation during loading. A micrograph of a loaded SLB specimen processed from a wire, recorded during such an in-situ experiment, is given in Fig. 3.19a. Fig. 3.19b shows a micrograph with a higher magnification, which allows to measure the crack length Δa. This information in combination with the recorded load displacement curves (see Fig. 3.19c) enables to obtain the R-curves for the fracture toughness depicted in Fig. 3.20.

The typical global K_I to K_{II} ratio of SLB specimens (considering equal leg heights and a crack to length ratio of 1/2) is about 0.87 [101]. For such a relatively high mode mixity an influence of the mode II component would be expected. However, fracture experiments on brittle materials with mixed mode loading showed a good agreement with the maximum tensile stress criterion [102, 103]. According to this criterion and a crack deflection angle of about 0° the dominating contribution for the fracture toughness is the K_I component. Therefore, in the following the discussion of the results is focused on K_I.

The initial fracture toughness values K_{Ii} are listed in Tab. 3.3. For each material 3 samples were tested. Significantly higher values of the initial fracture toughness values were found for the wires compared to the foils. This could mainly be explained

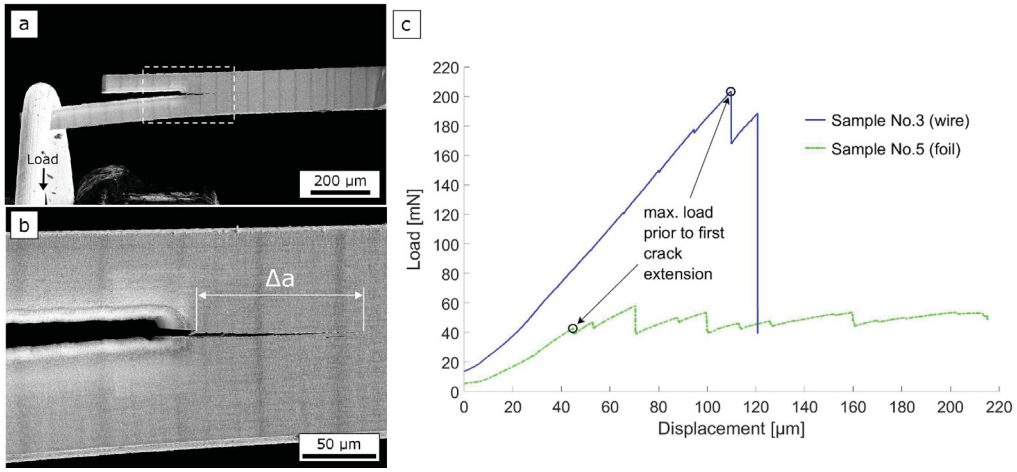

Figure 3.19 (a) Example of a loaded SLB sample with a propagated crack. (b) The detail indicated with the white, dashed rectangle in (a), displays the crack elongation Δa. (c) Load versus displacement curves exemplarily for one UFG tungsten wire and one UFG tungsten foil sample. The load values prior to the initial crack propagation are indicated. Figure is taken from the appended *publication C*.

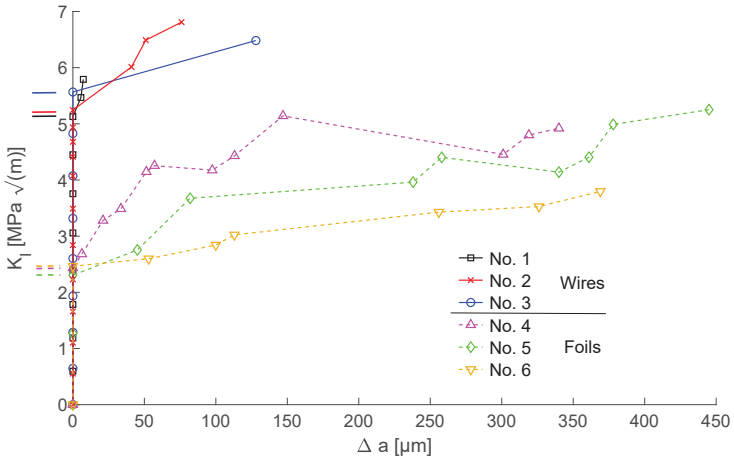

Figure 3.20 R-curves evaluated via the data from the in-situ SLB experiments. The wire specimens show a significantly higher stress intensity value for crack initiation K_{Ii}, compared to the foil specimens. The horizontal lines besides the ordinate indicate the K_{Ii} values. Figure is taken from the appended *publication C*.

by the different morphology of the fracture surfaces. The wire samples exhibited a rough "zig-zag-like" surface, whereas the fracture surfaces of the foils were very flat.

Furthermore, a difference in the R-curve behaviour was observed (see Fig. 3.20).

	Wire		Foil
No.	K_{Ii} [MPa$\sqrt{m}$]	No.	K_{Ii} [MPa$\sqrt{m}$]
1	5.13	4	2.43
2	5.24	5	2.30
3	5.57	6	2.46

Table 3.3 Experimental fracture initiation toughness values for a crack propagation along the elongated microstructure of UFG tungsten wires and foils evaluated via SLB experiments.

The wire samples show a short increase of the K_I value with a maxiumum crack elongation Δa of about 130 μm before final failure occurs, where the crack propagates to the end of the thinned section of the sample. On the contrary, the foil specimens exhibit a slower crack propagation with relatively constant distances between each crack arrest. These samples yield a maximum crack elongation Δa of about 450 μm.

The R-curve behaviour in these experiments was found to be dominated by bridging. Both materials show a distinctively different structure of bridges, which can be linked to their different microstructure. The flat pancake-like microstucture of the foils lead to large, thin bridges, which exhibit small resistance against bending. Additionally, as the initial FIB notch is better aligned with the flat microstructure, compared to the case of the wires, few bridges are formed initially. On the contrary, the fibrous microstructure of the wires yields a higher interconnection between each grain, hence, bridge formation is impeded. Furthermore, due to their cigar-like shape the grains have a higher stiffness compared to the flat grains of the foils. Therefore, for the wire material the development of only small, stiff bridges was observed, resulting in a steeper R-curve.

Details on the evaluation of the intergranular crack growth resistance of UFG tungsten wires and foils can be found in the appended *publication C*.

4
Conclusions and outlook

In this thesis a novel system combining a femtosecond laser with a scanning electron and a focused ion beam column was developed. This unique system allows an accurate positioning and high resolution imaging by means of the scanning electron microscope, a fast processing with the femtosecond laser and optionally a refinement of the processed surfaces and structures via the FIB. For all kinds of materials the femtosecond laser enables a precise, contactless micro-fabrication with minimal material influence due to non-thermal ablation.

For ideal results in processing quality it was shown that the laser parameters need to be thoroughly chosen. Primarily, the fluence needs to be in or near the low fluence regime for the processed material. Further, the resulting sample quality can be deteriorated by: (i) heat accumulation, (ii) re-deposition of ablated material, (iii) laser induced periodic surface structures and cone structures and (iv) formation of a taper. The main strategies identified to reduce these artefacts are respectively: (i) reduction of the pulse repetition rate, (ii) adaption of the laser beam scanning route, (iii) reduction of the cumulative pulses per spot and (iv) tilt of the sample during processing. The optimal parameter combination is, however, always a trade-off between many requirements and needs to be evaluated separately for each case.

Mechanical samples on the meso-scale ($\approx$100-1000 μm) were fabricated using the femtosecond laser without any need for post-processing, hence, being an unrivalled method in this size regime regarding the high processing speed and the low influence on the material. Successful applications of this method for specimen preparation were showcased for different material classes and sample geometries.

The preparation of bending cantilevers in thin tungsten foils displayed the superiority of the femtosecond laser compared to the focused ion beam regarding the processing speed. Furthermore, an analysis of the effect of the femtosecond laser processing on the material was performed and compared to the processing using a nanosecond laser. The results exhibited no influence of the femtosecond laser on the micro-structure as well as a higher surface quality, in comparison with the nanosecond laser.

In a further study the intergranular crack growth resistance along the elongated micro-structure of ultrafine grained tungsten foils and wires was determined, using laser fabricated single leg bending specimens. The foils yielded a fracture initiation

toughness of 2.4 MPa$\sqrt{m}$ and the wires 5.3 MPa$\sqrt{m}$, respectively.

An additional work was conducted on the preparation and testing of femtosecond laser processed tensile specimens on different polymer foils. The results showed a negligible influence of the laser processing and enabled to investigate the effect of electron irradiation on the local tensile properties of polymer foils used in spacecraft engineering.

For micro-mechanical experiments on biological materials it was found for spruce wood that the use of the femtosecond laser technology allows an efficient fabrication of pristine specimens. This offers interesting opportunities, for example, to investigate mechanical properties of bone tissue or enamel and dentine components of teeth on the small scale. Especially for the hierarchical structure of many biological materials the possibility to cover a large size range with mechanical experiments can help to investigate their length-scale dependent mechanical properties. Furthermore, the system enables a fabrication under atmospheric conditions. This is of interest for the preservation of biological tissues, which are hydrated in-vivo (e.g. bones) and therefore may exhibit alteration in their mechanical properties when exposed to vacuum conditions.

A further field of application is the preparation of thin slices of brittle materials or brittle thin films on a substrate, which is a demanding and time consuming task for common metallographic methods. The femtosecond laser enables a fast and reliable method to prepare wedges with a thickness of tens to hundreds of micrometer, independent of the material's brittleness. These wedges can for example be used for investigations like nano X-ray diffraction or they are utilized as precursor for further focused ion beam cutting, hence, reducing the processing time significantly as the volume of material, which needs to be removed, can be cut down distinctively.

A type of specimens, which has been processed by femtosecond laser but has not yet been properly evaluated by mechanical experiments, are (circular) compression pillars. Their fabrication is still a challenging task due to the large taper and the difficulty of achieving a determined cutting depth. However, if these difficulties can be overcome, it could open up a way of a rapid fabrication of a large amount of samples directly from the bulk, having the potential of laterally mapping mechanical properties of various materials.

Depending on future applications of the developed system, certain improvements and adaptions can be made. The Gaussian pulse shape could be changed to a rectangular tophat shape using a beam shaper. This enables the reduction of residual heat introduced by each single pulse and allows higher precision and pulse repetition rates without damaging the material. Further, instead of the f-θ lens a telecentric scanning lens could be installed. It enables a normal incidence on the horizontal sample plane across the whole scan area and provides continuous conditions regarding the formation of a taper. The taper issue could also be tackled efficiently by installing a precisely tilt-able sample holder, which can be controlled remotely. Such

a solution would be advantageous especially for complex sample geometries, such as the presented single leg bending specimens. Moreover, as the focal spot size determines the minimum processable structures, a further reduction of its diameter is of interest. This could be achieved by placing an additional collecting lens in the beam path right above the sample surface. However, this approach will amplify existing optical aberrations.

Ultimately, the promising results of the present thesis show that, especially in the field of micro-mechanical testing, an increase in the usage of femtosecond lasers can be anticipated. The author expects, that due to the increasing availability of fs-laser systems, the development of plug-and-play devices and because of the decreasing costs of such units with onward technological improvements, more applications for these *"tools made of light"* [5] will emerge in future in the field of materials testing and research.

5
Bibliography

Bibliography

[1] A. L. Schawlow and C. H. Townes, "Infrared and Optical Masers," *Phys. Rev.*, vol. 112, pp. 1940–1949, Dec. 1958.

[2] M. Bertolotti, *The History of the Laser*. CRC Press, Oct. 2004.

[3] T. H. Maiman, "Stimulated Optical Radiation in Ruby," *Nature*, vol. 187, p. 493, Aug. 1960.

[4] "Developer of the Laser Calls It A Solution Seeking a Problem," *The New York Times*, p. 69, May 1964.

[5] NobelPrize.org, *The Nobel Prize in Physics 2018*. Nobel Media AB, 2019.

[6] D. Strickland and G. Mourou, "Compression of amplified chirped optical pulses," *Optics Communications*, vol. 55, pp. 447–449, Oct. 1985.

[7] B. N. Chichkov, C. Momma, S. Nolte, F. von Alvensleben, and A. Tünnermann, "Femtosecond, picosecond and nanosecond laser ablation of solids," *Appl. Phys. A*, vol. 63, pp. 109–115, Aug. 1996.

[8] K. Sugioka and Y. Cheng, "Ultrafast lasers reliable tools for advanced materials processing," *Light: Science & Applications*, vol. 3, p. e149, Apr. 2014.

[9] S. Weiler, "Ultrafast lasers: high-power pico- and femtosecond lasers enable new applications," *Laser Focus World*, vol. 47, pp. 955–992, Oct. 2011.

[10] M. D. Uchic, D. M. Dimiduk, J. N. Florando, and W. D. Nix, "Sample Dimensions Influence Strength and Crystal Plasticity," *Science*, vol. 305, pp. 986–989, Aug. 2004.

[11] M. W. Phaneuf, "Applications of focused ion beam microscopy to materials science specimens," *Micron*, vol. 30, pp. 277–288, June 1999.

[12] K. Sugioka, M. Meunier, and A. Piqu, eds., *Laser Precision Microfabrication*. Springer Series in Materials Science, Berlin Heidelberg: Springer-Verlag, 2010.

[13] M. D. Shirk and P. A. Molian, "A review of ultrashort pulsed laser ablation of materials," *Journal of Laser Applications*, vol. 10, pp. 18–28, Feb. 1998.

[14] T. Gaumnitz, A. Jain, Y. Pertot, M. Huppert, I. Jordan, F. Ardana-Lamas, and H. J. Wörner, "Streaking of 43-attosecond soft-X-ray pulses generated by a passively CEP-stable mid-infrared driver," *Opt. Express*, vol. 25, pp. 27506–27518, Oct. 2017.

[15] J. Meijer, K. Du, A. Gillner, D. Hoffmann, V. S. Kovalenko, T. Masuzawa, A. Ostendorf, R. Poprawe, and W. Schulz, "Laser Machining by short and ultrashort pulses, state of the art and new opportunities in the age of the photons," *CIRP Annals*, vol. 51, pp. 531–550, Jan. 2002.

[16] K. Sugioka and Y. Cheng, *Ultrafast Laser Processing: From Micro-to Nanoscale*. Singapore: Pan Stanford Publishing Pte Ltd, June 2013.

[17] M. Castillejo, P. M. Ossi, and L. Zhigilei, eds., *Lasers in Materials Science*. Springer Series in Materials Science, Springer International Publishing, 2014.

[18] M. V. Shugaev, C. Wu, O. Armbruster, A. Naghilou, N. Brouwer, D. S. Ivanov, T. J.-Y. Derrien, N. M. Bulgakova, W. Kautek, B. Rethfeld, and L. V. Zhigilei, "Fundamentals of ultrafast lasermaterial interaction," *MRS Bulletin*, vol. 41, pp. 960–968, Dec. 2016.

[19] S. Ansimov, B. Kapeliovich, and T. Perel'man, "Electron-emission from surface of metals induced by ultrashort laser pulses," *Sov. Phys. JETP*, vol. 39, pp. 375–377, August 1974.

[20] Y. L. Yao, H. Chen, and W. Zhang, "Time scale effects in laser material removal: a review," *Int. J. Adv. Manuf. Technol.*, vol. 26, pp. 598–608, Sept. 2005.

[21] J. Krüger and W. Kautek, "Ultrashort Pulse Laser Interaction with Dielectrics and Polymers," in *Polymers and Light* (T. K. Lippert, ed.), Advances in Polymer Science, pp. 247–290, Berlin, Heidelberg: Springer Berlin Heidelberg, 2004.

[22] H. Schwoerer, "Generation of X-Rays by Intense Femtosecond Lasers," in *Femtosecond Technology for Technical and Medical Applications* (F. Dausinger, H. Lubatschowski, and F. Lichtner, eds.), Topics in Applied Physics, pp. 235–254, Berlin, Heidelberg: Springer Berlin Heidelberg, 2004.

[23] A. Y. Vorobyev and C. Guo, "Colorizing metals with femtosecond laser pulses," *Appl. Phys. Lett.*, vol. 92, p. 041914, Jan. 2008.

[24] A. Vorobyev and C. Guo, "Direct femtosecond laser surface nano/microstructuring and its applications," *Laser & Photonics Reviews*, vol. 7, pp. 385–407, May 2013.

[25] K. Sugioka and Y. Cheng, *Femtosecond Laser 3D Micromachining for Microfluidic and Optofluidic Applications*. SpringerBriefs in Applied Sciences and Technology, London: Springer-Verlag, 2014.

[26] X. Liu, D. Du, and G. Mourou, "Laser ablation and micromachining with ultrashort laser pulses," *IEEE Journal of Quantum Electronics*, vol. 33, pp. 1706–1716, Oct. 1997.

[27] W. Kautek and J. Krueger, "Femtosecond pulse laser ablation of metallic, semiconducting, ceramic, and biological materials," in *Laser Materials Processing: Industrial and Microelectronics Applications*, vol. 2207, pp. 600–611, International Society for Optics and Photonics, Sept. 1994.

[28] E. G. Gamaly, *Femtosecond Laser-Matter Interaction: Theory, Experiments and Applications*. Singapore: Pan Stanford Publishing Pte Ltd, 1 ed., Oct. 2011.

[29] K. Furusawa, K. Takahashi, H. Kumagai, K. Midorikawa, and M. Obara, "Ablation characteristics of Au, Ag, and Cu metals using a femtosecond Ti:sapphire laser," *Appl. Phys. A*, vol. 69, pp. S359–S366, Dec. 1999.

[30] M. E. Shaheen, J. E. Gagnon, and B. J. Fryer, "Femtosecond laser ablation behavior of gold, crystalline silicon, and fused silica: a comparative study," *Laser Phys.*, vol. 24, p. 106102, Aug. 2014.

[31] S. Nolte, C. Momma, H. Jacobs, A. Tünnermann, B. N. Chichkov, B. Wellegehausen, and H. Welling, "Ablation of metals by ultrashort laser pulses," *J. Opt. Soc. Am. B.*, vol. 14, pp. 2716–2722, Oct. 1997.

[32] T. Matsumura, A. Kazama, and T. Yagi, "Generation of debris in the femtosecond laser machining of a silicon substrate," *Appl. Phys. A*, vol. 81, pp. 1393–1398, Nov. 2005.

[33] N. G. Semaltianos, W. Perrie, V. Vishnyakov, R. Murray, C. J. Williams, S. P. Edwardson, G. Dearden, P. French, M. Sharp, S. Logothetidis, and K. G. Watkins, "Nanoparticle formation by the debris produced by femtosecond laser ablation of silicon in ambient air," *Materials Letters*, vol. 62, pp. 2165–2170, May 2008.

[34] M. P. Echlin, M. S. Titus, M. Straw, P. Gumbsch, and T. M. Pollock, "Materials response to glancing incidence femtosecond laser ablation," *Acta Materialia*, vol. 124, pp. 37–46, Feb. 2017.

[35] M. P. Echlin, A. Mottura, C. J. Torbet, and T. M. Pollock, "A new TriBeam system for three-dimensional multimodal materials analysis," *Review of Scientific Instruments*, vol. 83, p. 023701, Feb. 2012.

[36] J. Krüger, M. Lenzner, S. Martin, M. Lenner, C. Spielmann, A. Fiedler, and W. Kautek, "Single- and multi-pulse femtosecond laser ablation of optical filter materials," *Applied Surface Science*, vol. 208, pp. 233–237, Mar. 2003.

[37] A. Rosenfeld, M. Lorenz, R. Stoian, and D. Ashkenasi, "Ultrashort-laser-pulse damage threshold of transparent materials and the role of incubation," *Appl. Phys. A*, vol. 69, pp. S373–S376, Dec. 1999.

[38] J. Byskov-Nielsen, J.-M. Savolainen, M. S. Christensen, and P. Balling, "Ultrashort pulse laser ablation of metals: threshold fluence, incubation coefficient and ablation rates," *Appl. Phys. A*, vol. 101, pp. 97–101, Oct. 2010.

[39] L. G. DeShazer, B. E. Newnam, and K. M. Leung, "Role of coating defects in laserinduced damage to dielectric thin films," *Appl. Phys. Lett.*, vol. 23, pp. 607–609, Dec. 1973.

[40] O. Armbruster, A. Naghilou, M. Kitzler, and W. Kautek, "Spot size and pulse number dependence of femtosecond laser ablation thresholds of silicon and stainless steel," *Applied Surface Science*, vol. 396, pp. 1736–1740, Feb. 2017.

[41] A. Ancona, F. Röser, K. Rademaker, J. Limpert, S. Nolte, and A. Tünnermann, "High speed laser drilling of metals using a high repetition rate, high average power ultrafast fiber CPA system," *Opt. Express*, vol. 16, pp. 8958–8968, June 2008.

[42] J. König, S. Nolte, and A. Tünnermann, "Plasma evolution during metal ablation with ultrashort laser pulses," *Opt. Express*, vol. 13, pp. 10597–10607, Dec. 2005.

[43] S. Nolte, F. Schrempel, and F. Dausinger, eds., *Ultrashort Pulse Laser Technology: Laser Sources and Applications*. Springer Series in Optical Sciences, Springer International Publishing, 2016.

[44] A. Vorobyev, V. Kuzmichev, N. Kokody, P. Kohns, J. Dai, and C. Guo, "Residual thermal effects in Al following single ns- and fs-laser pulse ablation," *Appl. Phys. A*, vol. 82, pp. 357–362, Feb. 2006.

[45] H. M. van Driel, J. E. Sipe, and J. F. Young, "Laser-Induced Periodic Surface Structure on Solids: A Universal Phenomenon," *Phys. Rev. Lett.*, vol. 49, pp. 1955–1958, Dec. 1982.

[46] X. Yu, D. Qi, H. Wang, Y. Zhang, L. Wang, Z. Zhang, S. Dai, X. Shen, P. Zhang, and Y. Xu, "In situ and ex-situ physical scenario of the femtosecond laser-induced periodic surface structures," *Opt. Express*, vol. 27, pp. 10087–10097, Apr. 2019.

[47] M. Birnbaum, "Semiconductor Surface Damage Produced by Ruby Lasers," *Journal of Applied Physics*, vol. 36, pp. 3688–3689, Nov. 1965.

[48] M. J. Abere, M. Zhong, J. Krüger, and J. Bonse, "Ultrafast laser-induced morphological transformations," *MRS Bulletin*, vol. 41, pp. 969–974, Dec. 2016.

[49] J. Bonse, S. Höhm, S. V. Kirner, A. Rosenfeld, and J. Krüger, "Laser-Induced Periodic Surface Structures A Scientific Evergreen," *IEEE Journal of Selected Topics in Quantum Electronics*, vol. 23, May 2017.

[50] J. Long, P. Fan, M. Zhong, H. Zhang, Y. Xie, and C. Lin, "Superhydrophobic and colorful copper surfaces fabricated by picosecond laser induced periodic nanostructures," *Applied Surface Science*, vol. 311, pp. 461–467, Aug. 2014.

[51] D. S. Milovanovi, B. Gakovi, C. Radu, M. Zamfirescu, B. Radak, S. Petrovi, Z. R. Miladinovi, and I. N. Mihailescu, "Femtosecond laser surface patterning of steel and titanium alloy," *Phys. Scr.*, vol. 2014, p. 014017, Sep. 2014.

[52] J. J. Nivas, F. Gesuele, E. Allahyari, S. L. Oscurato, R. Fittipaldi, A. Vecchione, R. Bruzzese, and S. Amoruso, "Effects of ambient air pressure on surface structures produced by ultrashort laser pulse irradiation," *Opt. Lett., OL*, vol. 42, pp. 2710–2713, July 2017.

[53] A. Ancona, S. Döring, C. Jauregui, F. Röser, J. Limpert, S. Nolte, and A. Tünnermann, "Femtosecond and picosecond laser drilling of metals at high repetition rates and average powers," *Opt. Lett., OL*, vol. 34, pp. 3304–3306, Nov. 2009.

[54] Q. Wang, A. Chen, S. Li, H. Qi, Y. Qi, Z. Hu, and M. Jin, "Influence of ambient pressure on the ablation hole in femtosecond laser drilling Cu," *Appl. Opt.*, vol. 54, pp. 8235–8240, Sept. 2015.

[55] G. Yang, Q. Lin, Y. Ding, D. Tian, and Y. Duan, "Laser Induced Breakdown Spectroscopy Based on Single Beam Splitting and Geometric Configuration for Effective Signal Enhancement," *Scientific Reports*, vol. 5, p. 7625, Jan. 2015.

[56] Y. Miyasaka, M. Hashida, T. Nishii, S. Inoue, and S. Sakabe, "Derivation of effective penetration depth of femtosecond laser pulses in metal from ablation rate dependence on laser fluence, incidence angle, and polarization," *Appl. Phys. Lett.*, vol. 106, p. 013101, Jan. 2015.

[57] C. A. Zuhlke, T. P. Anderson, and D. R. Alexander, "Formation of multiscale surface structures on nickel via above surface growth and below surface growth mechanisms using femtosecond laser pulses," *Opt. Express*, vol. 21, pp. 8460–8473, Apr. 2013.

[58] E. J. Y. Ling, J. Sad, N. Brodusch, R. Gauvin, P. Servio, and A.-M. Kietzig, "Investigating and understanding the effects of multiple femtosecond laser scans on the surface topography of stainless steel 304 and titanium," *Applied Surface Science*, vol. 353, pp. 512–521, Oct. 2015.

[59] B. Pecholt, M. Vendan, Y. Dong, and P. Molian, "Ultrafast laser micromachining of 3c-SiC thin films for MEMS device fabrication," *Int. J. Adv. Manuf. Technol.*, vol. 39, pp. 239–250, Oct. 2008.

[60] A. Shyam, Y. N. Picard, J. W. Jones, J. E. Allison, and S. M. Yalisove, "Small fatigue crack propagation from micronotches in the cast aluminum alloy W319," *Scripta Materialia*, vol. 50, pp. 1109–1114, Apr. 2004.

[61] Y. Motoyashiki, A. Brückner-Foit, L. Englert, L. Haag, M. Wollenhaupt, and T. Baumert, "Use of Femtosecond Laser Technique for Studying Physically Small Cracks," *Int. J. Fract.*, vol. 139, pp. 561–568, June 2006.

[62] W. Zhao, P. Rao, and Z. Ling, "A new method for the preparation of ultra-sharp V-notches to measure fracture toughness in ceramics," *Journal of the European Ceramic Society*, vol. 34, pp. 4059–4062, Dec. 2014.

[63] T. Palacios and J. Y. Pastor, "Influence of the notch root radius on the fracture toughness of brittle metals: Nanostructure tungsten alloy, a case study," *International Journal of Refractory Metals and Hard Materials*, vol. 52, pp. 44–49, Sept. 2015.

[64] W. Zhao, J. P. Cui, and P. G. Rao, "Effect of thermal stress induced by femtosecond laser on fracture toughness of fine-grained alumina," *J. Aust. Ceram. Soc.*, vol. 55, pp. 575–578, June 2019.

[65] Y. C. Lim, K. Altman, D. F. Farson, and K. Flores, "Micropillar fabrication on bovine cortical bone by direct-write femtosecond laser ablation," *JBO*, vol. 14, p. 064021, Nov. 2009.

[66] C. Park and D. F. Farson, "Precise machining of disk shapes from thick metal substrates by femtosecond laser ablation," *Int. J. Adv. Manuf. Technol.*, vol. 83, pp. 2049–2056, Apr. 2016.

[67] J. G. Gigax, H. Vo, Q. McCulloch, M. Chancey, Y. Wang, S. A. Maloy, N. Li, and P. Hosemann, "Micropillar compression response of femtosecond laser-cut single crystal Cu and proton irradiated Cu," *Scripta Materialia*, vol. 170, pp. 145–149, Sept. 2019.

[68] S. K. Slaughter, J. P. Ligda, T. Sano, and B. E. Schuster, "High Throughput Femtosecond-Laser Machining of Micro-Tension Specimens," in *TMS 2015 144th Annual Meeting & Exhibition*, pp. 471–478, Springer, Cham, 2015.

[69] D. W. Eastman, Z. Alam, G. Weber, P. A. Shade, M. D. Uchic, W. C. Lenthe, T. M. Pollock, and K. J. Hemker, "Benchmarking Crystal Plasticity Models with Microtensile Evaluation and 3d Characterization of Ren 88DT," in *Superalloys 2016*, pp. 811–820, John Wiley & Sons, Ltd, Oct. 2016.

[70] D. J. Magagnosc, J. P. Ligda, T. Sano, and B. E. Schuster, "Femtosecond Laser Machining of Micro-tensile Specimens for High Throughput Mechanical Testing," in *Micro and Nanomechanics, Volume 5*, Conference Proceedings of the Society for Experimental Mechanics Series, pp. 7–9, Springer, Cham, 2018.

[71] C. A. Volkert and A. M. Minor, "Focused Ion Beam Microscopy and Micromachining," *MRS Bulletin*, vol. 32, pp. 389–399, May 2007.

[72] M. D. Uchic, P. A. Shade, and D. M. Dimiduk, "Plasticity of Micrometer-Scale Single Crystals in Compression," *Annual Review of Materials Research*, vol. 39, no. 1, pp. 361–386, 2009.

[73] J. R. Greer and J. T. M. De Hosson, "Plasticity in small-sized metallic systems: Intrinsic versus extrinsic size effect," *Progress in Materials Science*, vol. 56, pp. 654–724, Aug. 2011.

[74] D. Kiener, C. Motz, G. Dehm, and R. Pippan, "Overview on established and novel FIB based miniaturized mechanical testing using in-situ SEM," *IJMR*, vol. 100, pp. 1074–1087, Aug. 2009.

[75] L. Kwakman, G. Franz, M. M. V. Taklo, A. Klumpp, and P. Ramm, "Characterization and Failure Analysis of 3d Integrated Systems using a novel plasma FIB system," *AIP Conference Proceedings*, vol. 1395, pp. 269–273, Nov. 2011.

[76] L. Kwakman, M. Straw, G. Coustillier, M. Sentis, J. Beyersdorfer, J. Schischka, F. Naumann, and F. Altmann, "Sample preparation strategies for fast and effective failure analysis of 3d devices," in *ISTFA 2013: Proceedings from the 39th International Symposium for Testing and Failure Analysis*, pp. 17–26, ASM International, 2013.

[77] M. P. Echlin, N. S. Husseini, J. A. Nees, and T. M. Pollock, "A New Femtosecond Laser-Based Tomography Technique for Multiphase Materials," *Advanced Materials*, vol. 23, no. 20, pp. 2339–2342, 2011.

[78] J. Bailey, T. Heenan, D. Finegan, X. Lu, S. Daemi, F. Iacoviello, N. Backeberg, O. Taiwo, D. Brett, A. Atkinson, and P. Shearing, "Laser-preparation of geometrically optimised samples for X-ray nano-CT," *Journal of Microscopy*, vol. 267, pp. 384–396, Sept. 2017.

[79] T. Voisin, M. D. Grapes, Y. Zhang, N. Lorenzo, J. Ligda, B. Schuster, and T. P. Weihs, "TEM sample preparation by femtosecond laser machining and ion milling for high-rate TEM straining experiments," *Ultramicroscopy*, vol. 175, pp. 1–8, Apr. 2017.

[80] S. Lavenstein, B. Crawford, G.-D. Sim, P. A. Shade, C. Woodward, and J. A. El-Awady, "High frequency in situ fatigue response of Ni-base superalloy Ren-N5 microcrystals," *Acta Materialia*, vol. 144, pp. 154–163, Feb. 2018.

[81] S. Rubanov and P. R. Munroe, "FIB-induced damage in silicon," *Journal of Microscopy*, vol. 214, no. 3, pp. 213–221, 2004.

[82] D. Kiener, C. Motz, M. Rester, M. Jenko, and G. Dehm, "FIB damage of Cu and possible consequences for miniaturized mechanical tests," *Materials Science and Engineering: A*, vol. 459, pp. 262–272, June 2007.

[83] Y. Xiao, J. Wehrs, H. Ma, T. Al-Samman, S. Korte-Kerzel, M. Göken, J. Michler, R. Spolenak, and J. M. Wheeler, "Investigation of the deformation behavior of aluminum micropillars produced by focused ion beam machining using Ga and Xe ions," *Scripta Materialia*, vol. 127, pp. 191–194, Jan. 2017.

[84] I. Utke, S. Moshkalev, and P. Russell, *Nanofabrication Using Focused Ion and Electron Beams: Principles and Applications*. Oxford; New York: Oxford University Press, Dec. 2011.

[85] A. Jelinek, "Surface quality analysis of femto-second laser processed trenches," *Bachelor Thesis, University of Leoben*, 2018.

[86] J. Keckes, M. Bartosik, R. Daniel, C. Mitterer, G. Maier, W. Ecker, J. Vila-Comamala, C. David, S. Schoeder, and M. Burghammer, "X-ray nanodiffraction reveals strain and microstructure evolution in nanocrystalline thin films," *Scripta Materialia*, vol. 67, pp. 748–751, Nov. 2012.

[87] J. Ast, M. Göken, and K. Durst, "Size-dependent fracture toughness of tungsten," *Acta Materialia*, vol. 138, pp. 198–211, Oct. 2017.

[88] C. W. Cheng, "Ablation of copper by a scanning Gaussian beam of a femtosecond laser pulse," *Int. J. Adv. Manuf. Technol.*, vol. 92, pp. 151–156, Sept. 2017.

[89] K. Matoy, H. Schönherr, T. Detzel, T. Schöberl, R. Pippan, C. Motz, and G. Dehm, "A comparative micro-cantilever study of the mechanical behavior of silicon based passivation films," *Thin Solid Films*, vol. 518, pp. 247–256, Nov. 2009.

[90] K. K. de Groh, B. A. Banks, S. K. R. Miller, and J. A. Dever, "Chapter 28 - Degradation of Spacecraft Materials," in *Handbook of Environmental Degradation of Materials (Third Edition)* (M. Kutz, ed.), pp. 601–645, William Andrew Publishing, Jan. 2018.

[91] L. P. Fut, "Qualitative und quantitative Ermittlung der Mikrozugeigenschaften von Holz," *Holz als Roh-und Werkstoff*, vol. 27, pp. 192–201, May 1969.

[92] I. Burgert, J. Keckes, K. Frühmann, P. Fratzl, and S. E. Tschegg, "A Comparison of Two Techniques for Wood Fibre Isolation - Evaluation by Tensile Tests on Single Fibres with Different Microfibril Angle," *Plant Biology*, vol. 4, no. 1, pp. 9–12, 2002.

[93] S. Orso, "Structural and mechanical investigations of biological materials using a Focussed Ion Beam microscope," *Dissertation Universität Stuttgart*, 2005.

[94] Y. Wang, K. Ando, and N. Hattori, "Changes in the anatomy of surface and liquid uptake of wood after laser incising," *Wood Sci. Technol.*, vol. 47, pp. 447–455, May 2013.

[95] S. Fukuta, M. Nomura, T. Ikeda, M. Yoshizawa, M. Yamasaki, and Y. Sasaki, "UV laser machining of wood," *Eur. J. Wood Prod.*, vol. 74, pp. 261–267, Mar. 2016.

[96] E. Baubeau, R. L. Harzic, C. Jonin, E. Audouard, S. Mottin, M. Courbon, and P. Laporte, "Micromachining with high-repetition-rate femtosecond laser sources," in *First International Symposium on Laser Precision Microfabrication*, vol. 4088, pp. 48–50, International Society for Optics and Photonics, Nov. 2000.

[97] N. Naderi, S. Legacey, and S. L. Chin, "Preliminary investigations of ultrafast intense laser wood processing.," *Forest products journal*, June 1999.

[98] C. Ren, Z. Fang, M. Koopman, B. Butler, J. Paramore, and S. Middlemas, "Methods for improving ductility of tungsten - a review," *International Journal of Refractory Metals and Hard Materials*, vol. 75, pp. 170 – 183, Sept. 2018.

[99] V. Nikolić, J. Riesch, M. J. Pfeifenberger, and R. Pippan, "The effect of heat treatments on pure and potassium doped drawn tungsten wires: Part II Fracture properties," *Materials Science and Engineering: A*, vol. 737, pp. 434–447, Nov. 2018.

[100] V. Nikolić, S. Wurster, D. Firneis, and R. Pippan, "Fracture toughness evaluation of UFG tungsten foil," *International Journal of Refractory Metals and Hard Materials*, vol. 76, pp. 214–225, Nov. 2018.

[101] F. J. P. Chaves, L. F. M. d. da Silva, M. F. S. F. de Moura, D. A. Dillard, and V. H. C. Esteves, "Fracture Mechanics Tests in Adhesively Bonded Joints: A Literature Review," *The Journal of Adhesion*, vol. 90, pp. 955–992, Nov. 2014.

[102] F. Erdogan and G. C. Sih, "On the Crack Extension in Plates Under Plane Loading and Transverse Shear," *J. Basic Eng*, vol. 85, pp. 519–525, Dec. 1963.

[103] T. M. Maccagno and J. F. Knott, "The low temperature brittle fracture behaviour of steel in mixed modes I and II," *Engineering Fracture Mechanics*, vol. 38, pp. 111–128, Jan. 1991.

6
List of publications

Appended main-author publications

Publication A
M. J. Pfeifenberger, M. Mangang, S. Wurster, J. Reiser, A. Hohenwarter, Wilhelm Pfleging, Daniel Kiener, Reinhard Pippan
The use of femtosecond laser ablation as novel tool for rapid micro-mechanical sample preparation
Materials and Design, Vol. 121 (2017) 109-118

Publication B
M. J. Pfeifenberger, G. Milassin, A. Hohenwarter, B. Putz, C. O. A. Semprimoschnig, R. Pippan
Electron irradiation effects on strength and ductility of polymer foils studied by femtosecond laser processed micro-tensile specimens
Materials, Vol. 12, Issue 9 (2019) 1468

Publication C
M. J. Pfeifenberger, V. Nikolić, S. Žák, A. Hohenwarter, R. Pippan
Evaluation of the intergranular crack growth resistance of ultrafine grained tungsten materials
Acta Materialia, Vol. 176 (2019) 330-340

Co-author publications

Publication D
A. Kleinbichler, M. J. Pfeifenberger, J. Zechner, N. R. Moody, D. F. Bahr, M. J. Cordill
New Insights into Nanoindentation-Based Adhesion Testing
JOM, Vol. 69 Issue 11 (2017) 2237-2245

Publication E
S. Jakob, M. J. Pfeifenberger, A. Hohenwarter, R. Pippan
Femtosecond laser machining for characterization of local mechanical properties of biomaterials: a case study on wood
Science and Technology of Advanced Materials, Vol. 18 Issue 1 (2017) 574-583

Publication F
A. Kleinbichler, M. J. Pfeifenberger, J. Zechner, S. Wöhlert, M. J. Cordill
Scratch induced thin film buckling for quantitative adhesion measurements
Materials and Design, Vol. 155 (2018) 203-211

Publication G
V. Nikolić, J. Riesch, M. J. Pfeifenberger, R. Pippan
The effect of heat treatments on pure and potassium doped drawn tungsten wires: Part II Fracture properties
Materials Science and Engineering: A, Vol. 737 (2018) 434-447

Publication H
D. P. Gruber, J. Todt, N. Wöhrl, J. Zalesak, M. Tkadletz, A. Kubec, S. Niese, M. Burghammer, M. Rosenthal, H. Sternschulte, M. J. Pfeifenberger, B. Sartory, J. Keckes
Gradients of microstructure, stresses and mechanical properties in a multi-layered diamond thin film revealed by correlative cross-sectional nano-analytics
Carbon, Vol. 144 (2019) 666-674

Publication I
M. Zhao, I. Issa, M. J. Pfeifenberger, M. Wurmshuber, D. Kiener
Tailoring ultra-strong nanocrystalline tungsten nanofoams by reverse phase dissolution
Acta Materialia, under review

Remark

In the appended papers, myself, Manuel J. Pfeifenberger, developed the laser system, performed all experiments, the data analyses and the composition of the publications with the following exceptions:

- In **Publication A**
  Dipl.-Ing. Melanie Mangang and Dr. Wilhelm Pfleging performed initial parameter tests for the laser processing. Dr. Stefan Wurster helped developing the laser setup. Dr. Jens Reiser contributed ideas for publication and fruitful discussions.
- In **Publication B**
  Dipl.-Ing. Gabor Milassin performed the electron irradiation of the sample material. Dr. Barbara Putz helped with the verification of the testing results. Dr. Christopher O. A. Semprimoschnig contributed the basic ideas for publication and helpful discussions.
- In **Publication C**
  Dr. Stanislav Žák performed the FE simulations. Dr. Vladica Nikolić contributed to the conceptualization of the experiments as well as the writing of the paper. Dr. Anton Hohenwarter supported the execution of the experiments.
- My supervisor Prof. Dr. Reinhard Pippan, Assoz. Prof. Dr. Daniel Kiener and Dr. Anton Hohenwarter contributed to the papers by giving the basic ideas for the publications, helpful discussions of the results, and essential support during the preparation.

A

The use of femtosecond laser ablation as novel tool for rapid micro-mechanical sample preparation

Manuel J. Pfeifenberger [1,*], Melanie Mangang [2], Stefan Wurster [3], Jens Reiser [2], Anton Hohenwarter [3], Wilhelm Pfleging [4], Daniel Kiener [3], Reinhard Pippan [1]

[1] Erich Schmid Institute of Materials Science, Austrian Academy of Sciences, 8700 Leoben, Austria
[2] Institute for Applied Materials - Applied Materials Physics, Karlsruhe Institute of Technology, 76021 Karlsruhe, Germany
[3] Department Materials Physics, University of Leoben, 8700 Leoben, Austria
[4] Karlsruhe Nano Micro Facility, Karlsruhe Institute of Technology, 76344 Egg.-Leopoldshafen, Germany

Abstract

The focused ion beam technique has become a standard tool for micro-mechanical sample preparation in the last decade due to its high precision and general applicability in material removal. Besides disadvantages such as possible ion damage and high operation costs especially the characteristically small removal rates represent a bottleneck for this application. In contrast, femtosecond lasers provide material removal rates orders of magnitude higher, with small or ideally without thermal impact on the surrounding material. Hence, a combination of these two methods offers an ideal tool for time-efficient, micrometer-sized sample preparation. A prototype implementing this idea is presented here in combination with a case study. Cantilevers with a length of several hundred micrometers were machined into 25 μm, 50 μm and 100 μm thick, cold rolled tungsten foils. Scanning electron microscopy analyses reveal the influence of laser parameters and different scanning routines on the resulting sample quality and the effect of the laser pulse length (femtoseconds

versus nanoseconds) on the ultra-fine grained microstructure. Finally, the performance for unprecedented rapid sample preparation is demonstrated with a sample array consisting of 100 cantilevers with a dimension of 420x60x25 μm^3 processed in only half an hour, opening completely new testing possibilities.

A.1 Introduction

Mechanical experiments with specimens in the size regime between several hundred nanometers and some hundred micrometers become more and more important in order to achieve a better understanding of local mechanical properties and hence the mechanisms determining the materials' behaviour on these length scales [1–3]. Furthermore, the development and usage of small medical devices, micro-electro mechanical systems and nano-composites increase the relevance of the knowledge of the materials' properties at these small dimensions [4, 5]. In addition, novel fundamental research approaches conduct micro-experiments, in order to e.g. validate multi-scale modelling approaches [6] or to determine the controlling mechanism of the brittle-to-ductile transition [7].

The state-of-the-art fabrication technique for the preparation of miniaturized mechanical samples is the focused ion beam (FIB) machining. Up to a sample size of few tens of micrometer the FIB technique offers an ideal tool in terms of variability and further provides high precision down to the sub-micrometer domain [8–10]. Utilizing this technique for micro-mechanics provided the basis for the development of various miniaturized testing concepts and sample geometries [11]. For example, for the fabrication of specimens in the micrometer range, starting from thin sheets [12] or bulk materials [13], it presents nowadays a standard tool. Nevertheless, due to the low removal rates it impedes the fabrication of an adequate number of samples when sufficient statistical information is required and therefore becomes a costly and time-consuming method. Hence, the sample preparation employing the FIB technique represents a bottleneck for micro-mechanical studies. A further disadvantage of the FIB is the so-called ion-damage, which describes ion-induced defects in the near-surface layer caused by ion implantation [14, 15].

Especially the pre-preparation of samples usually requires the removal of a large amount of material and therefore is a time critical step. Due to the depletion of the ion source, these time intensive rough cuts make up a significant part of the operation expenses for a FIB system. High currents further lead to a high ion beam dosage and hence a strong influence on the material [16].

Wurster *et al.* [17] showed how the FIB cutting time can be considerably reduced by employing the ion slicing technique for the pre-preparation of test specimens. Additionally, this reduces the ion-induced damage in comparison to pure FIB milling. This damage reduction is based on a lower acceleration voltage and the use of argon

instead of gallium ions. However, there are still various disadvantages of the ion slicing technique. An irradiation damage may occur, the thickness of the specimen is limited to few microns only, an adequate masking technique has to be applied and complex geometries are difficult to fabricate [17].

Another technological advancement regarding the reduction of the FIB processing time is the application of recently developed xenon plasma sources for micromachining [18]. It enables faster material removal due to 1-2 orders of magnitude higher milling currents compared to the gallium FIB [19]. More recent studies also suggest that the influence on the mechanical properties of the processed material is less pronounced. Kwakman et al. noticed that the extent of the damage layer is reduced by approx. 25% [20]. Micro-compression experiments on polycrystalline aluminium performed by Xiao *et al.* [21] using pillars fabricated by a xenon and a gallium FIB exhibited a lowered yield strength for the samples prepared by the gallium FIB. However, the size of structures machinable with the xenon FIB is still limited to a few hundred micrometer.

On the meso-scale, i.e. in the range of 100 to $10,000\,\mu$m a precise and versatile method for sample preparation with limited influence on the material is not available. Suitable methods for this dimensions, such as micro-electrical discharge machining (μ-EDM) or micro-machining, influence the material either through heat or through plastic deformation. Kawakami *et al.*observed the generation of residual stresses in tungsten micro-beams due to the thermal impact of the μ-EDM cutting process [22]. The fabrication of micro-mechanical samples with μ-EDM has been conducted for example by Schmitt *et al.*, producing micro-cantilevers [23], or Uchic *et al.*, producing micro-compression samples [24]. For these specimens an additional preparation step was required due to the rough surface and the heat affected zone resulting from the μ-EDM processing. In [23] a FIB was employed to notch the cantilevers and to polish the cutting edges nearby the notch. Additional disadvantages of μ-EDM are the required fabrication of the electrode (for sinking μ-EDM), the subsequent wear of the electrode during processing, as well as the limitation of the technique to conductive materials [25].

Another widely used method for machining specimens on this small scale are lasers. Investigations on the capability of the laser for micro-machining started shortly after its invention [26]. However, the heat influence of continuous wave or short pulse (pulse duration > 10 ps [27]) lasers impedes the processing of sharp, well defined geometries [28] and therefore their applicability for micro-machining has been limited to cases, where a possible modification of the material is not critical. In contrast, ultrashort pulsed lasers (pulse duration $< 10\,$ps) enable laser micromachining of well defined geometries with a very good reproducibility [28, 29]. In recent investigations it has been shown that ultrashort pulsed laser materials processing achieved a high reliable standard which enables this technology to enter new and advanced industrial applications [30–32]. This is due the fact that the laser

pulse duration is significant below the heat diffusion time (>10-100 ps). The ultrashort pulse duration and the high intensity on the material surface lead to complete ionization of the irradiated material by non-linear effects. The irradiated material volume is removed from the surface before any heat diffusion or thermal damage and melting can occur.

When the laser beam is guided in parallel incidence to the ablated surface, the Gaussian intensity distribution of the laser beam [29] ensures that the ablation of the material happens at the threshold fluence, leading to optimal surface quality. On the other hand when the beam is guided perpendicularly to the ablated sample surface the resulting surface quality is lower and strongly depends on the applied process parameters. Further, a perpendicular incidence leads to an increased creation of dislocations and their density scales with the peak fluence of the laser pulse. For a parallel incidence the depth of the dislocation zone occur is significantly reduced [27]. In this case a high dislocation density is found within few 100 nm of the processed surface [33]. A similar dependence on the incidence angle has been found for the ion damage of FIB processing [14]. Femtosecond laser processed silicon exhibited an amorphized layer near the surface, extending 50 nm in depth [33].

With the advent of reliable ultrashort pulsed lasers their unique properties found wide interest in science and industry, and several applications have been developed since then. The various possibilities to structure and modify surfaces [34] can be used e.g. to tune optical properties of metal surfaces [35] or to reduce the reflectivity of silicon photovoltaic cells [36]. Furthermore, due to the feasiblity of ablating various materials, the capability for micro-machining of ultrashort pulsed laser ablation has been investigated for e.g. metals [37–39], biomaterials [40, 41], dielectrics [42], semiconductors [43, 44] or polymers [45].

Comparing the laser ablation to the standard gallium FIB technique, its ablation rate is 4-6 orders of magnitude higher. Also the ablation rate of a xenon FIB is still 2-3 orders of magnitude below the achievable rates of an ultrashort pulsed laser [27]. However, compared to the FIB the laser exhibits a reduced precision. One reason for this is the large spot diameter of approximately 20 μm, which is due to the scan optics setup used in this study. It is approx. 3 orders of magnitude larger than the spot size of a gallium FIB at 1 nA [19]. By using fixed optics and a positioning stage the precision can be improved. A main challenge that arises when samples are prepared with the ultrashort pulsed laser is the creation of so-called laser induced periodic surface structures (LIPSS). These LIPSS are an inherent feature of ultrashort pulsed laser processing. An overview of the size and orientation of the ripple-like structures for different materials is given in [46]. For linear polarized light the ripples are mostly oriented perpendicularly to the polarization of the laser [46]. For circular polarization the surface features exhibit a dot-like structure [47].

Due to the high precision of the FIB technique and the high ablation rates of the ultrashort pulsed laser technique, a combination of both methods yields a powerful

device for machining from the micro- to the meso-scale. The addition of a scanning electron microscope (SEM) allows for an immediate analysis of the processed specimens. Such a combination has already been realised by Echlin et al. [27, 48]. They built a setup for femtosecond laser ablation in-situ in a SEM to perform rapid 3D material analysis. A further assessment of combining the nano- or femtosecond laser technique with either a xenon or a gallium FIB has been conducted by Kwakman et al. [20].

As outlined before, the properties of ultrashort pulsed lasers are appealing for the fabrication of micro-mechanical test samples. To date, this application has been rarely investigated. Lim et al. studied the fabrication of micro-pillars on bovine cortical bone [41]. Very recently, in macroscopic mechanical tests femtosecond lasers have been successfully employed for introducing notches into single edge notched beam samples [49, 50].

The aim of this paper is to establish and to assess femtosecond (ultrashort) pulsed laser processing as a novel technique for the fabrication of micro-mechanical samples. In the following an overview of the combined SEM/FIB - femtosecond laser system is given. Then the performance of the femtosecond laser for the fabrication of micro-cantilevers is assessed and process parameters are optimized in terms of redeposition and surface quality. In addition, the quality and the microstructure of samples processed by nanosecond and femtosecond laser radiation is compared. Finally the question if femtosecond laser micro-machining allows the mass-production of micro-mechanical samples is answered.

A.2 Experimental

In this study three different pulsed laser sources were used. The specifications of these lasers are summarized in Table A.1. The specifications include the maximum average power P_{max}, the wavelength λ, the maximum pulse repetition rate R_{max} and the pulse duration t_p.

	Laser I	Laser II	Laser III
t_p	0.35 - 10 ps	4-20 ns	318 fs
P_{max} [W]	20	2.2	4
R_{max} [MHz]	2	0.12	1
λ [nm]	1030, 515, 343	355	1030, 515, 343
d_0 [μm]	35	27	25

Table A.1 Specifications of the three laser sources which were used in this study.

Initial investigations have been performed at the Karlsruhe Institute of Technology at the Karlsruhe Nano Micro Facility (KNMF) by employing a micro- machining

workstation (PS450-TO, Optec, Frameries, Belgium). This workstation is equipped with an ultrashort pulsed laser (Tangerine, Amplitude Systèmes, Pessac, France - Laser I in Table A.1). The laser beam is scanned across the sample surface employing a scan head (RhotorTM Laser Deflection Systems, Newson Engineering BV, Dendermonde, Belgium) and finally focused by a f-theta lens with 100 mm focal length.

Further tests and analyses have been conducted using a femtosecond laser system at the Erich Schmid Institute of Materials Science and the Materials Physics Department of the University of Leoben.

A.2.1 System design

The basis of the new femtosecond laser system is the Auriga Laser platform (Zeiss, Oberkochen, Germany - concept of the platform; see [51]). The modified setup is displayed in Fig. A.1. It consists of two vacuum chambers separated via an airlock. The main chamber (Fig. A.1 - a) contains the FIB and the SEM gun in a standard cross beam implementation. The laser processing is conducted in the separated second chamber (Fig. A.1 - b). Both chambers as well as the laser unit (Fig. A.1 - e) and all optical components are mounted on the same active air suspension for damping. The separation of the two chambers has the advantage that the high amount of ablated material during the laser processing does not contaminate the main chamber. Nevertheless, this setup allows femtosecond laser processing and successive SEM analysis or FIB cutting without leaving the vacuum state. An additional advantage is the possibility to use the laser in air or under inert gas conditions. This is especially of great interest, when working on bio-materials. The nanosecond laser (Laser II in Table A.1) originally used in the commercial Zeiss system is replaced by a femtosecond laser (Origami 10 XP, Onefive GmbH, Regensdorf, Switzerland - Laser III in Table A.1).

A look into the optical unit (Fig. A.1 - d) and the scan unit (Fig. A.1 - c) provides details on the beam path (Fig. A.2). The orientation of the laser unit causes that the separate exit windows of the three wavelengths are located on different height levels. By employing a periscope (Fig. A.2 - b) equipped with mirrors, designed for femtosecond laser pulses, all beams are guided along the same path through the beam expander (Fig. A.2 - c). The lower mirror of the periscope can be moved into and out of the beam path by a flip mount. The mirror positioned in the beam path is shown in the inset in Fig. A.2. After passing the beam expander, the laser beam is guided into the processing chamber via a scan unit (intelliscan III 10, SCANLAB AG, Puchheim, Germany), employing two perpendicularly oriented femtosecond mirrors (Fig. A.2 - d), which are driven by galvanometers. This scan unit allows for a scanning area of 50×50 mm^2 and a relative positioning accuracy of about 0.3 μm at the sample surface. The scanning principle enables the fabrication of

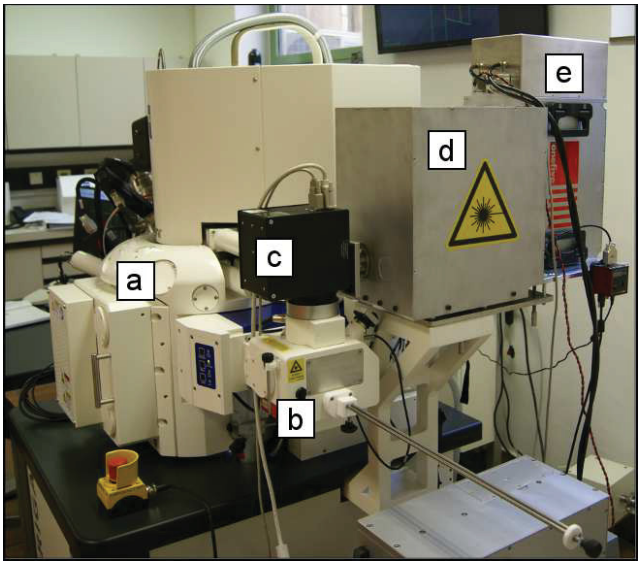

Figure A.1 System setup with main FIB/SEM chamber (a), laser processing chamber (b), scan unit (c), optical unit (d) and femtosecond laser unit (e).

arbitrary geometries, which are defined using a computer-aided design programme. The objective lens which finally focuses the laser beam onto the sample is a f-theta lens (Sill Optics GmbH, Wendelstein, Germany) ensuring a flat image plane and therefore a constant focal width across the scan area (Fig. A.2 - e,f). The used objective has a working distance of 145.7 mm. The focal diameter on the sample is adjusted by the beam expander, consisting of an uncoated dispersing lens and an uncoated collecting lens, located between the periscope and the scan unit. The position of the minimal focal diameter is defined by the distance between these two lenses (Fig. A.3). The position of the dispersal lens can be varied and is controlled by a stepper motor actuator. This setup allows a shift of the position of the minimal focal diameter of approximately 30 mm and therefore allows the same variance in sample height.

The laser system offers five parameters to be adjusted: The average laser pulse power and the laser pulse repetition rate. Further a shutter allows to adjust the number of transmitted pulses. In addition, the laser scanning speed across the sample surface and the number of repetitions of each laser scan line are variable.

A spot size evaluation on the modified system was performed according to [52]. The determined spot diameter was $24.5 \pm 0.3\,\mu$m. The ablation threshold fluence yielded 0.20 ± 0.01 J/cm^2 for the tungsten foils. This is in good agreement with Byskov-Nielsen et al. [53], considering the linear dependence of the threshold fluence on the wavelength for sub-picosecond pulses [54]. Byskov-Nielsen et al. [53] found

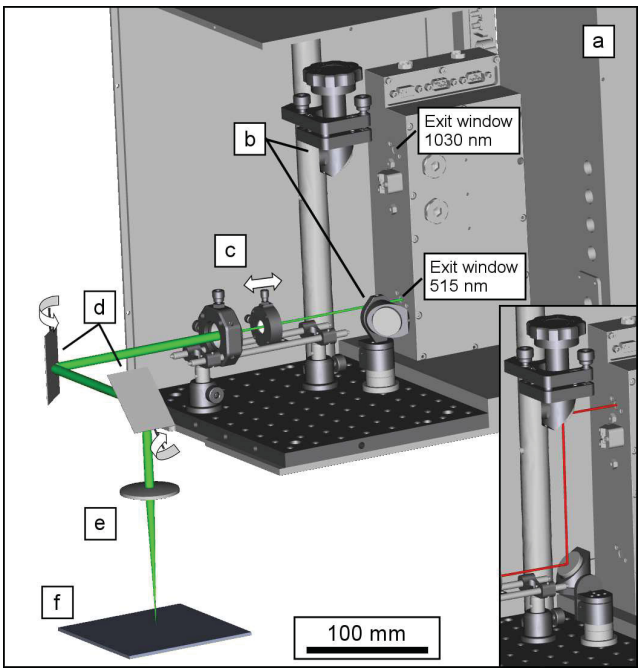

Figure A.2 Detailed view of the beam path starting from the laser unit (a) along the beam expander (c), the mirrors of the scanning unit (d) and the objective lens (e). The exit windows for the wavelengths of 515 nm and 1030 nm are located on different heights. The periscope (b) optionally guides the beam with a wavelength of 1030 nm into the beam expander (shown in inset).

for tungsten a single pulse threshold of 0.44 ± 0.02 J/cm^2 for femtosecond laser ablation with a wavelength of 800 nm. The same analysis for the nanosecond laser operating with a wavelength of 355 nm provided a spot diameter of 27.4 ± 1.9 μm and a fluence threshold of 5.8 ± 1.0 J/cm^2. This threshold value agrees well with the values listed in [55], where thresholds of 8.32 J/cm^2 and 4.28 J/cm^2 have been found for wavelengths of 266 nm and 532 nm respectively.

A.2.2 Material and methods

In this study cold rolled tungsten foils with a thickness of either 25 μm, 50 μm or 100 μm were used as sample material. These foils exhibit an ultra fine grained microstructure and excellent ductility. Therefore, they are promising for the use as structural material in high temperature applications [56]. The enhanced mechanical properties are governed by the microstructure of the foil. It is of great importance to prevent the material from being damaged by melting, recrystallization or by crack formation during preparation [56]. Therefore, the use of a femtosecond laser seems

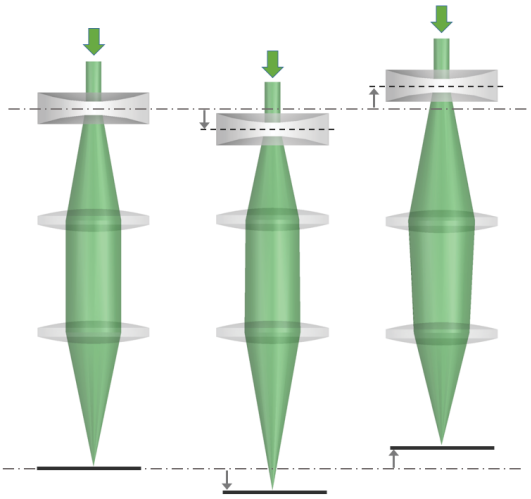

Figure A.3 Working principle of the beam expander. Changing the distance between the dispersal and collecting lens, varies the position of the focal plane.

to be an appropriate tool in order to avoid a thermal impact on the material during the ablation process. Tungsten additionally represents a challenging material for FIB processing due to its low sputter yield [57] and is therefore an ideal example for the investigation of the ablation capability and efficiency of a femtosecond laser. Cantilevers are a widely used specimen type for micro-mechanical testing, hence, this geometry has been selected to study the performance of the new system.

For the electron backscatter diffraction (EBSD) data acquisition a scanning electron microscope (LEO 1525, Zeiss, Oberkochen, Germany) with an EBSD detector (EDAX Inc., New Jersey, USA) has been used. The data have been analysed with the EDAX OIM Data Analysis software. For the scans a step size of 50 nm and an acceleration voltage of 20 kV was chosen.

A.3 Results and discussion

A.3.1 Scanning routine and parameter optimization

The initial tests at KIT-KNMF demonstrated the feasibility of femtosecond laser processing for the production of micro cantilevers made of tungsten. Samples were cut into foils, fabricated by cold rolling, with thicknesses of 25 μm, 50 μm or 100 μm. Fig. A.4 shows cantilevers cut through the thickness of these foils. The laser parameters used for these samples are listed in Table A.2. The respective scan pattern is displayed in Fig. A.5a. The same pattern was scanned multiple times to ensure full penetration. The number of scan repetitions is given in Table A.2. In these samples

also a notch was introduced using the femtosecond laser. Because of the significantly larger tip radius compared to a FIB notch, the laser processing of notches has not been further investigated in this study.

In the used configuration the laser beam is oriented perpendicularly to the foil. Therefore the incidence of the laser beam with respect to the ablated material is normal at the beginning of the process. After the penetration of the foil a glancing incidence is achieved.

Foil thickness	25 μm	50 μm	100 μm
Fluence [J/cm^2]	0.7	1.0	1.6
Repetition rate [kHz]	20	20	40
Scan speed [mm/s]	100	100	50
Scan repetitions	150	300	400

Table A.2 Parameters for the cantilevers cut in foils with different thicknesses using a femtosecond laser with a wavelength of 1030 nm and a laser pulse duration of 380 fs (Laser I in Table A.1). The resulting samples are shown in Fig. A.4.

The cutting edges exhibited a wavy structure towards the bottom. Particularly for the 100 μm thick sample an array of cavities is observed. This is on the one hand due to a non-optimal overlap of successive laser pulses, because of the high scanning speeds used for the 25 μm and 50 μm samples. On the other hand, cutting only the contour of the desired shape, as shown in Fig. A.5a, is unfavourable for an increasing foil thickness because the redeposited material from preceding scanning steps increasingly hinders material transport away from the processing region and therefore impedes an even ablation. Further, the U-shaped remnant piece will move or fall out during the last scan repetitions and thus change the conditions for the interaction of the laser with the material. The remnant piece can remain stuck, especially in thicker foils, and has to be removed via a follow-up treatment. Though, the scan pattern in Fig. A.5a yields the lowest scan time for the intended cantilever geometry. The generation of debris on the surface lowers the surface quality as displayed in Fig. A.4. Shaheen et al. found for an increasing fluence an increase in the amount of generated debris. Further re-solidified molten material occurs at high fluences, though, none was observed in the low fluence regime [58]. For an increasing foil thickness, more ablated material and therefore more debris on the top face of the cantilever was found. The generated debris leads to a change of colour around the processed area. However, it can be removed nearly completely by cleaning the sample in a ultrasonic bath filled with soap water.

To further enhance the surface quality of the cutting edge a second scan pattern has been applied. It is displayed in Fig. A.5b. Using this scan pattern also avoids any remnant piece of getting stuck, because here the whole U-shape is removed during processing. Nevertheless, due to the ablation of a larger amount of material more

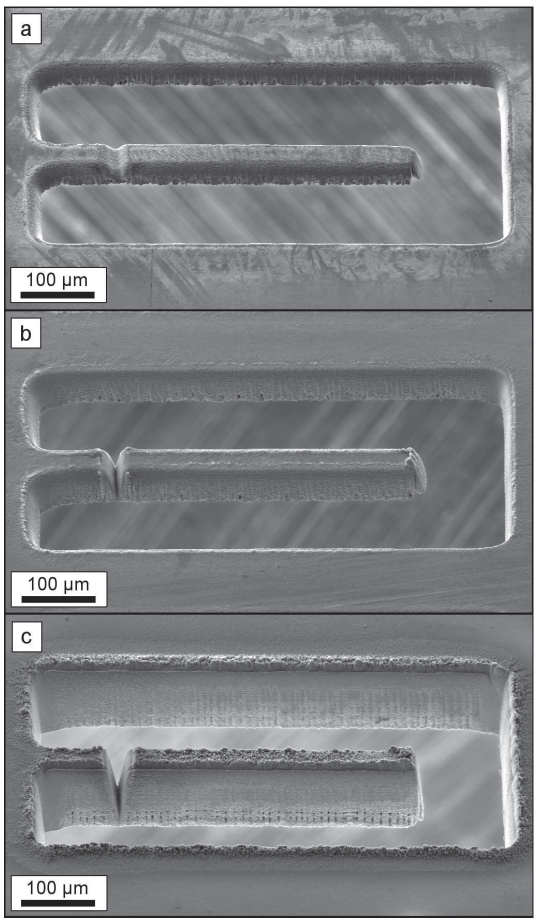

Figure A.4 Cantilever cut with a femtosecond laser (KIT-KNMF) in foils with (a) 25 μm, (b) 50 μm and (c) 100 μm thickness. The used scan pattern is shown in Fig. 5a. The number of scan passes are listed in Table 2. For this samples also the notch was laser processed.

debris is generated.

With the modified prototype multiple scanning routines and parameter tests were performed to identify their influence on the resulting sample. The 25 μm thick foils served as samples for these experiments. Fig. A.6 shows the rectangular scan pattern employed for these experiments. The pattern has been chosen with the goal to remove a certain area of the sample to successively enable the fabrication of free-standing specimens. Starting from the lower right corner each line is scanned from right to left. After a certain number of repetitions per line the beam moves to the next upper line. In total 10 lines with a distance of 8 μm in between were cut. A distance of 8 μm ensures sufficient overlap between the lines. This pattern

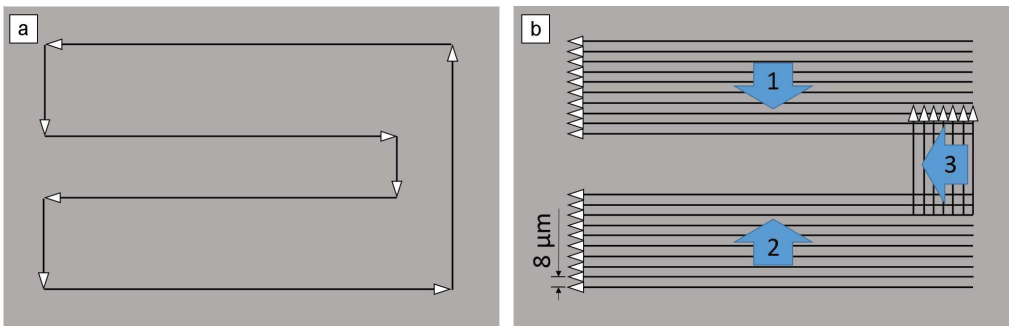

Figure A.5 The scan strategies for the fabrication of cantilevers. The U-shape can either be cut out by a single contour cut (a) or by removing the whole material by scanning across the respective area (b). The narrow arrows indicate the lines of the laser cuts and the broad arrows indicates the scan direction.

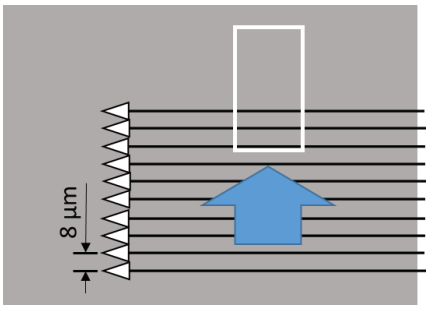

Figure A.6 The scan pattern for the parameter tests. The horizontal arrows indicate the lines of the laser cuts and the broad arrow the scan direction. The white rectangle marks the area of interest shown in Fig. A.7.

was used to create the cuts shown in Fig. A.7 and Fig. A.8. For these tests a laser fluence of 1.1 J/cm^2, a scan speed of 1 mm/s and a laser pulse repetition rate of 100 kHz have been used. The micrographs in Fig. A.7 display the cut edges on the top side of the scan pattern. These cuts were fabricated with a repetition number of 1, 2, 3, 10, 100, 250 for each line. It was found that for this parameter set with 10 line repetitions the surface quality of the cut edge does not significantly increase any more. For higher repetition numbers periodic structures also start to form on the top face of the sample (Fig. A.7 (e),(f)).

Besides enhancing the surface quality of the cut edges, also the amount of redeposited material needs to be reduced. In Fig. A.8 the processed areas are viewed in total. For the cut in Fig. A.8a each line of the scan pattern was repeated 20 times. It exhibits a significant redeposition of ablated material on the lower edge. For the sample in Fig. A.8b each line of the scan pattern was repeated 5 times and

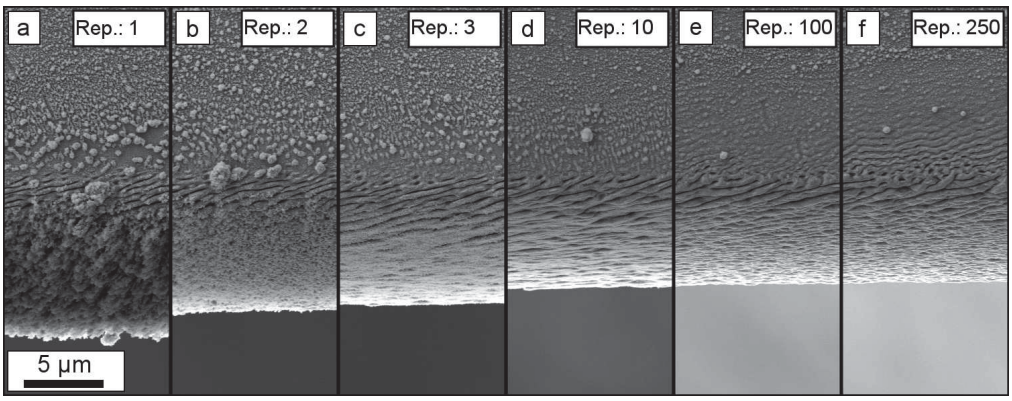

Figure A.7 Samples cut in a 25 μm thick foil using the scan pattern in Fig. A.6 with a different number of repetitions per scan line in a single pass. Increasing the number of repetitions leads to a smoother cut edge and a reduced taper angle (a)-(c), but also to the occurrence of LIPSS on the top face of the sample for higher repetition numbers (e), (f).

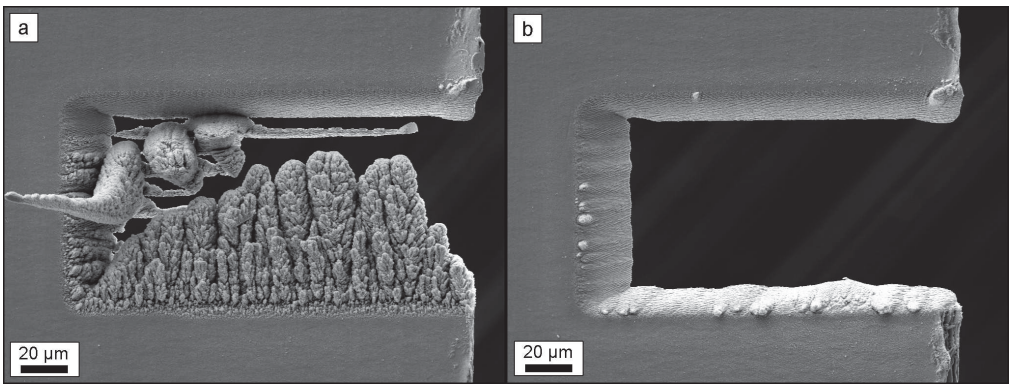

Figure A.8 The scan pattern displayed in Fig. A.6 is cut into a foil with a thickness of 25 μm. (a) Single pass scanning with 20 repetitions per line leads to an extensive redeposit of ablated material. (b) Multiple pass scanning (5 repetitions per line and 4 passes) minimizes redeposition.

additionally the whole scan pattern (Fig. A.6) was repeated in 4 passes. These tests exhibited that multiple passes significantly reduce the amount of redeposited material. This strategy is well known for the FIB technique, where multiple pass scanning is applied to minimize material redeposition [57].

A variation of the average laser power showed that after the power suffices to penetrate the foil a further increase leads initially to a decrease of the taper angle at the cut edges. Finally, a saturation of the taper angle is observed with increasing laser power.

The findings in this section were considered when designing the scanning routine and choosing the parameters for the cantilever fabrication. For larger samples a combination of the patterns in Fig. A.5a and Fig. A.5b can be favourable, using first a contour shape for a rough cut followed by few parallel cuts to enhance surface quality of desired edges. This way the processing time required, when using the pattern in Fig. A.5b, can be reduced.

A.3.2 Comparison of nanosecond and femtosecond laser processing

In this section the results of processing with a nanosecond (Laser II in Tab. A.1) and a femtosecond laser (Laser III) are compared. The surface quality of the cut edges as well as the influence of the laser pulse duration on the microstructure were investigated. The process parameters are displayed in Table A.3. Although the average power of the nanosecond laser is higher, the peak power of the femtosecond laser pulses due to the much smaller pulse duration is approx. 3 orders of magnitude higher. For the nanosecond laser processing the scan pattern in Fig. A.5a was scanned in 2 passes. For the femtosecond laser processing the pattern in Fig. A.5b was scanned in 2 passes with 5 repetitions per line.

(see Tab. A.1)	ns-laser Laser II	fs-laser Laser III
Fluence [J/cm^2]	15.3	1.1
Repetition rate [kHz]	25	100
Scan speed [mm/s]	60	10

Table A.3 Parameters of the laser used for the fabrication of the cantilevers displayed in Fig. A.9 and Fig. A.10

Fig. A.9a shows a cantilever processed with the nanosecond laser. Machining with the nanosecond laser leads to extensive debris formation on the top face (Fig. A.9b). This redeposition is produced by the ejection of molten material [58]. The surface of the cut edge shows melted structures and a distinct burr as displayed in Fig. A.9c. Fig. A.10a shows a cantilever processed with the femtosecond laser. Compared to the nanosecond laser machining less and smaller debris is generated on the top face (Fig. A.10b). Further, the cut edge of the femtosecond laser cut is smoother and no burr can be found (Fig. A.10a and c). Although the surface quality is improved employing femtosecond laser pulses, a completely structure free surface can not be obtained due to the occurrence of the characteristic LIPSS (Fig. A.10c).

Investigations of the microstructure underneath the edge of the laser cut yield a significant difference between the samples processed with the nanosecond and the femtosecond laser, respectively. Inverse pole figure maps were obtained from EBSD analyses of FIB polished surfaces which were oriented perpendicular to the laser cut.

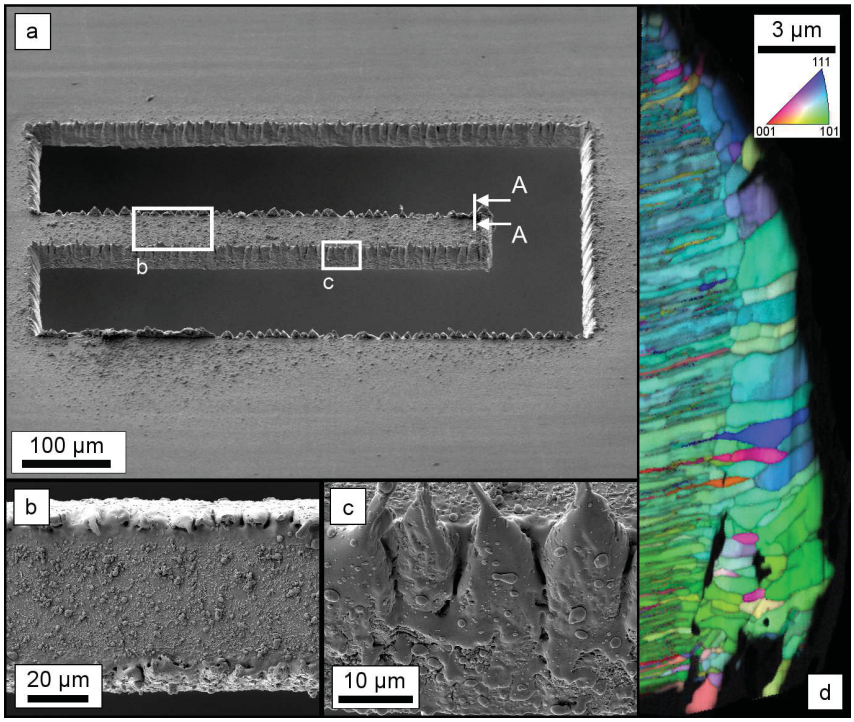

Figure A.9 A cantilever fabricated by a nanosecond laser in a foil with a thickness of 25 μm is displayed in (a). The scan pattern in Fig. A.5a was scanned in 2 passes. The magnified top view (b) shows rough debris. The magnification of the cut edge shows a melted surface and a distinct burr (c). An EBSD analysis of the cross-section A-A indicated in (a) reveals coarsened and equiaxed grains in the heat influenced zone (d). The inset triangle shows the colour coding of the crystal orientation with respect to an external reference.

The results are presented in Fig. A.9d and Fig. A.10d. The inset shows the colour coding of the EBSD pattern, which describes the crystal orientation with respect to an external reference. The greyscale of the maps has been coded with the image quality. Due to the rolling fabrication of the tungsten foils the grains initially feature an elongated structure with a grain thickness of approximately $300 - 500$ nm and a high defect density giving rise to a low grey value. The microstructure of the nanosecond laser processed samples exhibits coarsened, nearly equiaxed grains in the vicinity of the cut edge (Fig. A.9d). The coarsening can be explained by a recrystallisation process, which followed after the heat influence exerted by the nanosecond laser pulses. For the employed parameter set coarsening is found up to approximately 4 μm underneath the cut surface. Furthermore, due to the recrystallisation the defect density is reduced, resulting in a brighter image near to On

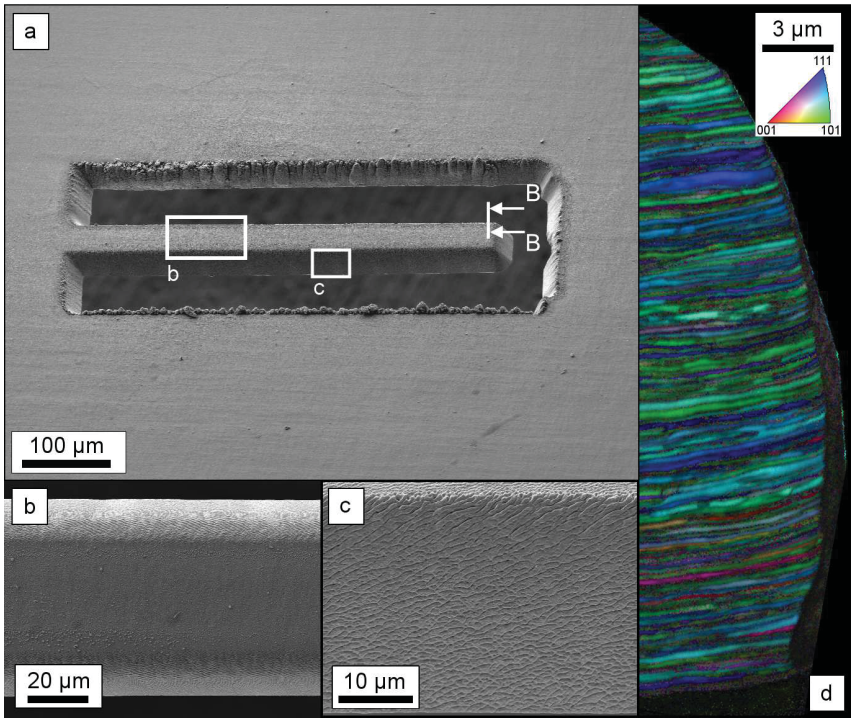

Figure A.10 A cantilever fabricated by a femtosecond laser in a foil with a thickness of 25 μm is shown in (a). The scan pattern in Fig. A.5b was scanned in 2 passes with 5 repetitions per line. In the magnified top view (b) less debris is found than for the nanosecond laser processing. The magnification of the cut edge exhibits the characteristic laser induced periodic structures (c). An EBSD analysis of the cross-section B-B indicated in (a) reveals no grain coarsening near the cut edge (d). The inset triangle shows the colour coding of the crystal orientation with respect to an external reference.

the contrary the femtosecond laser processed samples show no change in the grain shape and in the EBSD pattern quality due to recovery as shown in Fig. A.10d.

To evaluate the extent of the periodic surface structures a FIB cross-section located on the cut edge was analysed as shown in Fig. A.11. The LIPSS show a periodicity of about 250 nm and a depth of about 100 nm. This is in good agreement with the LIPSS dimensions Echlin et al. [33] found for various materials. Furthermore, the microstructure a few tens of nm underneath the LIPSS reveals no change. While representing no impediment for example for tensile testing of ductile materials, this surface roughness will inhibit such tests for brittle materials. Nevertheless, for fracture experiments the LIPSS will be of no relevance, because the required notch exceeds their dimension by far.

Fig. A.12 emphasizes the efficiency of the femtosecond laser system for sample

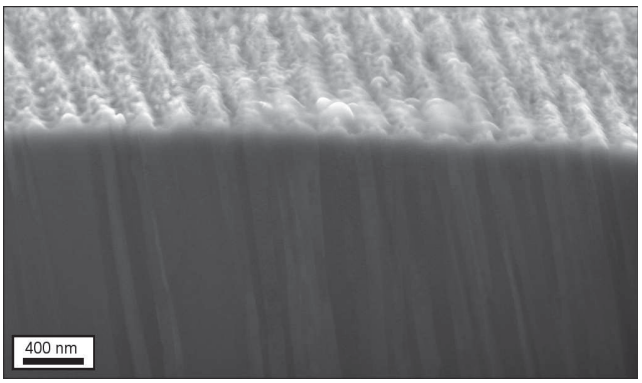

Figure A.11 A FIB cross-section through the LIPSS on the cut edge shows a periodicity of the undulating structures of approximately 250 nm. The depth is about 100 nm. The elongated grains due to the rolling fabrication are visible and reveal no change in structure underneath the LIPSS.

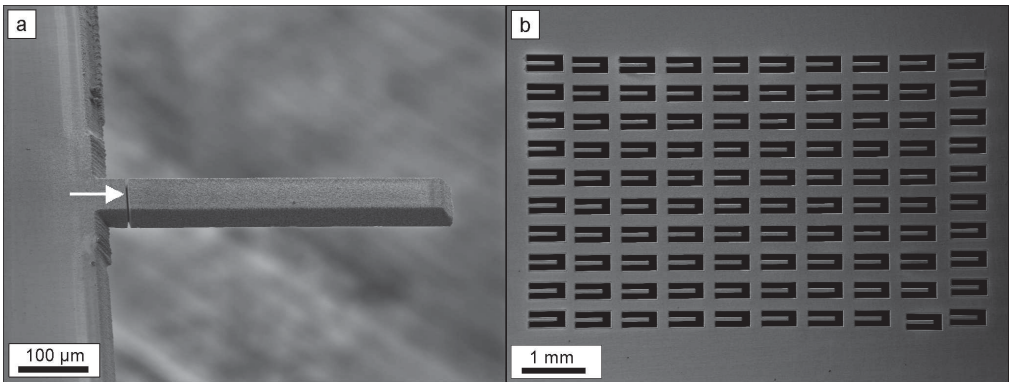

Figure A.12 (a) Femtosecond laser cut cantilever with a notch introduced by a FIB (indicated by white arrow). (b) The micrograph shows 100 cantilevers with a length of 420 μm and a width of 60 μm prepared in only half an hour in a tungsten foil with 25 μm thickness.

preparation. The cantilever shown in Fig. A.12a was fabricated using the laser, while the notch was introduced employing the FIB. The laser processing step takes approximately 20 s. A set consisting of 100 cantilevers with a dimension of 420x60x25 μm^3, as shown in Fig. A.12b, takes therefore only about half an hour. The complete machining by FIB would require about 1 year of continuous milling, assuming a high ablation rate of 10 $\mu m^3/s$.

A.4 Conclusions

In this study, the feasibility of employing a femtosecond laser for the rapid fabrication of micro-mechanical test structures, in the particular case cantilevers in tungsten foils, with lengths up to several hundred micrometers has been demonstrated. For this purpose a device combining a FIB and a SEM in a standard crossbeam implementation and a nanosecond laser was modified to be operated with a femtosecond laser. The system enables fast material removal by a femtosecond laser and precise FIB end-processing as well as scanning electron analyses without any need of interrupting the vacuum conditions. Furthermore, the system design with a separated laser chamber allows processing in air or under certain inert gas conditions, which is of interest when e.g. working on bio-materials. The femtosecond laser processing enables a material independent ablation without significant heat impact on the surrounding material. Employing a scan unit to move the beam across the sample offers fast processing and a high variability in sample geometries, for example round pillars or tensile specimens.

The authors are sure that this novel method will find wide application for unprecedented fast pre-preparation and preparation of samples on the micro-scale. Furthermore, it represents a unique and versatile tool for producing samples in the meso-scale up to few 10 mm dimensions. The rapid processing can be regarded as a mass production technique for micro samples and therefore helps to facilitate the acquisition of sufficient statistical information for micro-mechanical experiments. It will contribute to relieve the bottleneck posed by the established FIB technique for micro-mechanical sample preparation and testing.

Acknowledgments

KIT has received funding from the European Unions Horizon 2020 research and innovation programme under the Marie Sklodowska-Curie grant agreement no. 644971. In addition, the support for femtosecond laser processing by the Karlsruhe Nano Micro Facility (http://www.knmf.kit.edu/), a Helmholtz research infrastructure at KIT is gratefully acknowledged.

The authors thank the Zeiss team in Oberkochen, especially Dr. Hiller, for their support in issues regarding the modification of the Zeiss Auriga Laser.

Bibliography to publication A

[1] J. R. Greer and J. T. M. De Hosson, "Plasticity in small-sized metallic systems: Intrinsic versus extrinsic size effect," *Progress in Materials Science*, vol. 56, pp. 654–724, Aug. 2011.

[2] M. D. Uchic, D. M. Dimiduk, J. N. Florando, and W. D. Nix, "Sample Dimensions Influence Strength and Crystal Plasticity," *Science*, vol. 305, pp. 986–989, Aug. 2004.

[3] M. D. Uchic, P. A. Shade, and D. M. Dimiduk, "Plasticity of Micrometer-Scale Single Crystals in Compression," *Annual Review of Materials Research*, vol. 39, no. 1, pp. 361–386, 2009.

[4] A. C. R. Grayson, R. S. Shawgo, A. M. Johnson, N. T. Flynn, Y. Li, M. J. Cima, and R. Langer, "A BioMEMS review: MEMS technology for physiologically integrated devices," *Proceedings of the IEEE*, vol. 92, pp. 6–21, Jan. 2004.

[5] S. A. Wilson, R. P. J. Jourdain, Q. Zhang, R. A. Dorey, C. R. Bowen, M. Willander, Q. U. Wahab, M. Willander, S. M. Al-hilli, O. Nur, E. Quandt, C. Johansson, E. Pagounis, M. Kohl, J. Matovic, B. Samel, W. van der Wijngaart, E. W. H. Jager, D. Carlsson, Z. Djinovic, M. Wegener, C. Moldovan, R. Iosub, E. Abad, M. Wendlandt, C. Rusu, and K. Persson, "New materials for micro-scale sensors and actuators: An engineering review," *Materials Science and Engineering: R: Reports*, vol. 56, pp. 1–129, June 2007.

[6] N. M. Ghoniem, E. P. Busso, N. Kioussis, and H. Huang, "Multiscale modelling of nanomechanics and micromechanics: an overview," *Philosophical Magazine*, vol. 83, pp. 3475–3528, Nov. 2003.

[7] H. Li and F. Ebrahimi, "Ductile-to-Brittle Transition in Nanocrystalline Metals," *Adv. Mater.*, vol. 17, pp. 1969–1972, Aug. 2005.

[8] M. W. Phaneuf, "Applications of focused ion beam microscopy to materials science specimens," *Micron*, vol. 30, pp. 277–288, June 1999.

[9] J. Melngailis, "Focused ion beam technology and applications," *Journal of Vacuum Science & Technology B*, vol. 5, pp. 469–495, Mar. 1987.

[10] C. A. Volkert and A. M. Minor, "Focused Ion Beam Microscopy and Micromachining," *MRS Bulletin*, vol. 32, pp. 389–399, May 2007.

[11] D. Kiener, C. Motz, G. Dehm, and R. Pippan, "Overview on established and novel FIB based miniaturized mechanical testing using in-situ SEM," *International Journal of Materials Research*, vol. 100, no. 8, pp. 1074–1087, 2009.

[12] J. McCarthy, Z. Pei, M. Becker, and D. Atteridge, "FIB micromachined submicron thickness cantilevers for the study of thin film properties," *Thin Solid Films*, vol. 358, pp. 146–151, Jan. 2000.

[13] D. Di Maio and S. Roberts, "Measuring fracture toughness of coatings using focused-ion-beam-machined microbeams," *Journal of Materials Research*, vol. 20, pp. 299–302, Feb. 2005.

[14] D. Kiener, C. Motz, M. Rester, M. Jenko, and G. Dehm, "FIB damage of Cu and possible consequences for miniaturized mechanical tests," *Materials Science and Engineering: A*, vol. 459, pp. 262–272, June 2007.

[15] S. Rubanov and P. R. Munroe, "FIB-induced damage in silicon," *Journal of Microscopy*, vol. 214, pp. 213–221, June 2004.

[16] J. Hütsch and E. T. Lilleodden, "The influence of focused-ion beam preparation technique on microcompression investigations: Lathe vs. annular milling," *Scripta Materialia*, vol. 77, pp. 49–51, Apr. 2014.

[17] S. Wurster, M. Jenko, C. Motz, and R. Pippan, "Micrometer-Sized Specimen Preparation Based on Ion Slicing Technique," *Advanced Engineering Materials*, vol. 12, no. 12, pp. 61 – 64, 2010.

[18] N. S. Smith, W. P. Skoczylas, S. M. Kellogg, D. E. Kinion, P. P. Tesch, O. Sutherland, A. Aanesland, and R. W. Boswell, "High brightness inductively coupled plasma source for high current focused ion beam applications," *Journal of Vacuum Science & Technology B*, vol. 24, pp. 2902–2906, Nov. 2006.

[19] L. Kwakman, G. Franz, M. Taklo, A. Klumpp, and P. Ramm, "Characterization and failure analysis of 3d integrated systems using a novel plasma-FIB system," in *Frontiers of Characterization and Metrology for Nanoelectronics: 2011*, vol. 1395, pp. 269–273, 2011.

[20] L. Kwakman, M. Straw, G. Coustillier, M. Sentis, J. Beyersdorfer, J. Schischka, F. Naumann, and F. Altmann, "Sample preparation strategies for fast and effective failure analysis of 3d devices," in *ISTFA 2013: Proceedings from the 39th International Symposium for Testing and Failure Analysis*, pp. 17–26, ASM International, 2013.

[21] Y. Xiao, J. Wehrs, H. Ma, T. Al-Samman, S. Korte-Kerzel, M. Gken, J. Michler, R. Spolenak, and J. M. Wheeler, "Investigation of the deformation behavior of aluminum micropillars produced by focused ion beam machining using Ga and Xe ions," *ResearchGate*, Aug. 2016.

[22] T. Kawakami and M. Kunieda, "Study on Factors Determining Limits of Minimum Machinable Size in Micro EDM," *CIRP Annals - Manufacturing Technology*, vol. 54, pp. 167–170, Jan. 2005.

[23] N. Schmitt, C. Bohnert, C. Eberl, R. Schwaiger, S. Weygand, and O. Kraft, "Investigation of the fracture behavior of tungsten at the micro scale," *ICF Proceedings*, vol. 13th International Conf. on Fracture, Beijing, pp. 3342–3349, June 2013.

[24] M. D. Uchic and D. M. Dimiduk, "A methodology to investigate size scale effects in crystalline plasticity using uniaxial compression testing," *Materials Science and Engineering: A*, vol. 400401, pp. 268–278, July 2005.

[25] N. Mohd Abbas, D. G. Solomon, and M. Fuad Bahari, "A review on current research trends in electrical discharge machining (EDM)," *International Journal of Machine Tools and Manufacture*, vol. 47, pp. 1214–1228, June 2007.

[26] M. G. Cohen, R. A. Kaplan, and E. G. Arthurs, "Micro-materials processing," *Proceedings of the IEEE*, vol. 70, pp. 545–555, June 1982.

[27] M. P. Echlin, M. Straw, S. Randolph, J. Filevich, and T. M. Pollock, "The TriBeam system: Femtosecond laser ablation in situ SEM," *Materials Characterization*, vol. 100, pp. 1–12, Feb. 2015.

[28] B. N. Chichkov, C. Momma, S. Nolte, F. v. Alvensleben, and A. Tünnermann, "Femtosecond, picosecond and nanosecond laser ablation of solids," *Appl. Phys. A*, vol. 63, pp. 109–115, Aug. 1996.

[29] X. Liu, D. Du, and G. Mourou, "Laser ablation and micromachining with ultrashort laser pulses," *IEEE Journal of Quantum Electronics*, vol. 33, pp. 1706–1716, Oct. 1997.

[30] K. Sugioka, "Progress in ultrafast laser processing and future prospects," *Nanophotonics*, vol. 5, pp. 17–37, 2016.

[31] E. Mottay, X. Liu, H. Zhang, E. Mazur, R. Sanatinia, and W. Pfleging, "Industrial applications of ultrafast laser processing," *MRS Bulletin*, vol. 41, no. 12, pp. 984–992, 2016.

[32] P. Lu, R. J. K. Wood, M. G. Gee, L. Wang, and W. Pfleging, "The Friction Reducing Effect of Square-Shaped Surface Textures under Lubricated Line-Contacts - An Experimental Study," *Lubricants*, vol. 4, p. 26, July 2016.

[33] M. P. Echlin, M. S. Titus, M. Straw, P. Gumbsch, and T. M. Pollock, "Materials response to glancing incidence femtosecond laser ablation," *Acta Materialia*, vol. 124, pp. 37–46, Feb. 2017.

[34] K. M. T. Ahmmed, C. Grambow, and A.-M. Kietzig, "Fabrication of Micro/Nano Structures on Metals by Femtosecond Laser Micromachining," *Micromachines*, vol. 5, pp. 1219–1253, Nov. 2014.

[35] A. Y. Vorobyev and C. Guo, "Colorizing metals with femtosecond laser pulses," *Applied Physics Letters*, vol. 92, p. 041914, Jan. 2008.

[36] M. Halbwax, T. Sarnet, P. Delaporte, M. Sentis, H. Etienne, F. Torregrosa, V. Vervisch, I. Perichaud, and S. Martinuzzi, "Micro and nano-structuration of silicon by femtosecond laser: Application to silicon photovoltaic cells fabrication," *Thin Solid Films*, vol. 516, pp. 6791–6795, Aug. 2008.

[37] G. Kamlage, T. Bauer, A. Ostendorf, and B. N. Chichkov, "Deep drilling of metals by femtosecond laser pulses," *Appl Phys A*, vol. 77, no. 2, pp. 307–310, 2003.

[38] K. Furusawa, K. Takahashi, H. Kumagai, K. Midorikawa, and M. Obara, "Ablation characteristics of Au, Ag, and Cu metals using a femtosecond Ti:sapphire laser," *Appl Phys A*, vol. 69, pp. S359–S366, Dec. 1999.

[39] S. Ma, J. P. McDonald, B. Tryon, S. M. Yalisove, and T. M. Pollock, "Femtosecond Laser Ablation Regimes in a Single-Crystal Superalloy," *Metall and Mat Trans A*, vol. 38, pp. 2349–2357, Aug. 2007.

[40] N. Naderi, S. Legacey, and S. L. Chin, "Preliminary investigations of ultrafast intense laser wood processing," *Forest products journal*, vol. 49, pp. 72–76, 1999.

[41] Y. C. Lim, K. J. Altman, D. F. Farson, and K. M. Flores, "Micropillar fabrication on bovine cortical bone by direct-write femtosecond laser ablation," *J Biomed Opt*, vol. 14, p. 064021, Dec. 2009.

[42] M. D. Perry, B. C. Stuart, P. S. Banks, M. D. Feit, V. Yanovsky, and A. M. Rubenchik, "Ultrashort-pulse laser machining of dielectric materials," *Journal of Applied Physics*, vol. 85, pp. 6803–6810, May 1999.

[43] N. Bärsch, K. Körber, A. Ostendorf, and K. H. Tönshoff, "Ablation and cutting of planar silicon devices using femtosecond laser pulses," *Appl Phys A*, vol. 77, no. 2, pp. 237–242, 2003.

[44] T. Kim, H. S. Kim, M. Hetterich, D. Jones, J. M. Girkin, E. Bente, and M. D. Dawson, "Femtosecond laser machining of gallium nitride," *Materials Science and Engineering: B*, vol. 82, pp. 262–264, May 2001.

[45] M. H. H. Z. B. Wang, "Femtosecond laser ablation of polytetrafluoroethylene (Teflon) in ambient air," *Journal of Applied Physics*, vol. 93, no. 10, pp. 6375–6380, 2003.

[46] J. Bonse, J. Krüger, S. Höhm, and A. Rosenfeld, "Femtosecond laser-induced periodic surface structures," *Journal of Laser Applications*, vol. 24, p. 042006, Sept. 2012.

[47] O. Varlamova, F. Costache, M. Ratzke, and J. Reif, "Control parameters in pattern formation upon femtosecond laser ablation," *Applied Surface Science*, vol. 253, pp. 7932–7936, July 2007.

[48] M. P. Echlin, A. Mottura, C. J. Torbet, and T. M. Pollock, "A new TriBeam system for three-dimensional multimodal materials analysis," *Review of Scientific Instruments*, vol. 83, p. 023701, Feb. 2012.

[49] W. Zhao, P. Rao, and Z. Ling, "A new method for the preparation of ultrasharp V-notches to measure fracture toughness in ceramics," *Journal of the European Ceramic Society*, vol. 34, pp. 4059–4062, Dec. 2014.

[50] T. Palacios and J. Y. Pastor, "Influence of the notch root radius on the fracture toughness of brittle metals: Nanostructure tungsten alloy, a case study," *International Journal of Refractory Metals and Hard Materials*, vol. 52, pp. 44–49, Sept. 2015.

[51] R. Salzer and H. Stegmann, "Efficient and Precise Sample Preparation by Combination of Pulsed Laser Ablation and FIB Milling," *Microscopy and Microanalysis*, vol. 18, pp. 636–637, July 2012.

[52] J. M. Liu, "Simple technique for measurements of pulsed Gaussian-beam spot sizes," *Opt. Lett., OL*, vol. 7, pp. 196–198, May 1982.

[53] J. Byskov-Nielsen, J.-M. Savolainen, M. S. Christensen, and P. Balling, "Ultrashort pulse laser ablation of metals: threshold fluence, incubation coefficient and ablation rates," *Appl. Phys. A*, vol. 101, pp. 97–101, Oct. 2010.

[54] E. G. Gamaly, A. V. Rode, B. Luther-Davies, and V. T. Tikhonchuk, "Ablation of solids by femtosecond lasers: Ablation mechanism and ablation thresholds for metals and dielectrics," *Physics of Plasmas*, vol. 9, pp. 949–957, Feb. 2002.

[55] L. M. Cabaln and J. J. Laserna, "Experimental determination of laser induced breakdown thresholds of metals under nanosecond Q-switched laser operation," *Spectrochimica Acta*, vol. 53, pp. 723–730, May 1998.

[56] J. Reiser, M. Rieth, A. Mslang, B. Dafferner, A. Hoffmann, X. Yi, and D. E. J. Armstrong, "Tungsten foil laminate for structural divertor applications Tensile test properties of tungsten foil," *Journal of Nuclear Materials*, vol. 434, pp. 357–366, Mar. 2013.

[57] I. Utke, S. Moshkalev, and P. Russell, *Nanofabrication Using Focused Ion and Electron Beams: Principles and Applications*. Oxford University Press, USA, May 2012.

[58] M. E. Shaheen, J. E. Gagnon, and B. J. Fryer, "Laser ablation of iron: A comparison between femtosecond and picosecond laser pulses," *Journal of Applied Physics*, vol. 114, p. 083110, Aug. 2013.

B

Electron irradiation effects on strength and ductility of polymer foils studied by femtosecond laser processed micro-tensile specimens

Manuel J. Pfeifenberger [1,*], Gabor Milassin [2], Anton Hohenwarter [3], Barbara Putz [1], Christopher O. A. Semprimoschnig [2] and Reinhard Pippan [1]

[1] Erich Schmid Institute of Materials Science, Austrian Academy of Sciences, 8700 Leoben, Austria
[2] ESA - ESTEC (TEC-QEE), Keplerlaan 1, 2201 AZ Noordwijk, The Netherlands
[3] Department of Materials Science, Chair of Materials Physics, University of Leoben, 8700 Leoben, Austria

Abstract

The influence of irradiation on mechanical properties of polymer foils used in spacecraft applications has widely been studied via macroscopic tensile samples. An increase in the local resolution of this investigation can be achieved by reducing the sample's dimensions. A femtosecond laser enables a fast fabrication of micro-samples with dimensions from tens of μm to the mm range, with ideally no influence on the material. Tensile experiments using such micro-tensile samples were conducted on FEP, Upilex-S and PET foils. The influence of the laser processing on the polymer foils was evaluated. Additionally an investigation of degradation due to electron irradiation was performed. Furthermore an outlook to extend this technique to depth-resolved measurements by preparing samples from locally thinned foils is presented. The study demonstrates the feasibility of femtosecond laser processing for rapid fabrication of micro-samples, enabling insights into the effect of electron irradiation on local mechanical properties of polymers.

B.1 Introduction

Polymer foils used in spacecrafts, e.g., as thermal control foils, are usually exposed to multiple types of radiation and severe thermal cyclic loading [1–3]. The influence of irradiation on the mechanical properties of polymer foil materials has already been studied widely, mainly via testing macroscopic tensile specimens [1, 4–10]. Existing experiments on the macro scale cannot, however, resolve local variations in mechanical properties, e.g., caused by degradation due to inhomogeneous irradiation conditions. The mapping of such variations requires a significant reduction of the sample dimensions, compared to the dimensions specified in ASTM D882 [11]. Very small specimens can additionally contribute to an efficient investigation of materials which are limited in their availability or exclusive in their kind, e.g., polymer foils retrieved from space missions.

A femtosecond (fs) laser enables a fast and reproducible way for the fabrication of such micro-samples. This technique offers optimal properties for material processing on a scale from tens of micrometers up to a few millimeters. Most importantly, using a fs-laser for processing impedes melting of the specimen material during the ablation due to ideally no thermal diffusion into the material. This allows precise and reproducible fabrication of structures on the micro-scale [12]. An increase in processing precision, compared to lasers with a longer pulse duration, has been found for various classes of materials including polymers, semiconductors and ceramics [13, 14]. The negligible material modification during fabrication of the sample is a significant advantage compared to other techniques for small scale processing like micro electric discharge machining [15] or laser processing using lasers with pulse durations above the ultra-short pulse regime (i.e., >10 ps) [16]. However, the high material removal rate of the fs-laser competes with the rate of the aforementioned techniques and outperforms other methods such as the focused ion beam (FIB) or Plasma FIB by orders of magnitude [17]. The presented features make the fs-laser particularly interesting for the micro-processing of polymers.

The processing of micro tensile samples by means of a fs-laser has rarely been studied. Works by Slaughter et al. [18], Severin et al. [19] and Magagnosc et al. [20] already showed the feasibility of this method for micro tensile sample fabrication of different materials. A proper investigation of the laser processing influence on the mechanical properties of polymers is missing, though. Hence, in this study, three types of polymers with strongly different mechanical properties have been investigated and the results are discussed in comparison with macroscopic results from literature.

The polymer foils were exposed to electron irradiation with typical dose levels seen by spacecraft in the low earth orbit to asses the capability of the micro-tensile experiments to study the influence on the material. Other influencing factors of the space environment like, thermal cycling, high vacuum, electromagnetic irradiation

or further types of charged particle irradiation [9, 21] have not been investigated in this work. The influence of mixed irradiation is discussed elsewhere [1–3, 5, 6, 8].

Micro tensile specimens allow to evaluate the mechanical properties on a scale of a few hundred micrometer, hence, this study provides a technique, which can yield insights into the local irradiation damage of polymer foils. Additionally, the determination of damage gradients across the thickness of polymer foils can be of interest. It is particularly interesting to investigate the depth of embrittlement zones due to (space) irradiation. The fs-laser processing combined with the capability of precise positioning allows to locally slice the foils into thinner sections. This depicts a promising technique to enable the acquisition of depth-resolved mechanical data.

This study is structured as follows: The first part deals with the experimental details of the work. In Section B.3.1 results on the influence of the laser processing on the polymer foils are given and discussed. The results of the micro-sample tensile experiments are shown in Section B.3.2. Section B.3.3 contains the investigation of the influence of electron irradiation doses present in space environment conditions, on the mechanical properties of the foils. Details on the effect of different ambient atmospheric conditions during the laser processing on the materials are discussed in Section B.3.4. Finally, an outlook on the fabrication of tensile samples with varying thickness, via local thinning of the foils, is presented.

B.2 Experimental

In this study a recently developed system, which combines a fs-laser with a FIB and a scanning electron microscope (SEM) was used (based on the Auriga Laser platform—Zeiss, Oberkochen, Germany). Details of the system can be found in a previous study [22]. The integrated fs-laser is a Origami 10 XP (Onefive GmbH, Regensdorf, Switzerland). The fs-laser has a pulse duration of about 500 fs, two available wavelengths of 1030 and 515 nm and a maximum pulse repetition rate of 1 MHz. For the sample processing the wavelength of $\lambda = 515$ nm, which allows a maximum average output power of about 2 W, is used. Two lenses placed prior to the scan unit act as beam expander. Their distance determines the focal height in the processing chamber. The beam is guided by a galvanometer scan unit (intelliscan III 10, SCANLAB AG, Puchheim, Germany). The objective lens allows an optimal focal diameter at the sample surface of approximately 25 μm. SEM imaging is used to evaluate the quality of the laser processed samples.

B.2.1 Materials

Three different polymer foil materials were investigated in this work:

- Polyimide Upilex-S VDA (25.4 μm-thickness) from UBE

- PET (Polyethylene terephthalate) (127 μm) from Sheldahl
- FEP (Fluorinated ethylene propylene) VDA (127 μm) from Sheldahl

The Upilex-S and FEP foil are coated with a vapor deposited aluminium (VDA) thinfilm (with 100 nm-thickness) on one side. The PET foil is not coated.

The three types of polymer foil materials exhibit distinctively different tensile properties, ranging from high ultimate strength to high ultimate strain, therefore, this materials are ideally suited to assess experiments with fs-laser fabricated micro-tensile specimens. Furthermore, Upilex-S VDA and FEP VDA foils are commonly used in multilayer insulation of spacecraft [21, 23], hence, an evaluation of their resistivity against electron irradiation is of essential interest.

Electron Irradiation Procedure

The electron irradiation doses of the outer layer of thermal blankets of the Hubble Space Telescope in the low Earth orbit roughly range from 100 kGy to about 1 MGy for the shortest servicing missions up to the defined end-of-life duration respectively [2, 24]. The electron irradiation doses investigated in this study cover this dose range.

The irradiation was performed in a van de Graaff-type electron accelerator producing an electron beam with 1 MeV and a dose rate of 146 Gy/s. The 2 centimeter thick aluminium exposure table was water-cooled and a nitrogen flushed frame was placed above the samples to keep them close to room temperature and to inhibit oxidation. For the dosimetry measurements radiochromic Nylon thin foil dosimeters were used. Coated foils were irradiated from the non-coated side. Material samples were grouped in stacks of different heights on the exposure table, 12 foils for Upilex-S VDA, 4 foils for FEP VDA and 4 foils for PET. Due to the high electron energies, the small total stack thickness and the low density of the polymers, the dose rate was assumed to be constant across the thickness during the whole exposure process. In order to reach different irradiation dose levels, the exposure was interrupted regularly to remove foils from the stack. Hence, for example, to achieve a total irradiation dose of 250 kGy the foils were removed after 28.5 minutes from the exposure setup. For each material this procedure yielded samples with certain total electron irradiation doses (listed in Table B.1). The FEP VDA foils became too brittle to handle for irradiation doses above 250 kGy, hence, only two irradiation dose levels were investigated for this material.

Irradiation dose [kGy]	0	250	500	750	1000
Upilex-S VDA	○	○	○		○
PET	○	○	○	○	
FEP VDA	○	○			

Table B.1 The investigated electron irradiation doses for each of the 3 different polymer foil materials.

B.2.2 Methods

Laser Processing

The focal plane was determined by selecting the ablation spot with minimum diameter via varying the distance of the beam expander lenses. The samples were placed in the middle of the scan field to ensure a normal incidence of the laser beam onto the foil.

In Table B.2 the laser processing parameters used for the fabrication of the tested specimens are listed. The laser processing parameters mainly responsible for the quality of the cut are the pulse repetition rate and the fluence. In Section B.3.1 the influence of the laser pulse repetition rate on the sample quality is discussed in more detail. The fluence is the energy density at the focal spot and directly proportional to the maximum average power. For the investigated types of polymers (Polyimide, FEP and PET) multi-pulse fluence ablation thresholds of ultra-short pulsed laser were reported to be in the range of about 0.3–0.5 J/cm^2 [14, 25]. The fluence values given in Table B.2, were selected close to the ablation threshold to ensure a high quality cutting surface, however, still being high enough to enable an adequate removal rate for a fast sample processing. The value for the Upilex-S VDA material is lower due to its smaller thickness.

	Upilex-S VDA	FEP VDA	PET
Fluence [J/cm^2]	0.65	1.18	1.18
Pulse rep. rate [kHz]	1	1	1
Scan speed [mm/s]	2	2	2
Scan repetitions [−]	15	40	40
Processing time [s]	≈ 380	≈ 1000	≈ 1000
Taper angle [°]	15.1 ± 0.4	9.5 ± 0.8	8.0 ± 0.5

Table B.2 Laser parameters used for the processing of the tested tensile samples in different foil materials. The respective total processing time and the resulting taper angle are given.

The scan repetitions define how often each laser pattern, shown in Fig. B.1b, is successively scanned. This adds up to the total processing times listed in the table for the respective parameters of each sample material. The scanning strategy plays an important role, especially regarding the redeposit of ablated material. Further details regarding the scanning strategy can be found in [22]. If not stated otherwise, the fs-laser processing was conducted under a vacuum pressure of ca. 7×10^{-3} mbar.

Prior to the laser processing a piece of the foil with a size of about 6×6 mm, cut using scissors, was fixed in a clamp, which could be afterwards mounted in the tensile testing device. The foils were fixed with the VDA side facing upwards. This is sketched in Fig. B.1a. The image also schematically indicates the laser beam incidence direction. Subsequently, the tensile geometry was cut in a two-step process as shown in Fig. B.1b. First a rectangular shape and second the dog bone shape was fabricated. The scan patterns consist of single lines successively shifted by a distance of 10 μm (see detail in Fig. B.1b). The tensile samples are placed in a distance of 1.4 mm to each other to ensure enough space for the testing gripper. This enables to test a maximum of four samples on each piece of foil, fixed in a clamp (as shown in Fig. B.1c). The final cross-section geometry of the samples shows a trapezoidal shape due to a certain taper angle resulting from the laser processing. The resulting mean values of the taper angles for the respective processing parameters of each sample material are listed in Table B.2. This taper can not be compensated in the used fabrication setup, however, it shows good reproducibility when using the same processing parameters. The trapezoidal shape of the cross-section was taken into account for the stress evaluation of the tensile experiments.

Setup of Tensile Experiments

The uni-axial tensile experiments were performed on a Kammrath & Weiss fibre tensile module [26]. This device enables to measure forces up to about 2 N with a resolution of approximately 10 μN. The displacement is registered with an accuracy of about 30 nm. The experiments are recorded using a camera connected to a stereo microscope, taking images every five seconds. Using a moveable stage the sample can be properly aligned with the gripper. The gripper was cut out of a 100 μm-thick tungsten foil, resembling the negative shape of the tensile sample head, with the same fs-laser system. All experiments were performed displacement controlled and the force was recorded. The testing speed was 1 μm/s, resulting in an initial strain rate of about 0.3%/s. Only the non-irradiated FEP VDA foils, due to their very high maximal strain values, were tested with 2 μm/s (strain rate 0.6%/s) to keep the test duration limited. This low testing speed values enable the capturing of enough pictures throughout the loading process to perform a continuous displacement correction of the data. Each sample was elongated until failure. The experiments were conducted at room temperature (22 °C) under atmospheric conditions.

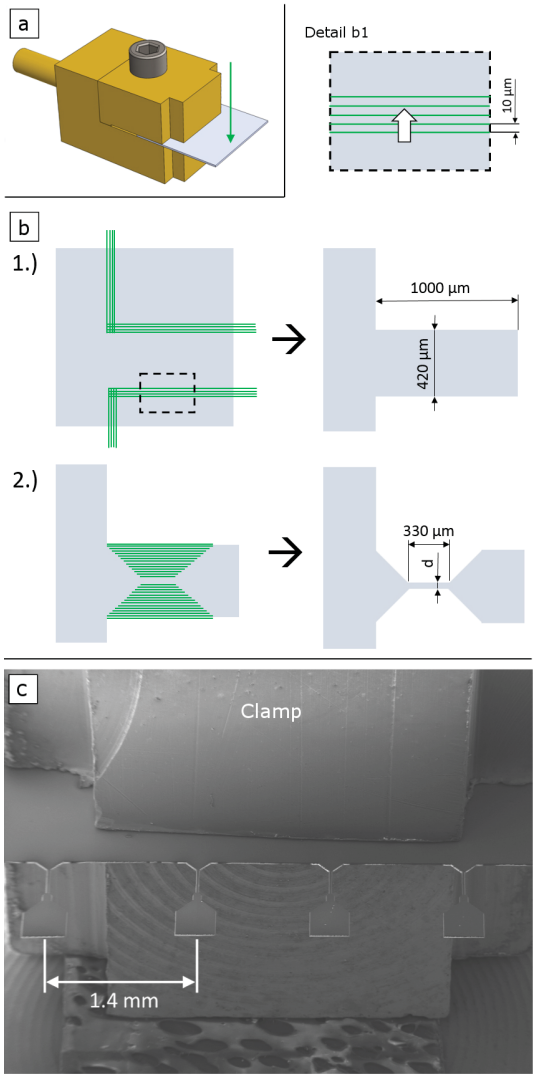

Figure B.1 (**a**) 3D sketch of a foil fixed in a clamp with the VDA film on top. The arrow indicates the incidence direction of the laser beam. (**b**) Outline of the two step cutting process from the view of the laser incidence direction. First a rectangular shape with the intended width of the tensile head is cut. In the second step the dog bone shape is processed. Relevant dimensions of the specimen are given. The width d of the gauge section was about 100 μm for the FEP VDA and about 25 μm for the Upilex-S VDA foils. Detail (b1) displays the magnification of the dashed rectangle in step 1. Each laser scan line is shifted 10 μm in the direction of the broad arrow. (**c**) SEM image showing a set of four samples cut in a Upilex-S VDA foil, fixed in the clamp for the following tensile experiments.

B.3 Results and Discussion

B.3.1 Influence of fs-Laser Processing

Femtosecond laser processing is a fast and versatile method for the fabrication of micro-samples, nevertheless, especially in the case of polymers the influence of heat and effects due to air ionization (see Section B.3.4) need to be considered. Specifically, in the case of polymers the repetition rate needs to be carefully chosen. The excessive energy of each laser pulse, which is not used to ablate material generates a small amount of heat [27]. If the pulse repetition rate is high, the accumulation of the heat can lead to a local melting of the processed materials [28]. Especially for materials with a low heat conductivity this is critical in terms of achieving a high quality of the cut.

To evaluate the heat accumulation effect on the sample quality an experiment, varying the time of energy input, was performed on the three investigated materials. For this, five parallel lines with a length of 600 μm placed at a distance of 10 μm were cut into the foil, resulting in a rectangular cut. This is sketched in Fig. B.2. The fluence was chosen to be 1.18 J/cm^2, the scan speed 2 mm/s and the laser pulse repetition rate was varied: 50, 25, 10, 5, 1 kHz. To keep the total energy input constant the scan repetitions were adapted accordingly: 1, 2, 5, 10, 50 repetitions. Hence, the amount of laser pulses per cut are kept constant, but the processing duration varies from 1.5 s to 75 s. SEM details of the upper and lower edge of this rectangular cuts, as indicated in Fig. B.2, are shown in Fig. B.3 for Upilex-S VDA, in Fig. B.4 for PET and in Fig. B.5 for FEP VDA.

The 25 μm-thick Upilex-S VDA foils were cut through the entire thickness for all parameter combinations. For pulse repetition rates of 50 and 25 kHz, the specimens exhibited a massive damage up to a distance of 200 μm around the processed area. For the pulse repetition rate of 10 kHz (Fig. B.3c) still a small part of molten material was observable. For the cuts done with 5 kHz and 1 kHz clean cutting surfaces were obtained.

Pronounced melting was also found for the PET foils up to 150 μm away from the cutting edge for the highest pulse repetition rates of 50 and 25 kHz. For this material a molten burr also appeared for 5 kHz. A pulse repetition rate of 1 kHz again showed minimized damage. All pulse repetition rates allowed a cut through the entire 127 μm-thick PET foils.

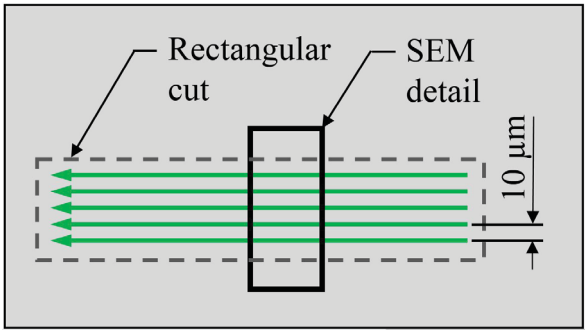

Figure B.2 Scan pattern for the laser parameter tests. 5 parallel lines, each shifted for 10 μm, were cut into the foil and yielded a rectangular cut as indicated by the dashed line. The position of the SEM details shown in Figures B.3–B.5 is indicated.

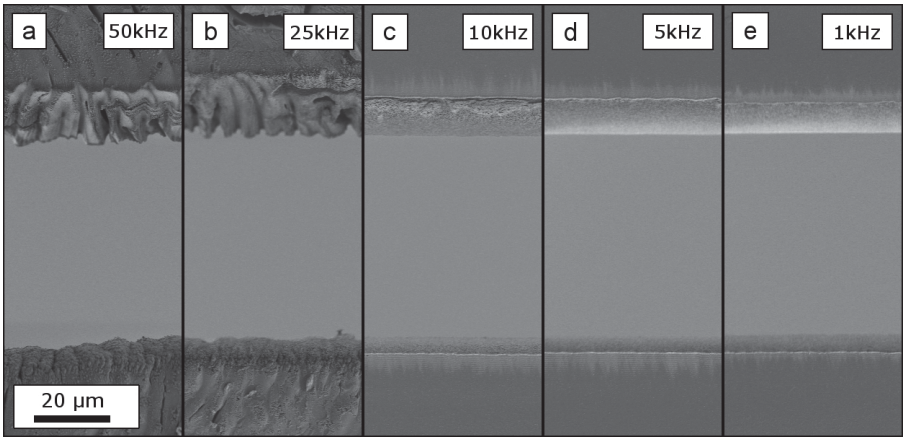

Figure B.3 SEM details, as indicated in Fig. B.2, show the edges above and below the central rectangular cut in a 25.4 μm-thick Upilex-S VDA foil. The cuts were processed with a constant total energy input, hence, decreasing pulse repetition rates whilst increasing the number of scan repetitions (corresponding to increasing machining times). (**a**,**b**) show massive damage, cracks and molten structures. In (**c**) local molten areas are observable on the upper edge. In (**d**,**e**) both edges exhibit clean cutting surfaces. The scale bar indicated in (**a**) applies to all figures.

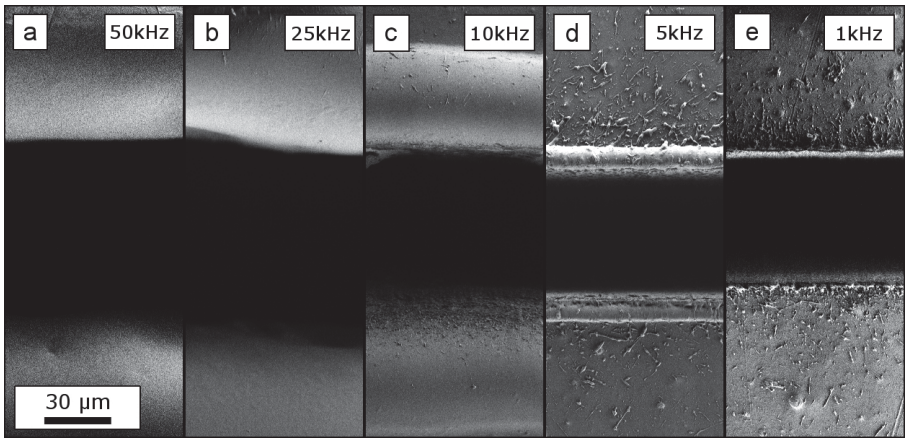

Figure B.4 Upper and lower edge of rectangle cuts in a 127 μm-thick PET foil. The cuts were processed with a constant total energy input, hence, decreasing pulse repetition rates ((a) 50 kHz; (b) 25 kHz; (c) 10 kHz; (d) 5 kHz; (e) 1 kHz;) whilst increasing the number of scan repetitions (corresponding to increasing machining times). The foil thickness is cut through for all tested parameter combinations. Massive melting is found for repetition rates larger than 5 kHz. Note the larger scale bar, compared to Figures B.3 and B.5. The scale bar indicated in (**a**) applies to all figures.

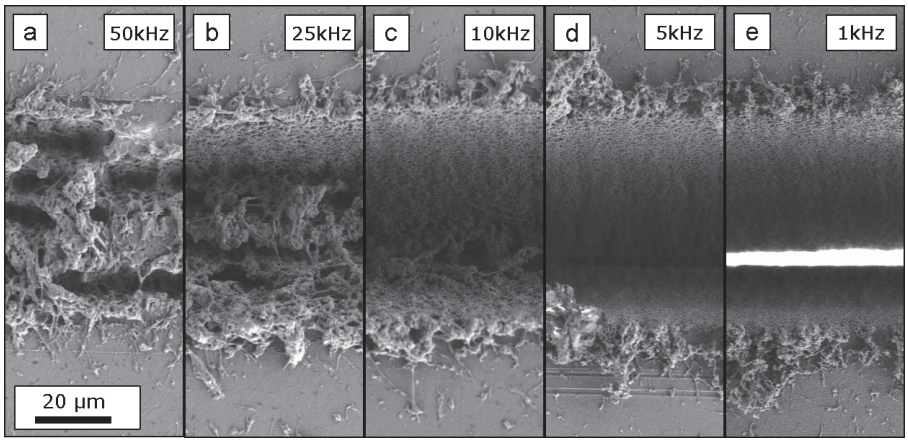

Figure B.5 Upper and lower edge of rectangle cuts in a 127 μm-thick FEP VDA foil. The cuts were processed with a constant total energy input, hence, decreasing pulse repetition rates ((a) 50 kHz; (b) 25 kHz; (c) 10 kHz; (d) 5 kHz; (e) 1 kHz;) whilst increasing the number of scan repetitions (corresponding to increasing machining times). The foil thickness is cut through only for 50 kHz and 50 scan repetitions as multiple scan repetitions enable more efficient material removal, compared to few scan repetitions and high pulse repetition rates. The scale bar indicated in (**a**) applies to all figures.

The damage of the FEP VDA foils showed less signs of damage due to melting, but an increase in debris deposition next to the processed structure compared to Upilex-S VDA and PET foils. Additionally, another critical issue occurred when compared to Upilex-S VDA and PET films. The use of high pulse repetition rates and respective small numbers of scan repetitions yields a small material removal rate. Therefore, a cut through the 127 μm-thick FEP VDA foil, was only achieved for 50 scan repetitions using a pulse repetition rate of 1 kHz (see Fig. B.5e). The good heat resistance of FEP experienced in the fs-laser cutting experiments agrees with the results of thermally cycled FEP, which did not exhibit significant changes in its tensile properties [7].

According to the results of these experiments on the variation of the pulse repetition rate, a rate of 1 kHz was used for the fabrication of all tensile test specimens. The scan repetitions were set to values, which ensure a through thickness cut (see Table B.2).

B.3.2 Tensile Experiments

The tensile properties of the three investigated non-irradiated materials show large differences in both, the maximum strength and the maximum elongation (see Fig. B.6). While Upilex-S VDA shows a very high ultimate tensile strength (UTS), the FEP VDA foils exhibit low UTS and a considerably maximum tensile strain. The values for the PET samples lie within this range and exhibit additionally a distinctive orientation dependency. The directions of the orientation are commonly referred to as machine direction (MD) and transverse direction (TD) related to the fabrication procedure of the foil [29]. This orientation dependence has not been found for the Upilex-S VDA and FEP VDA foils. The resulting curves of Upilex-S VDA and PET are comparable to results of macroscopic experiments (according to ASTM D 882) [11, 23].

The stress-strain curves measured for the FEP VDA samples exhibit a yield stress and a ultimate tensile strain in good agreement with macroscopic results [2]. However, the UTS from the micro-tests is significantly lower than the macroscopic value. The FEP VDA micro-samples do not show an increase of strength at elongation values of about 200% as reported for non-irradiated macroscopic specimens [2]. This suggests an alteration of the mechanisms responsible for the typical strain hardening of this material, due to the fs-laser.

B.3.3 Influence of Electron Beam Irradiation

Upilex-S VDA

The resulting tensile curves of Upilex-S VDA samples are shown in Fig. B.7. Foils irradiated with a dose of 0 (four samples), 250 (3), 500 (4) and 1000 (3) kGy were

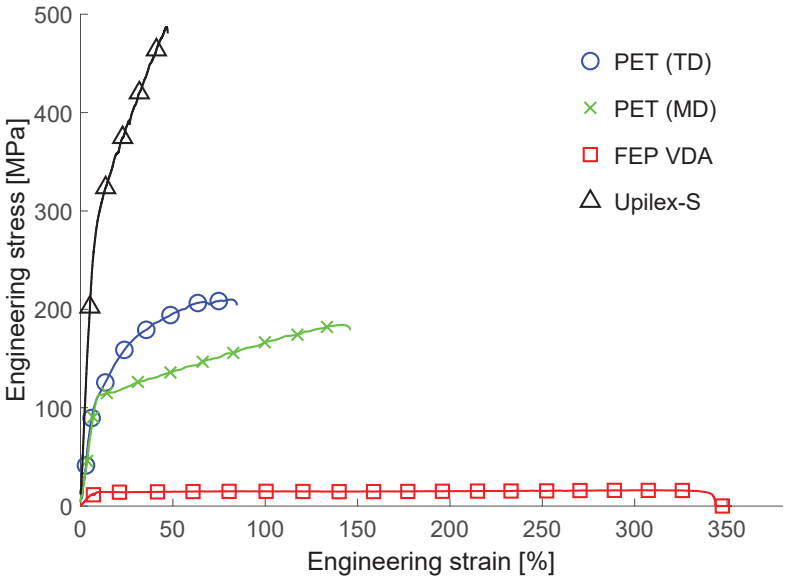

Figure B.6 Results of the tensile experiments on non-irradiated FEP VDA, PET and Upilex-S VDA micro-samples. The materials show a large variation in their tensile behaviour. Additionally, the PET foils exhibit a distinct orientation dependency.

tested. No necking is observed during elongation. The experiments do not show a significant influence of the electron irradiation on the tensile properties. This high resistivity of Upilex against degradation by means of electron irradiation has already been shown [4, 8, 30]. No significant differences were found for the mechanical properties regarding the orientation of the samples (MD, TD), which has also been found in [4]. The results yield a very good agreement with the mechanical properties found in [23] (UTS of 520 MPa and maximum strain of 42%).

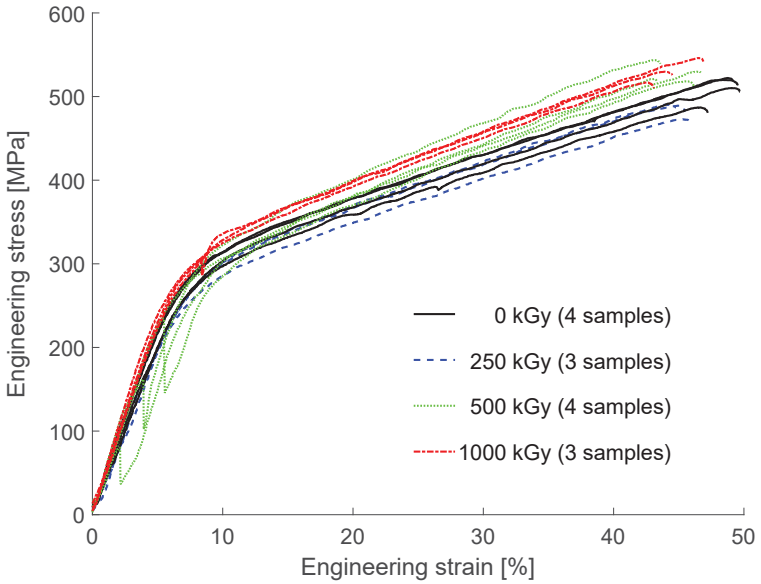

Figure B.7 Results of the tensile experiments of the Upilex-S VDA foils exposed to irradiation doses of 0 kGy, 250 kGy, 500 kGy and 1000 kGy. The number of tested samples for each irradiation dose is indicated. There is no significant influence of the irradiation dose up to 1000 kGy. The deviation from a straight line in the linear elastic part shown by three curves, stems from a small rotation of the sample head due to a non-proper alignment with the gripper at the beginning of the tensile experiment.

PET

The stress-strain curves of the tensile experiments on the PET foils are shown in Figure B.8. The PET foils exhibited a distinct dependence on the foil orientation (TD and MD). Both directions had a yield stress of about 105 MPa, which agrees well with the values found in [31]. The UTS of the MD orientation is lower than that of the TD. However, a stronger increase of stress after the yield point is observed in the presented micro-tests compared to literature. This can be most likely linked to the higher strain rate used in the present work compared to the study of Poluektov et al. [31].

Regarding the electron irradiation samples with a dose of 0 kGy (5 samples TD, 2 MD), 250 kGy (4 MD), 500 kGy (3 MD) and 750 kGy (2 TD) were tested. Electron irradiation lead to a slight reduction of the yield strength. A significant decline in the maximal tensile strain and stress was found for both orientations. This is in contrast to the results in [32], which suggest for irradiation doses of 250 kGy and 500 kGy relatively constant values compared to non-irradiated PET samples.

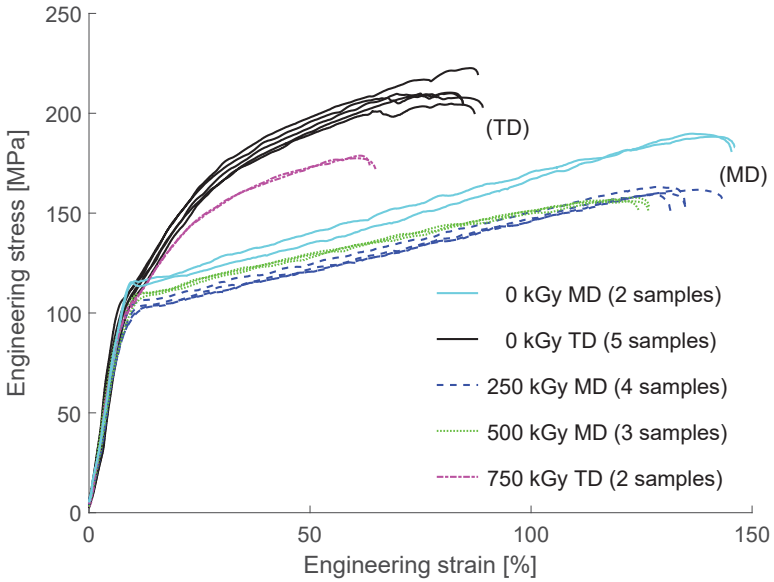

Figure B.8 Results of the tensile experiments of the PET foils exposed to different irradiation doses. The number of tested samples for each irradiation dose is indicated. A reduction of the UTS was found for both, the machine and the transverse direction for all irradiation doses. For a dose of 750 kGy the maximum strain exhibited a significant reduction for the TD direction, respectively for the MD direction and 500 kGy. Only a slight reduction was found for the MD direction when irradiated with 250 kGy.

FEP VDA

In contrast to the Upilex-S VDA foils the FEP VDA foils are strongly affected by the electron irradiation. Fig. B.9 shows the results of tensile tests on 10 non-irradiated and 10 irradiated samples. Contrary to PET and Upilex-S VDA, the FEP VDA samples exhibit a load decrease after yielding, related to necking. In the case of the pristine samples the ultimate tensile strain yielded a mean value of 346% ± 11%, which agrees well with the value of 356% ± 8% given in [2]. The irradiation dose of 250 kGy leads to a reduction of this mean value to 57% ± 27%. No dependence of the resulting curves on the MD and TD direction was observed for the FEP VDA specimens. Further the yield strength of 14.2 ±0.2 MPa reported in [2] is in excellent agreement with the results in Fig. B.9. For the irradiated material an increase in the variation of the yield strength is observed. This increase is observed between the different sets of samples (four samples mounted on one clamp, see Section B.2.2), while the scatter between the samples on a single mount stays in the same range as the value of the non irradiated specimens. As the positions of each sample set are located in a range of a few centimeters, this increased scatter in the yield strength

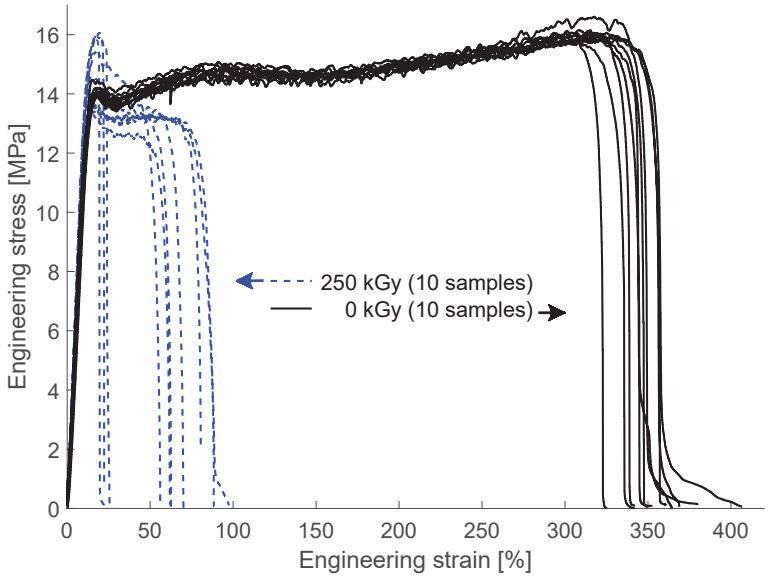

Figure B.9 Results of the tensile experiments of the FEP VDA foils exposed to electron irradiation doses of 0 kGy and 250 kGy. For each irradiation dose 10 samples have been tested. The irradiated samples show a reduction of the ultimate tensile strain to about 7–25% of the value of non-irradiated samples. Furthermore, the irradiated samples exhibit an increased scatter of the yield strength.

possibly results from a local variation in the degradation due to a lateral variation of the electron irradiation dose.

B.3.4 Influence of fs-Laser Processing Atmosphere

The fs-laser processing atmosphere can play a critical role. Using atmospheric conditions the high energy density in the focal spot can lead to an ionization of the surrounding air [33]. In a study on PTFE [34] it has been shown that exceeding the threshold for ionization leads to a reduction of the ablation efficiency. Furthermore, the quality of processed surfaces decreases and an increase in debris deposition was found. To investigate the influence of atmospheric conditions during processing on the mechanical properties, tensile samples were cut with increasing fluence values of 1.18, 1.31, 1.96 and 2.62 J/cm^2 under both, vacuum and ambient atmosphere. All other parameters were kept the same as listed in Table B.2.

For the Upilex-S VDA and PET micro-samples, processed under ambient pressure conditions, no change in tensile properties for increasing fluence values was found (see Appendix B.5). The FEP VDA samples, however, exhibited a significant reduction of the ultimate strain as shown in Fig. B.10. The curve for the sample processed with

1.18 J/cm^2 under vacuum showed a maximum strain of about 350%. Increasing the fluence value to 2.62 J/cm^2 reduces the ultimate strain also for vacuum conditions. This can be linked to a reduced quality of the cut and the occurrence of pores, which act as initial sites of failure. Fabricating the specimens under ambient air pressure, however, yielded a more pronounced reduction of the ultimate tensile strain for all fluence values. Additionally, the yield strength as well as the UTS is lowered for the samples processed under atmospheric conditions. Such an influence of the exposure environment on the extent of degradation of FEP has also been found for other types of irradiation and is linked to a higher yield of scission when irradiated in air [21].

An effect of using atmospheric processing conditions, as well as increasing fluence values was not found for irradiated FEP VDA samples. In this case, the influence of the electron irradiation dominates the decrease of the UTS and the maximum strain.

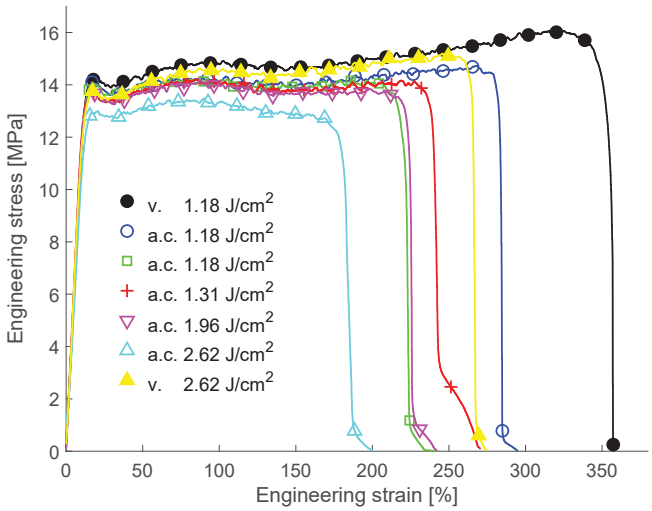

Figure B.10 Influence of the ambient processing conditions on the tensile experiments of FEP VDA. For each condition, except the standard processing condition (vacuum (v.) and 1.18 J/cm^2), one sample was tested. Processing under atmospheric conditions (a.c.) shows a somewhat smaller UTS and a significant reduction of the ultimate tensile strain compared to vacuum conditions. This effect increases with increasing fluence values.

B.4 Outlook—Local Thinning of the Polymer Foil

Due to the very high energy electron beam used in this study and the small sample thickness, a constant electron irradiation damage across the thickness of the foils can be assumed. This will not be the case for foils used in space missions, hence,

these samples may exhibit a gradient in irradiation damage across the foil thickness. A technique to evaluate the extent of this gradient as well as its influence on the mechanical properties has not been established yet. Due to the high material removal rate combined with the high precision, the fs-laser system allows to locally thin such foil samples. Taking into account the accuracy of the sample positioning, the thickness of the sample can be gradually reduced with a step-size of about 20 μm.

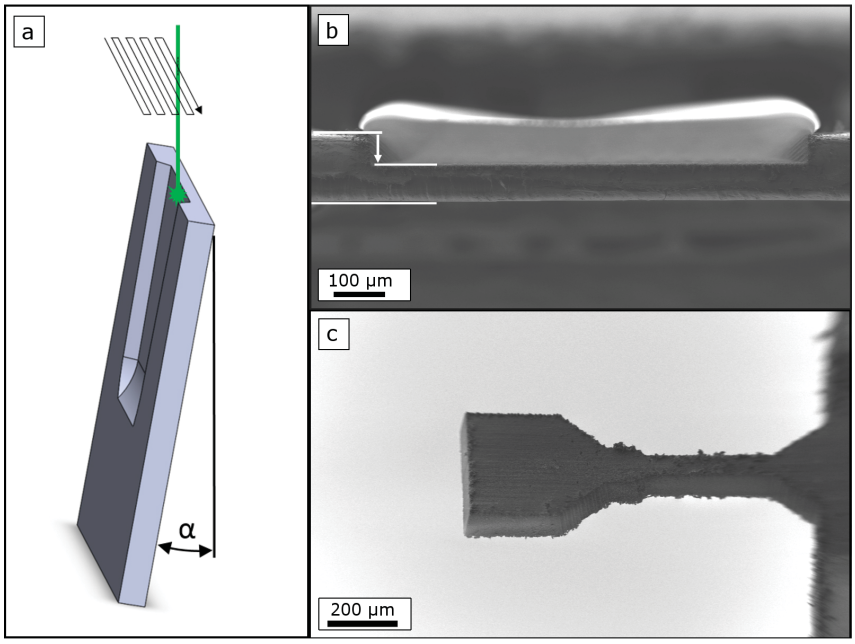

Figure B.11 Fs-laser processing allows a local reduction of the foil thickness. (**a**) The thinning needs to be performed under the resulting, parameter dependent taper angle α. (**b**) FEP VDA foil thin section with a thickness of ca. 80 μm. (**c**) Tensile specimen cut into a thinned section.

The necessary preparation geometry is sketched in Fig. B.11a. The foil surface is oriented under an angle, which corresponds to the resulting taper angle, relative to the incidence direction of the laser. This arrangement allows to fabricate a trench with a sidewall parallel to the opposite foil surface. For this the laser beam is scanned in a meander-like path towards the intended depth in multiple repetitions. As the achievable resolution is about 20 μm, linked to the positioning accuracy and the spot size, this approach is of interest for a foil thickness starting around 100 μm. An example of a locally thinned FEP VDA foil with a thickness of 80 μm is shown in Fig. B.11b, viewed from the laser incidence direction. To cut this trench the foil was positioned under an angle of about $\alpha = 9°$. This corresponds to the taper angle resulting when using the parameters for FEP VDA given in Table B.2. An example

of a tensile specimen cut into the locally thinned area is shown in Fig. B.11c. The tensile sample processing followed the fabrication route outlined in Section B.2.2.

B.5 Conclusions

Femtosecond laser processing of polymer micro-samples was demonstrated for Upilex-S VDA, FEP VDA and PET foils. The structural quality of the samples is strongly influenced by the femtosecond laser pulse repetition rate due to heat accumulation effects. A repetition rate of 1 kHz yielded a minimal influenced zone, while ensuring a sufficient material removal rate.

The evaluation of tensile properties by means of the femtosecond laser processed micro-samples shows a good agreement with macroscopic data found in literature. No degradation of the samples due to laser processing was found for the PET and Upilex-S VDA specimens. However, the FEP VDA samples exhibited a sensitivity of the tensile properties on the ambient atmospheric conditions as well as the fluence of the fs-laser. Electron irradiation up to 1000 kGy did not influence the tensile properties of Upilex-S VDA foils. PET foils revealed a distinct orientation dependence and showed a minor degradation due electron beam irradiation, observable for all investigated doses from 250 to 750 kGy. FEP VDA foils exhibited a pronounced degradation already for an irradiation dose of 250 kGy. Besides a lower ultimate tensile strength, the ultimate tensile strain was reduced by a factor of about 6.

The study showed that femtosecond laser processing allows a fast and reproducible fabrication of polymer micro-samples with sizes of up to multiple hundreds of micrometers, therefore, enabling a high resolution for the investigation of local mechanical properties of polymer foils.

Acknowledgments

The authors want to thank Alexander Jelinek for the thorough assistance in sample processing.

Appendix B.A

The influence of the atmospheric conditions during laser processing on the tensile properties was found to be significant for the FEP VDA foils, exhibiting a distinct decrease in the ultimate tensile strain (see Section B.3.4). For non-irradiated Upilex VDA foils (Fig. B.A.1) and non-irradiated PET foils (Fig. B.A.2) no such effect was found. For both materials, even for the highest fluence values, the ultimate tensile stress and the ultimate tensile strain are within the scatter observed for samples processed under vacuum conditions.

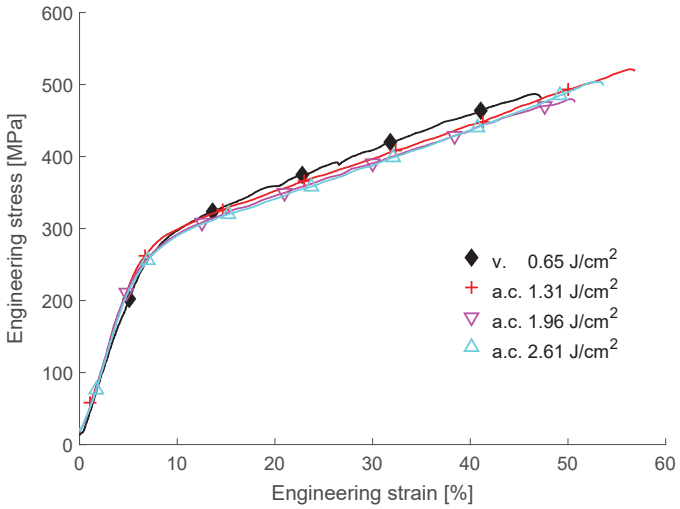

Figure B.A.1 Influence of the ambient processing conditions on the tensile experiments of Upilex VDA foils. For atmospheric conditions (a.c.) and each fluence value one sample was tested. Comparing samples processed with increasing fluence under a.c. with samples processed under vacuum conditions (v.) does not reveal any influence. The scatter of the data lies within the scatter observed in Fig. B.7.

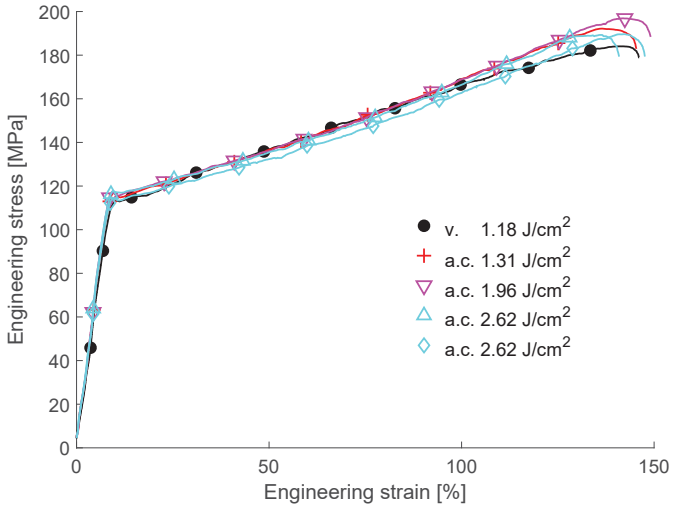

Figure B.A.2 Influence of the ambient processing conditions on the tensile experiments of PET foils in MD. For atmospheric conditions (a.c.) and fluence value of 1.31 and 1.96 J/cm^2 one sample was tested. For the fluence of 2.62 J/cm^2 two curves are given. Comparing samples processed with increasing fluence under a.c. with samples processed under vacuum conditions (v.) does not reveal any influence. The scatter of the data lies within the scatter observed in Fig. B.8.

Bibliography to publication B

[1] J. A. Townsend, P. A. Hansen, J. A. Dever, K. K. de Groh, B. A. Banks, L. Wang, and C. He, "Hubble Space Telescope Metallized Teflon FEP thermal Control Materials: On-Orbit Degradation and Post-Retrieval Analysis," *High Perform. Polym.*, vol. 11, pp. 81–99, mar 1999.

[2] J. A. Townsend, C. E. Powers, M. J. Viens, M. T. Ayres-Treusdell, and B. F. Munoz, "Degradation of Teflon® FEP Following Charged Particle Radiation and Rapid Thermal Cycling," in *20th Space Simulation Conference*, vol. NASA/CP-1999-208598, jan 1998.

[3] C. O. A. Semprimoschnig, S. Heltzel, A. Polsak, and M. Van Eesbeek, "Space Environmental Testing of Thermal Control Foils at Extreme Temperatures," *High Perform. Polym.*, vol. 16, pp. 207–220, jun 2004.

[4] T. Sasuga, N. Hayakawa, K. Yoshida, and M. Hagiwara, "Degradation in tensile properties of aromatic polymers by electron beam irradiation," *Polymer*, vol. 26, pp. 1039–1045, jul 1985.

[5] J. A. Dever, K. K. de Groh, B. A. Banks, and J. A. Townsend, "Effects of Radiation and Thermal Cycling on Teflon FEP," *High Perform. Polym.*, vol. 11, pp. 123–140, mar 1999.

[6] M. Moser, C. Ranzenberger, and S. Duzellier, "Space Environmental Testing of Novel Candidate Materials for Multilayer Insulation," *Journal of Spacecraft and Rockets*, vol. 53, no. 6, pp. 1134–1140, 2016.

[7] M. Moser, C. O. A. Semprimoschnig, M. Van Eesbeek, and R. Pippan, "Comparison of results from post-flight investigations on FEP retrieved from the Hubble Space Telescope solar arrays and LDEF," *Proceedings of the European Conference on Spacecraft Structures, (Special Publication) ESA SP*, vol. 581, p. 95, jan 2005.

[8] H. Shimamura and I. Yamagata, "Degradation of Mechanical Properties of Polyimide Film Exposed to Space Environment," *Journal of Spacecraft and Rockets*, vol. 46, no. 1, pp. 15–21, 2009.

[9] J. Chen, N. Ding, Z. Li, and W. Wang, "Organic polymer materials in the space environment," *Progress in Aerospace Sciences*, vol. 83, pp. 37–56, may 2016.

[10] J. A. Dever, S. K. Miller, E. A. Sechkar, and T. N. Wittberg, "Space Environment Exposure of Polymer Films on the Materials International Space Station Experiment: Results from MISSE 1 and MISSE 2," *High Perform. Polym.*, vol. 20, pp. 371–387, aug 2008.

[11] ASTM, "ASTM D882-18, Standard Test Method for Tensile Properties of Thin Plastic Sheeting," 2018.

[12] S. Nolte, C. Momma, H. Jacobs, A. Tünnermann, B. N. Chichkov, B. Wellegehausen, and H. Welling, "Ablation of metals by ultrashort laser pulses," *J. Opt. Soc. Am. B*, vol. 14, pp. 2716–2722, oct 1997.

[13] M. D. Shirk and P. A. Molian, "A review of ultrashort pulsed laser ablation of materials," *Journal of Laser Applications*, vol. 10, pp. 18–28, feb 1998.

[14] J. Krüger and W. Kautek, "Ultrashort Pulse Laser Interaction with Dielectrics and Polymers," in *Polymers and Light* (T. K. Lippert, ed.), Advances in Polymer Science, pp. 247–290, Berlin, Heidelberg: Springer Berlin Heidelberg, 2004.

[15] N. Mohd Abbas, D. G. Solomon, and M. Fuad Bahari, "A review on current research trends in electrical discharge machining (EDM)," *International Journal of Machine Tools and Manufacture*, vol. 47, pp. 1214–1228, jun 2007.

[16] B. N. Chichkov, C. Momma, S. Nolte, F. v. Alvensleben, and A. Tünnermann, "Femtosecond, picosecond and nanosecond laser ablation of solids," *Appl. Phys. A*, vol. 63, pp. 109–115, aug 1996.

[17] A. S. M. International, *ISTFA 2013: Proceedings from the 39th International Symposium for Testing and Failure Analysis*. ASM International, 2013.

[18] S. K. Slaughter, J. P. Ligda, T. Sano, and B. E. Schuster, "High Throughput Femtosecond-Laser Machining of Micro-Tension Specimens," in *TMS 2015 144th Annual Meeting & Exhibition*, pp. 471–478, Springer, Cham, 2015.

[19] S. Jakob, M. J. Pfeifenberger, A. Hohenwarter, and R. Pippan, "Femtosecond laser machining for characterization of local mechanical properties of biomaterials: a case study on wood," *Science and Technology of Advanced Materials*, vol. 18, pp. 574–583, dec 2017.

[20] D. J. Magagnosc, J. P. Ligda, T. Sano, and B. E. Schuster, "Femtosecond Laser Machining of Micro-tensile Specimens for High Throughput Mechanical Testing," in *Micro and Nanomechanics, Volume 5*, Conference Proceedings of the Society for Experimental Mechanics Series, pp. 7–9, Springer, Cham, 2018.

[21] K. K. de Groh, B. A. Banks, S. K. R. Miller, and J. A. Dever, "Chapter 28 - Degradation of Spacecraft Materials," in *Handbook of Environmental Degradation of Materials (Third Edition)* (M. Kutz, ed.), pp. 601–645, William Andrew Publishing, jan 2018.

[22] M. J. Pfeifenberger, M. Mangang, S. Wurster, J. Reiser, A. Hohenwarter, W. Pfleging, D. Kiener, and R. Pippan, "The use of femtosecond laser ablation as a novel tool for rapid micro-mechanical sample preparation," *Materials & Design*, vol. 121, pp. 109–118, may 2017.

[23] S.-Y. Yang, ed., *Advanced Polyimide Materials: Synthesis, Characterization, and Applications*. Elsevier, 1 edition ed., may 2018.

[24] K. K. de Groh, D. Waters, J. S. Mohammed, B. A. Perry, and B. Banks, "Analyses of Hubble Space Telescope Aluminized-Teflon Insulation Retrieved After 19 Years of Space Exposure," in *Protection of Materials and Structures From the Space Environment, Astrophysics and Space Science Proceedings*, vol. 32, pp. 13–26, Springer-Verlag Berlin Heidelberg, jan 2013.

[25] H. Kumagai, K. Midorikawa, K. Toyoda, S. Nakamura, T. Okamoto, and M. Obara, "Ablation of polymer films by a femtosecond high peak power Ti:sapphire laser at 798 nm," *Appl. Phys. Lett.*, vol. 65, pp. 1850–1852, oct 1994.

[26] B. Yang, C. Motz, W. Grosinger, W. Kammrath, and G. Dehm, "Tensile behaviour of micro-sized copper wires studied using a novel fibre tensile module," *Int. J. Mater. Res.*, vol. 99, pp. 716–724, jul 2008.

[27] S. Nolte, F. Schrempel, and F. Dausinger, *Ultrashort Pulse Laser Technology: Laser Sources and Applications*. Cham: Springer, 1st ed. 2016 ed., oct 2015.

[28] S. M. Eaton, H. Zhang, P. R. Herman, F. Yoshino, L. Shah, J. Bovatsek, and A. Y. Arai, "Heat accumulation effects in femtosecond laser-written waveguides with variable repetition rate," *Opt. Express*, vol. 13, pp. 4708–4716, jun 2005.

[29] G. H. Michler and F. J. Baltá Calleja, *Nano- and Micromechanics of Polymers: Structure Modification and Improvement of Properties*. Cincinnati: Carl Hanser Verlag GmbH & Co. KG, mar 2012.

[30] C. O. A. Semprimoschnig, P. Gray, M. K. Nehls, and D. L. Edwards, "Accelerated space environmental testing and analysis of ultra-thin polymer films for Gossamer space structures like solar sails," in *The 10th International Symposium on Materials in a Space Environment*, vol. SP-616, mar 2006.

[31] M. Poluektov, J. A. W. v. Dommelen, L. E. Govaert, and M. G. D. Geers, "Characterisation and modelling of anisotropic thermo-mechanical behaviour of oriented polyethylene terephthalate," *Modelling Simul. Mater. Sci. Eng.*, vol. 22, no. 5, p. 055024, 2014.

[32] M. Źenkiewicz, "Effects of electron-beam irradiation on some mechanical properties of polymer films," *Radiat. Phys. Chem.*, vol. 69, pp. 373–378, apr 2004.

[33] Z. B. Wang, M. H. Hong, Y. F. Lu, D. J. Wu, B. Lan, and T. C. Chong, "Femtosecond laser ablation of polytetrafluoroethylene (Teflon) in ambient air," *J. Appl. Phys.*, vol. 93, pp. 6375–6380, may 2003.

[34] Y. Wang, X. Wang, N. Zhang, H. Zhai, and X. Zhu, "Study of ambient air ionization with femtosecond laser pulses," in *Proceedings of the SPIE*, vol. 5627, pp. 105–111, jan 2005.

C

Evaluation of the intergranular crack growth resistance of ultrafine grained tungsten materials

Manuel J. Pfeifenberger [1,*], Vladica Nikolić [1], Stanislav Žák [1], Anton Hohenwarter [2], Reinhard Pippan [1]

[1] Erich Schmid Institute of Materials Science, Austrian Academy of Sciences, 8700 Leoben, Austria
[2] Department of Materials Science, Chair of Materials Physics, University of Leoben, 8700 Leoben, Austria

Abstract

The brittleness of tungsten at room temperature represents a severe challenge particularly for structural applications. Tungsten composites, consisting of foils or wires, overcome this low ductility by utilizing the remarkable mechanical properties of ultrafine grained tungsten materials. A comprehensive understanding of the fracture behaviour of these ultrafine grained tungsten materials is therefore essential for a further development of high performance structural composites. However, the dimensions of specimens used for classical fracture toughness experiments are not applicable to test all important crack growth directions in the case of thin foils and wires, especially, in the direction of the presumably lowest fracture toughness, which is along their characteristically elongated microstructure. Femtosecond laser processing allows to fabricate micro single leg bending specimens, which enable to properly evaluate the fracture toughness in this orientation. The fracture toughness value at crack initiation found for the foil is 2.4 MPa$\sqrt{m}$, whereas for the wire a value of 5.3 MPa$\sqrt{m}$ was determined. In both cases the results are significantly below the values reported for other orientations. This strongly anisotropic fracture behaviour is responsible for the reduced brittle to ductile transition temperature and the delamination induced toughening for crack orientations perpendicular to the elongated

ultrafine grained structure. The distinct difference of the fracture toughness at crack initiation and the R-curve between wire and foil specimens could be primarily explained by the morphologies of the fracture surfaces, exhibiting significantly different roughnesses of the evolving crack paths.

C.1 Introduction

Tungsten (W) is a refractory metal with a unique set of outstanding mechanical and physical properties in the environment of elevated temperatures, which makes it a very prominent material choice for diverse high-temperature applications. In recent years, W-based materials were also identified as main candidates for the divertor and plasma facing components in nuclear fusion reactors [1, 2], which potentially extends the use of W to structural applications. However, significant challenges in this regard are related to the typically brittle nature of W at low temperatures [3]. The overall low fracture toughness and the low ductility at room temperature tremendously restrict both the workability of W, as well as its performance in challenging applications.

Throughout the past decades, extensive research on the ductility enhancement of W was conducted [4]. One particularly promising toughening strategy is the synthesis of laminated and fiber-reinforced composites. Tungsten laminates are synthesized by assembling multilayers of ultrafine grained tungsten (UFG) foils to obtain bulk W materials with enhanced ductility by exploiting the advantageous mechanical properties of the foils [5]. In fiber-reinforced composites the inherent brittleness issue of W can be mitigated through different extrinsic toughening mechanisms, consequently leading to a pseudo-ductile behavior [6]. Such a composite structure is obtained by embedding commercially available drawn W wires in a W matrix, which is produced either by powder metallurgy [7] or by a chemical deposition process [8]. Hence, the principal components which determine the structural integrity of both the laminated and fiber-reinforced composites are heavily deformed UFG polycrystalline W foils and wires, respectively.

In order to produce such UFG materials different techniques can be applied, where very large strains are imposed on coarse grained starting materials [9–11]. Consequently, deformation induced grain refinement during the production leads to the development of unique microstructures of the different grades of materials, like foils, rods and wires. The description of the fracture characteristics of W materials with more complex, polycrystalline microstructures is not straightforward as the resulting crack resistance and occurring failure modes are controlled by many different parameters. However, the microstructural features, such as grain size, grain shape and texture, play a decisive role in the obtained fracture behavior of UFG W materials and are usually responsible for an anisotropic character of their mechanical

properties [12, 13]. The alternation of the microstructure of W foils and wires to the UFG size results in an extraordinary combination of both increased strength [14, 15], as well as high fracture resistance for crack propagation perpendicular to the drawing (DD) or rolling (RD) direction [16, 17].

The lamellar and fibrous microstructures of UFG W foils and wires are undoubtedly the key controlling features of the predominant failure micromechanism, which is clearly reflected in the materials fracture behavior. Fig. C.1 shows fracture surfaces of samples investigated by Nikolić et al. [16, 17]. The crack front was oriented perpendicular to the RD for the foil sample and perpendicular to the DD for the wire, respectively. The conspicuous fracture surfaces exhibit pronounced delaminations for both, the foil and the wire. The magnified inset in Fig. C.1b shows the fracture surface of the wire in a top view and reveals, besides large cracks along the DD, also delaminations between each of the the single fibres. Furthermore, the wire displays a distinct crack deflection. The observed crack path along the DD of the wire and along the RD of the foil, respectively, is a strong indication that the fracture resistance along DD and RD is significantly lower. This implies the existence of a very pronounced fracture toughness anisotropy in both materials [16, 17].

Thus, an essential part in a comprehensive understanding of the basics of the delamination toughening mechanism is to determine the fracture characteristics along the elongated grains, the so-called "weak" crack propagation direction. For the present materials this was impossible to realize for classical macro-scale fracture mechanics samples (typically in the range of several millimeters), as the sample size requirements and the realization of an appropriate experimental setup were restricted by the dimensions of the foils and wires, which are commonly in the range below one millimeter. A feasible approach of assessing the fracture properties would be to prepare samples with a focused ion beam (FIB) station. Considering the large material volumes that need to be removed for the present wires and foils, this approach is on the one hand time consuming, especially as a Gallium FIB yields a particularly low sputter rate for W [18]. On the other hand, the typical sample dimensions of FIB specimens would be far smaller. However, the evaluation of the fracture properties on such small scales may bear the problem of not complying with requirements for fulfilling small or large scale yielding conditions. Our approach is the utilization of femtosecond (fs) laser processing, which enables a fast and precise preparation of suitable micro-mechanical samples [19].

The aim of the paper is to determine the fracture toughness of W foils and wires with the designated crack propagation direction along the aligned microstructure. The main goal is to present a solid experimental approach to study fracture properties on the meso-scale (in the range of hundreds of micrometers) to allow a complete description of the anisotropic fracture behavior of UFG tungsten materials.

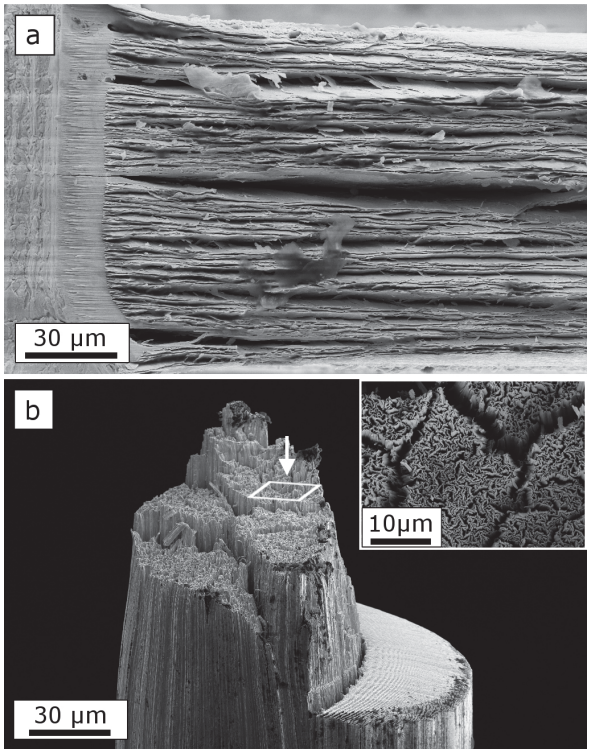

Figure C.1 The fracture experiments performed in [16, 17] suggest a significant fracture toughness anisotropy of ultrafine grained tungsten materials. (a) The fracture surface of the foil tested perpendicular to the rolling direction exhibits pronounced delaminations along the rolling direction, hence, normal to the initial crack front. (b) The fracture surface of the wire reveals a crack deflection along the drawing direction. The inset reveals, besides large cracks along the drawing direction, also delaminations between single fibres.

C.2 Materials and methods

C.2.1 Materials

The materials used in this study were a potassium doped tungsten (K-W) wire with a diameter of 150 μm and a technically pure W foil with a thickness of 100 μm.

A Leo 1525 (Zeiss, Oberkochen, Germany) field-emission-gun scanning electron microscope (SEM) with an electron backscatter diffraction (EBSD) detector (EDAX Inc., New Jersey, USA) was used for the investigation of the microstructure. The EBSD data was analysed with the EDAX OIM Data Analysis software. To provide details on the microstructure EBSD orientation maps for each material were taken from the three principal directions (see Fig. C.2). For the foil, along with the rolling direction, also the transverse direction (TD) and the short transverse direction (SD)

are indicated. In Fig. C.2b the DD and, additionally, the contour of the wire sample are displayed. The orientation maps were determined using an acceleration voltage of 20 kV and a scanning step size of 100 nm.

The microstructure of the foils consists of very thin, elongated grains, aligned into in the rolling direction, thus forming a characteristic "pancake-like" microstructure [20, 21]. Along with the large aspect ratio of the grains also a pronounced rotated-cube crystallographic texture is typical for the anisotropic microstructure. Fig. C.2b shows the EBSD orientation maps of the commercially available UFG K-W wires. A very high degree of deformation, which is imposed through the drawing process, leads to the development of a unique "bundle of fibers" microstructure. Such a microstructure is characterized by extremely elongated grains along the DD and the development of a very pronounced ⟨110⟩ fibre texture perpendicular to it. In the cross section of the wire a distinctive pattern known as grain curling can be observed, with ribbon shaped grains of a significantly smaller dimensions twisted around each other [22].

Material	Hardness [HV 0.5]	Tensile strength [MPa]	Mean grain thickness [μm]	Mean grain length [μm]	Aspect ratio [-]
K-W wire	665	2774	0.30	1.09	0.28
W foil	598	≈2300	0.37	1.08	0.35

Table C.1 Mechanical and microstructural features of the investigated materials (taken from [14, 16, 22, 23]).

In Tab. C.1 important mechanical and microstructural features of the investigated materials are summarized. The listed grain dimensions were determined via the intercept method, hence, the heavily deformed microstructure leads to a good estimation regarding the mean grain thickness but the mean grain length provides only a lower estimate of the real value. However, the EBSD scans in Fig. C.2 exhibit that individual grains reach a length in the 10 μm range. Further details of these materials and a comprehensive characterization of the microstructures can be found in [16, 22].

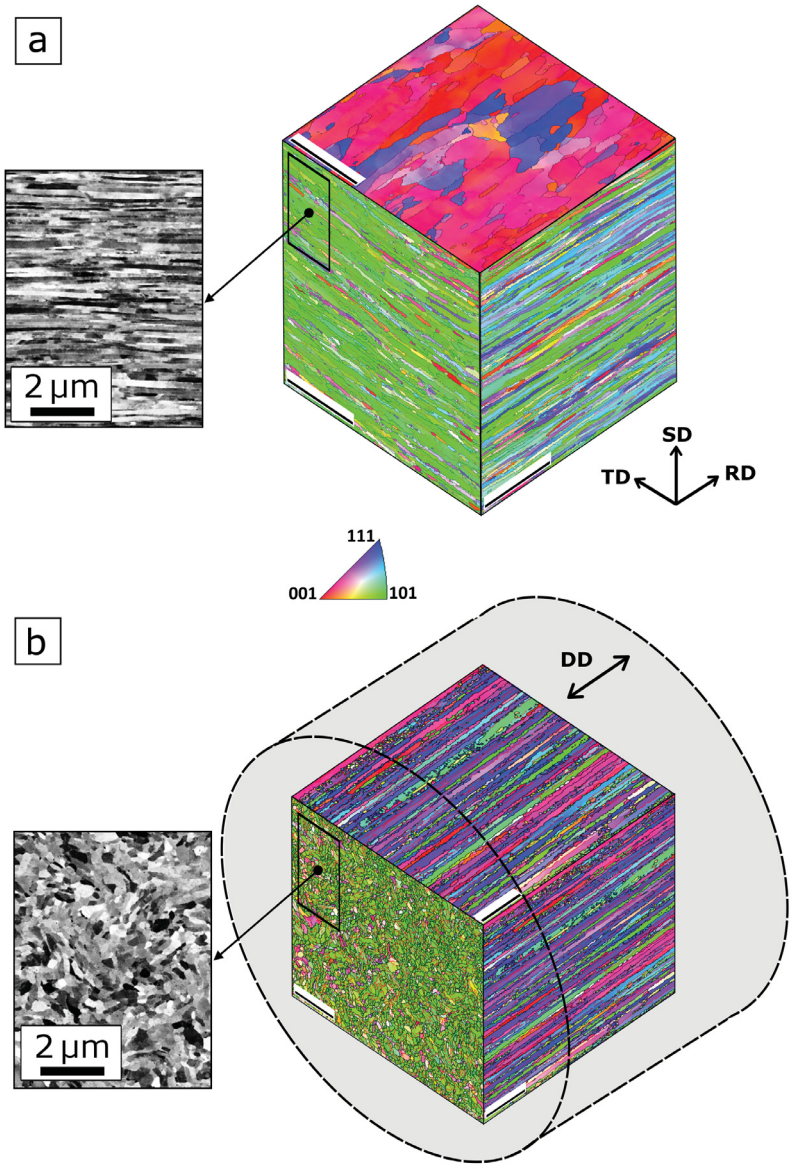

Figure C.2 EBSD orientation maps of the three principal axes of (a) a pure W foil and (b) a K-W wire. The color coded unit triangle shown in the middle represents the crystallographic directions ⟨100⟩, ⟨110⟩ and ⟨111⟩ perpendicular to the sample surface. The indicated scale bars correspond to 10 μm in (a) and to 5 μm in (b). In (b) the contour of the wire is displayed. The microstructure is clearly visible in the backscatter electron images with a higher magnification, which are presented in the insets. The fibrous grains of the wires show the characteristic curled structure, whereas the pancake like microstructure of the foil yields a distinct lamellar structure.

C.2.2 Femtosecond laser system

In this study an Auriga laser system (Zeiss, Oberkochen, Germany), combining a FIB and a SEM was used. This system further includes an Origami 10 XP femtosecond laser (Onefive GmbH, Regensdorf, Switzerland) with a pulse duration of 500 fs. Details on the laser upgrade of the system can be found elsewhere [19].

For the sample processing a wavelength of $\lambda = 515\,\mathrm{nm}$ was used. The minimal focal diameter at the sample surface is approximately $20\,\mu\mathrm{m}$. The evaluation of the sample quality and the fracture surfaces was conducted via SEM imaging. The surface profile evaluation of the fracture surfaces was performed via an Olympus LEXT OLS 4100 confocal laser scanning microscope (CLSM).

C.2.3 Sample preparation

The testing of the weak fracture direction was performed by means of single leg bending (SLB) specimens [24]. In the presented sample size regime this geometry is advantageous compared to conventional double cantilever beam specimens since the application of the load on only one leg represents a useful simplification (see Fig. C.4a). The samples were fabricated using fs-laser ablation and finally a notch was introduced via FIB. Details on the sample preparation can be found in appendix A.

The important dimensions of the final samples, which are the notch length, a, the height of the legs, t_1 and t_2, the thickness, b and the clamp length c, were measured with the SEM. Some of the dimensions are indicated in Fig. C.3a. Typical values are: $a \approx 500\,\mu\mathrm{m}$, $b \approx 45\,\mu\mathrm{m}$, $c \approx 1200\,\mu\mathrm{m}$, $t_1, t_2 \approx 75\,\mu\mathrm{m}$ for the wire specimens and $t_1, t_2 \approx 50\,\mu\mathrm{m}$ for the foil specimens. The exact values of all samples are summarized in appendix A.

Fig. C.3a shows a SLB sample fabricated from a K-W wire. A magnified view of the tip of the notch is displayed in Fig. C.3b. The fs-laser cut notch has a width of about $20\,\mu\mathrm{m}$ and a taper on the notch flanks with an angle of approximately 15 to 20°. Hence, also the front of the FIB notch is not perpendicular to the surfaces of the thinned section but shows an inclination, according to the taper of the laser cut. This means that the notch length on the side being observed with the SEM is somewhat longer than at the backside of the sample.

For the SEM in-situ experiments 6 SLB samples were prepared. 3 from K-W wires and 3 from W foils. The crack propagation direction of the foil samples was oriented parallel to the RD. Additionally, 3 K-W wire samples were tested under a stereo microscope, but since the crack extension could not be accurately measured these test are not discussed further. Nevertheless, it should be mentioned that the recorded force displacement curves and the fracture behaviour were similar to the presented experiments, yielding similar fracture toughness values.

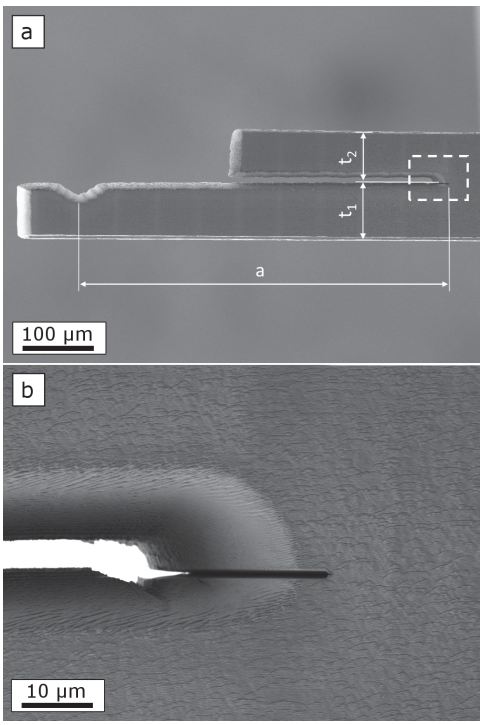

Figure C.3 (a) SEM micrograph of a micro-SLB sample fabricated from a K-W wire. The crack length a and the height of the legs, t_1 and t_2, are indicated. (b) Magnification of the dashed inset shows the FIB notch, as well as the taper of the laser cut. The fs-laser processed surfaces show typical fs-laser related surface structures with a roughness in the few hundred nm range [25].

C.2.4 Setup of single leg bending experiments

The testing of the SLB specimens was conducted with a Kammrath & Weiss fibre tensile module [26]. This device provides a maximum force of about 2 N with approximately 10 μN resolution and an accuracy in displacement registration of about 30 nm. The samples were tested in-situ in a Leo 1525 field-emission-gun SEM. A mounted sample and the setup of the testing is sketched in appendix A (see Fig. A.1a). The loading of the longer leg of the SLB specimen was achieved using a bent W wire with a diameter of 100 μm mounted in a fork-like clamp (see Fig. C.A.1a). All experiments were displacement controlled, while the force was recorded. The testing speed was 0.5 μm/s. Each sample was deformed until the crack reached the end of the thinned area. The tests were performed at room temperature (22°C) under a pressure of about 2×10^{-5} mbar. Along with load and crack length, the crack mouth opening displacement (CMOD) was measured 100 μm behind of the initial notch tip, as indicated in Fig. C.4.

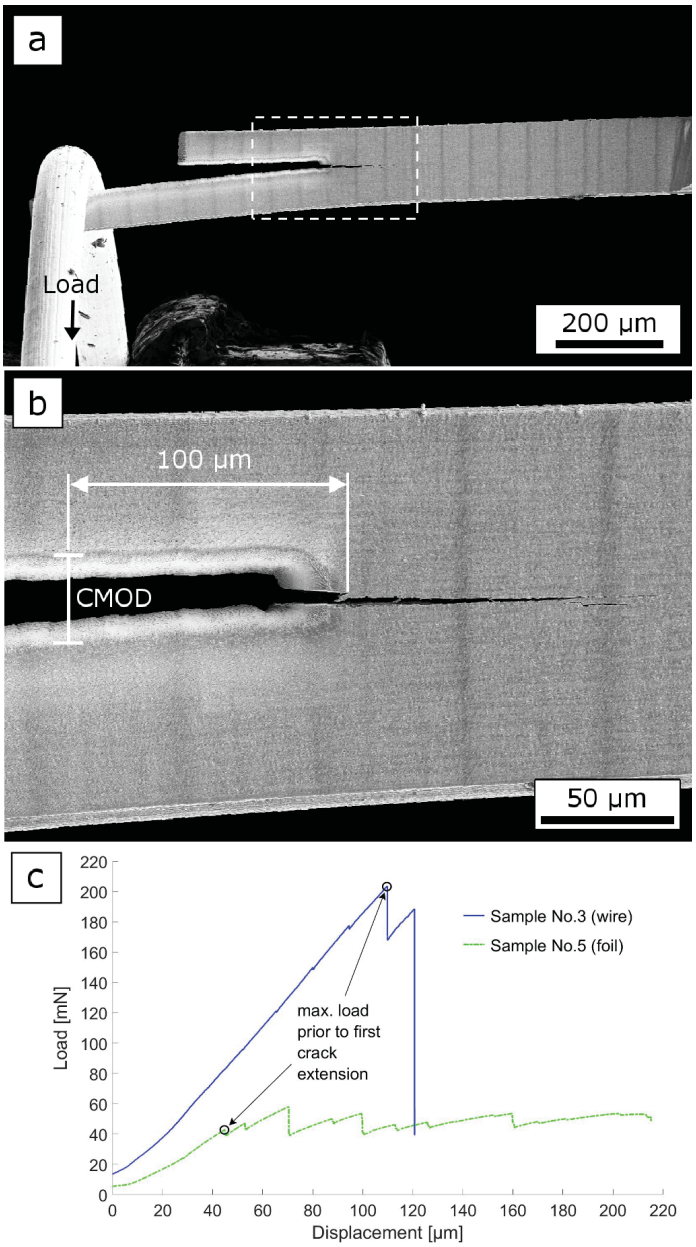

Figure C.4 SEM micrographs of the in-situ experiment exemplarily for a wire sample: (a) in loaded state with elongated crack, (b) magnified detail of the area indicated in (a). In all experiments the CMOD was measured 100 μm behind of the initial notch tip. (c) Exemplary load versus displacement curves for a wire and a foil sample recorded during the SLB experiments. The points used for the evaluation of the initiation values, K_{Ii} and K_{IIi}, are indicated.

C.3 Results

Two exemplary load versus displacement curves, one for a foil and one for a wire sample, are shown in Fig. C.4c. The wire samples reach significantly higher maximum load values, before the final failure − an unstable crack extension to the end of the thinned sample area − occurs. On the contrary, the crack in the foils samples starts to grow at lower loading values in a more stable manner. The difference in the maximum load between the two sample materials is partly owing to the different dimensions of the samples.

During the in-situ experiments either after an increment of 20 mN or after a drop in the load signal, due to a crack extension, the loading of the sample was stopped and micrographs were recorded. These micrographs allow the determination of the crack elongation and the corresponding CMOD. The stress intensity factor evaluation of the experimental data was performed according to Davidson et al. [24, 27]. The analytical equation is presented in the supplementary information. The input parameters regarding the geometry of the specimens are listed in Tab. C.A.1. For the calculation of the initiation fracture toughness values K_{Ii} (mode I component) and K_{IIi} (mode II component) the initial crack length and the load value corresponding to the first crack growth observed in the SEM (indicated in Fig. C.4c) were used. In addition also the fracture toughness values for the crack propagation after the first crack extension K_{Ii1} are calculated. The results for the analytically determined K_{Ii-Ex}, K_{IIi-Ex} and K_{Ii1-Ex} of each sample are compiled in Tab. C.2. After the first observed crack extension a straight crack front, perpendicular to the observed surface, is formed. This was confirmed with an additional experiment measuring the crack length after the first crack extension on both sides of a foil sample. K_{Ii-Ex} and K_{IIi-Ex} may contain a slight overestimation for the wire samples, as the first crack growth on the observed surface probably is not coinciding with the first crack growth on the side of the shorter notch (on the backside of the sample).

The loading of a single leg bending specimen generates besides mode I loading also a mode II component with a ratio K_{II}/K_I of about 0.8 (see Tab. C.2). However, the crack propagation path did not exhibit a deflection (fracture angle $\theta \approx 0$). For the description of mixed mode fracture different criteria exist, the most common are the maximum energy release rate criterion [28] and the maximum tensile stress criterion [29]. For $\theta \approx 0$ the first criterion yields the mode I fracture toughness values K_{GIc} listed in Tab. C.2 according to [30]. Considering the maximum tensile stress criterion, however, the resulting mode I fracture toughness corresponds to the listed K_I values. For brittle metallic materials it was found that the results are well described by the maximum tensile stress criterion [31, 32]. Hence, in the present semi-brittle case it is assumed that the mode I component controls the failure behaviour of the sample for the case of $\theta \approx 0$. Therefore, in the following only the mode I component of the stress intensity is discussed.

Strong differences between both materials are evident in the crack resistance curves displayed in Fig. C.5. The K_{Ii} value at crack initiation for wire samples is by a factor of approximately 2.2 higher compared to the foil samples (see Tab. C.2). An exception from this was wire sample no. 2, which showed a first crack initiation adjacent to the FIB introduced notch (see Fig. C.B.1 in appendix B). Taking the respective loading value into account, K_{Ii} yields a value of 3.49 MPa$\sqrt{m}$ in this case. However, the critical crack, which leads to the final failure starts at a higher load value directly in front of the FIB notch. Calculating K_{Ii} for this critical crack initiation yields 5.24 MPa$\sqrt{m}$. A possible explanation for the first crack initiation observed besides the notch could be a pre-existing defect near the surface.

Additionally for the wire samples a maximum of 3 crack extensions could be observed in the SEM before the final failure occurred. The largest observed crack elongation of the wire samples before this final failure was 128 μm. The maximum increase of the K_I value was found to be about 1.5 MPa$\sqrt{m}$. On the contrary, the crack in the foil samples grows with smaller, relatively constant step sizes whilst showing a rise of the K_I value to about 5 MPa$\sqrt{m}$, hence, approximately doubling its initiation value. The K_I values before and after a particular crack elongation are shown in Fig. C.6 exemplary for sample no. 2 (wire) and sample no. 5 (foil). Whereas the value of the K_I slightly decreases after each crack elongation for the foil sample, an increase is found for the wire sample. This behaviour was the same for all wire and foil samples respectively and will be discussed later.

Sample	Analytical results				FE simulation results			
No.	K_{Ii-Ex}	K_{Ii1-Ex}	K_{IIi-Ex}	K_{GIc-Ex}	K_{Ii-Si}	K_{Ii1-Si}	K_{IIi-Si}	K_{GIc-Si}
Wires								
1	**5.13**	5.47	4.60	6.89	5.47	6.16	3.05	6.26
2	**5.24**	6.01	4.48	6.89	5.65	6.90	2.81	6.31
3	**5.57**	6.48	4.88	7.41	6.18	7.30	3.59	7.15
Foils								
4	**2.43**	2.68	1.99	3.14	2.75	2.96	1.86	3.32
5	**2.30**	2.76	1.96	3.02	2.49	3.07	1.56	2.94
6	**2.46**	2.60	2.05	3.20	2.97	2.85	1.62	3.38

Table C.2 The stress intensity values for crack initiation (K_{Ii} and K_{IIi}) and for crack propagation after the first crack extension (K_{Ii1}) determined by means of SLB in-situ experiments (subscript -Ex) are listed for wire and foil samples. Additionally, the respective results from the FE simulations are given (subscript -Si). Further, also the fracture toughness values calculated according to the maximum energy release rate criterion K_{GIc} [30] are shown. All values are in MPa$\sqrt{m}$.

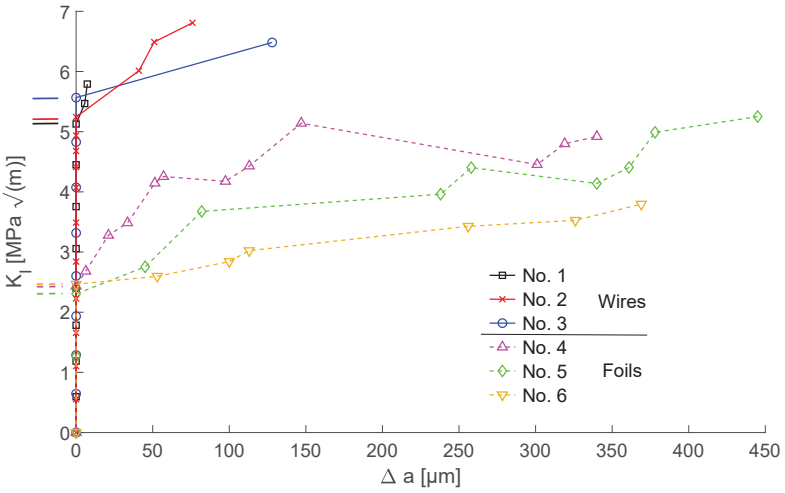

Figure C.5 K_I versus crack elongation Δa recorded during the in-situ SLB experiments. The K_{Ii-Ex} values, listed in Tab. C.2, are indicated by horizontal lines on the left side of the ordinate.

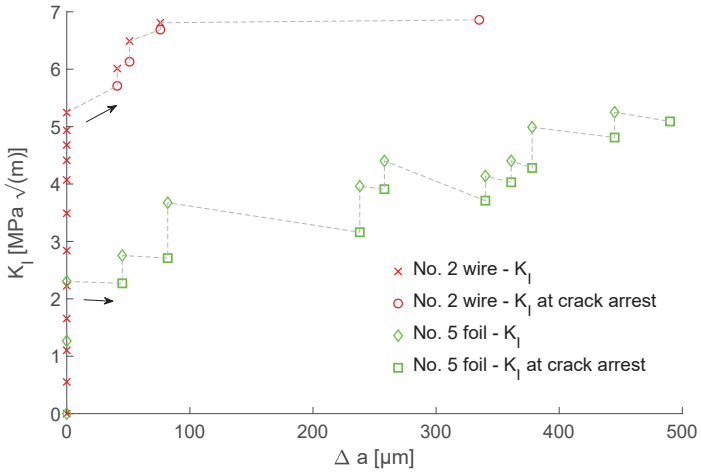

Figure C.6 K_I versus crack elongation Δa of the wire sample no. 2 and the foil sample no. 5 recorded during the in-situ SLB experiments. Further indicated are the K_I values at the first crack arrest. Whereas the wires show an increase of the K_I value after each crack elongation, the foils show a decrease.

SEM images of the fracture surfaces of a wire and a foil sample are displayed in Fig. C.7a-b and Fig. C.7c-d, respectively. In contrast to the fracture surfaces of the foil samples, which are nearly perfectly flat, the fracture surfaces of the wire show a rough, jagged structure. This difference can be related to the microstructures of these materials and the intergranular fracture prevailing in the present experiments. The fibrous microstructure of the wires leads to a rougher structure compared to the pancake like microstructure of the foils. Fig. C.7e displays the height profile of the fracture surfaces across the thickness of a wire sample and a foil sample, as indicated in Fig. C.7a and c, measured using a CLSM quantifying the distinct difference in roughness.

To achieve further understanding and a validation of the analytical results additional investigations by means of finite element (FE) modelling were conducted. Details on the FE modelling can be found in the supplementary informations. In addition a verification of the stiffness compatibility of the modelled sample and the experimentally tested samples was conducted to allow a proper comparison of simulation and experiment.

The resulting stress intensity factors deduced from the simulations for the same initial loads as found in the experiments are presented in Tab. C.2 and named as K_{Ii-Si}, K_{Ii1-Si} and K_{IIi-Si}. All K_{Ii-Si} are slightly higher than the K_{Ii-Ex} values and deviate at maximum 13% from the analytical solution. These deviations can stem on the one hand from the inclined notch or on the other hand from geometrical idealisations assumed in the modelling process (e.g. no taper on the laser notch flanks). Furthermore, the FE simulations yielded somewhat lower ratios of K_{IIi}/K_{Ii} between 0.5 and 0.7. This lower ratios can be linked to the influence of the inclined notch configuration at crack initiation. Further simulations regarding the effect of the inclined notch on the resulting K_{Ii} values showed only a negligible influence. A detailed description of the findings is given in the supplementary information.

C.4 Discussion

A requirement for a valid characterization of the crack-tip conditions via the calculated K values is that the condition for small scale yielding (size of the plastic zone r_p << sample dimensions) needs to be fulfilled. The r_p in front of the crack tip for plane stress is estimated by [33]

$$r_p = \frac{1}{\pi} \frac{{K_I}^2}{{\sigma_{ys}}^2}, \tag{C.1}$$

with a yield strength σ_{ys} of approximately 2200 MPa for both material types [14, 23]. Inserting the determined K_{Ii} values yields a size of about $r_p = 0.4\,\mu$m for the foils and $r_p = 1.9\,\mu$m for the wires. Therefore, considering the present specimen geometry

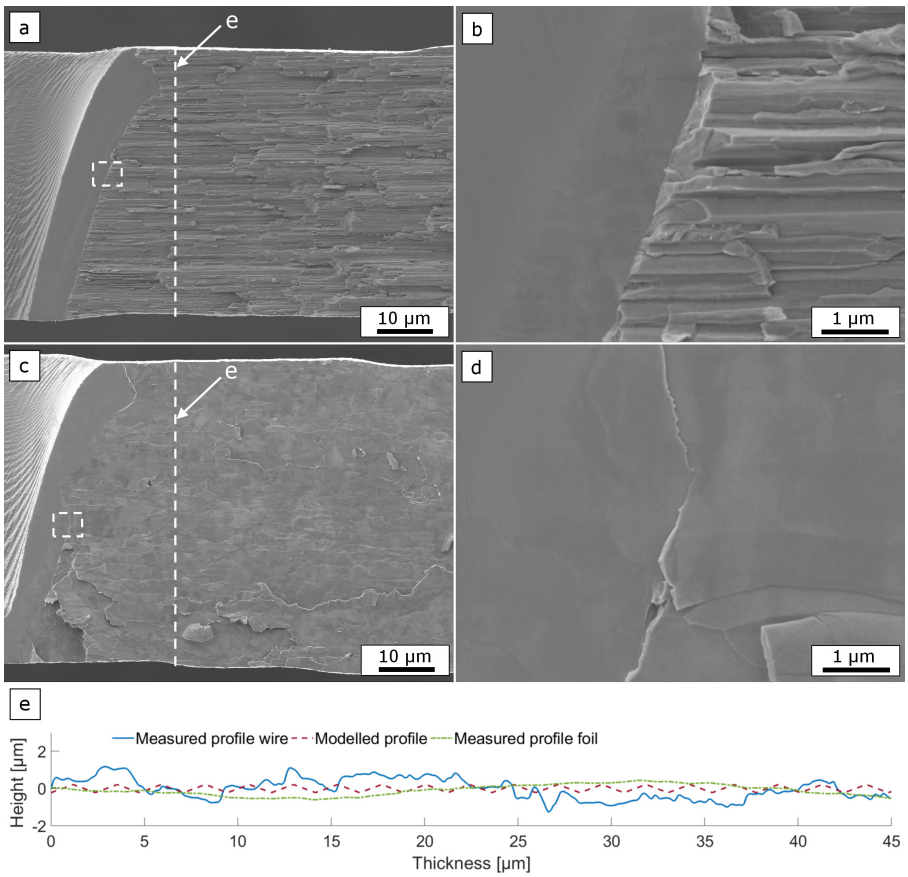

Figure C.7 Fracture surfaces of a wire sample (a) and a foil sample (c). (b) and (d) show a magnification of the dashed rectangles in (a) and (c). The surface morphology of the fracture surfaces strongly differs between the two materials. The wires show a rough, jagged structure, whereas the foil samples show a flat "pancake"-like structure. (e) The continuous and the dot and dash line display the profiles of the fracture surfaces measured using a CSLM along the dashed lines indicated in (a) and (c). The dashed line shows the simplified rough surface profile used for the FE modelling described in Sec. C.4.1.

(see Tab. C.A.1), small scale yielding conditions are fulfilled for the investigated specimens even for the conservative plane stress estimation of the plastic zone size. This supports the selection of the investigated sample size with dimensions much larger than usually fabricated with a FIB. Using the FIB technique, with dimensions usually limited to few times the size of the evaluated r_p, together with a K-based evaluation would not be suitable due to the large occurring plastic zone in the case of the W wires. In addition, to record the R-curve behaviour and to characterize the bridging process multiple grains along the crack path are required. For that a

minimum size of the specimens in the range of a few tens of μm is needed for the respective grain sizes.

Despite the successful evaluation of the fracture properties in the weak direction, some further questions arose. The discussion of them can be based on two alternative approaches for fracture analysis: the stress-strain approach and the energy approach [33].

In the stress-strain approach the stress intensity can be divided in a intrinsic resistance (k_i) and a contribution of a shielding stress intensity (k_s), which in the present case is caused by bridging (k_b) and dislocation shielding (k_d)

$$K_I = k_i + \underbrace{k_b + k_d}_{k_s} . \tag{C.2}$$

The determination of the shielding contribution, however, is not straight forward, therefore, the somewhat simpler energy approach will be used in this discussion. In this approach three different contributions to the material resistance to crack extension R can be stated [33]

$$K_I^2/E \propto R = 2\,(\gamma_s + \gamma_b + \gamma_d)\,, \tag{C.3}$$

with γ_s being the specific energy required for the creation of new surface by decohesion, in the investigated case, along a grain boundary. γ_b considers the contribution of the energy required for the deformation and failure of bridges during crack growth and γ_d the contribution of plastic deformation in front of the crack tip.

C.4.1 What is the origin for the large difference in the initiation toughness between W foils and wires?

The determination of the initiation toughness in very brittle materials is always a difficult task [34]. The FIB permits to generate very sharp notches with a root radius of about 10 nm [35]. Nevertheless, such a notch root radius is far from being atomically sharp, and much more important, the notch is not very likely to be located in the weakest crack path, which means the notch being within the grain boundary. In the investigated case the thickness of the fibrous and the pancake-like grains is few 100 nm, hence, the probability for the perfect placement of the notch at a grain boundary is not very high. However, in the pancake-like microstructure of the foils the alignment with the straight notch is more favourable for crack initiation than in the fibrous microstructure of the wires. Therefore, it should be somewhat easier to determine the initiation toughness in this case.

The presented experiments and FE simulations revealed a distinct difference between foil and wire samples, regarding the initiation value K_{Ii}. This difference of the stress intensity value at crack initiation (and also for K_{Ii1} after the first crack arrest) can mainly be based on the different roughness of the fracture surface.

In the description of the energy approach, the higher fracture toughness value of the rough crack front can be connected to the increased surface area compared to the relatively flat fracture surface of the foil and the accordingly larger energy required to create the new surface. Considering the measured roughness profile of the wires the fracture surface is $\approx 30\%$ larger compared to the case of a perfectly flat surface. Therefore, with respect to Eq.(3), this results in an $\approx 14\%$ increase of K_I.

Additionally, for a more detailed understanding of the influence of the increased roughness, an evaluation by means of a FE simulation, exemplarily for sample no. 2, was conducted. The rough crack front was modelled using the simplified model of the measured wire profile shown in Fig. C.7e. Besides its simplified structure, it also has a reduced average roughness. These simplifications are required to establish the computational feasibility of the FE simulations. For the calculation of the local k_I the same loading as for the model with the flat crack front was applied to the model with the rough crack front. In Fig. C.8 the resulting variation of the local k_I across the sample thickness starting from its center is depicted for both cases. The respective mean values are indicated by horizontal lines. For the rough crack front the loading is not exclusively perpendicular to the crack front across the thickness. Additional mode II and mode III components of k are induced locally, depending on the local inclination of the crack front with respect to the loading direction. Therefore, the k_I driving force exhibits a distinct fluctuation and on average a decrease of its value is found. The mean k_I value of the rough crack front is approximately 22% lower than the mean value of the flat crack front. However, this contribution to the decrease of the k_I value is based on the simplified surface profile. Hence, using a profile with the same average roughness as, or even using the real profile, a further reduction of k_I might be expected. This assumption is supported by findings of FE simulation studies on rough crack fronts by Pokluda et al. [36] for mode I loading and similar by Žák et al. [37, 38] for mode II loading. Nevertheless, a more elaborated treatment of the surface profile model in the present study would require a substantial enhancement of its complexity.

The different mode mixity and the connected decrease of the mean k_I value for the wires is after all not sufficient to describe the total difference in the crack initiation toughness compared to the foils. Hence, the contributions of plastic deformation γ_d in front of the crack tip and bridging γ_b, which also influence the initiation toughness, need to be considered. Although, the conducted experiments in the present study do not allow an exact quantification of both terms. In the case of the wires a significant amount of bridging can be expected already at crack initiation. Firstly, due to the formation of many small bridges in the case of the wires, compared to few large ones in the case of the foils (see Sec. C.4.2) and secondly, due to the non-optimal alignment of the initial notch with the fibrous microstructure of the wire. Furthermore, in the case of the wires the plastic deformation γ_d in front of the crack tip is likely to be

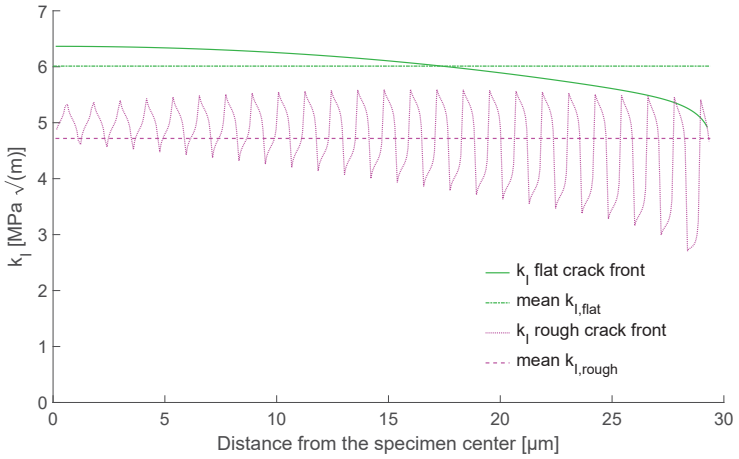

Figure C.8 Local k_I variation across the specimen thickness retracted from a FE simulation exemplarily for sample no. 2. Once for the modelled rough crack front shown in Fig. C.7 and once for a perfectly flat crack front. The mean value decreases for the rough crack front by about 22%.

more pronounced due to the increased mode III component compared to the case of the foils. For coarse grained polycrystalline W materials plastic deformation of neighbouring grains along an intergranular crack growing path was observed if a pronounced local mixed mode loading occured [12].

In comparison with the weak specimen orientations the principal testing direction of UFG W samples exhibits a significantly higher fracture toughness. Wires yielded lower limit values of $22.6-37.0\,\mathrm{MPa}\sqrt{m}$ (elasto-plastic evaluation would yield larger values) for crack propagation perpendicular to the DD [17]. In fracture experiments on foils a lower limit for the fracture toughness of $94.8\,\mathrm{MPa}\sqrt{m}$ for propagation perpendicular to the RD and $11.9-105.9\,\mathrm{MPa}\sqrt{m}$ for crack propagation parallel to the RD was found [16]. The testing was performed at room temperature, which is in the temperature range of the brittle to ductile transition of heavily deformed tungsten materials [3], therefore, the fracture toughness values exhibit a large scatter. The low fracture toughness along the aligned grain structure permits the enormous delamination toughening in the other loading directions and the reduction of the brittle to ductile transition temperature of tungsten to the room temperature regime.

C.4.2 How can the difference in the R-curve behaviour between the two materials be interpreted?

Due to the inclination of the notch, the crack should start at the shorter notch length (i.e. at or near the opposite of the SEM observed side), where the stress intensity

is significantly larger. With increasing crack extension the crack becomes visible on the longer notch side and the inclination of the crack front should disappear. Hence, the K_{Ii} is the mean stress intensity value where the crack tunnels from the back side to the observed side of the sample. In addition, in Tab. C.2 also K_{Ii1} is given, which is the stress intensity factor when the crack starts to propagate after the first visible crack arrest. In this case really the propagation condition of a crack located on the weakest crack path is investigated. However, one has to take into account that in this case already a certain contribution of the R-curve is included.

Besides the difference at crack initiation also the crack propagation differs between foil and wire samples (see Fig. C.5 and Fig. C.6), which can be explained by a different bridging behaviour. For all samples intergranular fracture prevails along the crack propagation direction as obvious by the fracture surfaces in Fig. C.7. However, looking at the fractographs of the wire samples many small ledges can be identified (see Fig. C.7a and b). This can be related to the microstructure of the wires (see inset in Fig. C.2a). The fibrous microstructure and the additional grain curling leads to a three dimensional bonded interconnection of the grains. In addition, the shape of this grains exhibits a higher resistance against bending compared to the pancake like grains of the foils (see inset in Fig. C.2b). Hence, the formation of large bridges is impeded. Fig. C.9a shows the crack tip of a wire sample. The fracture behaviour of the wires only allowed to capture the crack tip at the end of the thinned sections of the samples after the final failure occurred. A rough, frayed crack path due to the formation and rupturing of many small bridges can be observed. The larger number of small bridges and their higher stiffness yields a faster increasing contribution of γ_b to K_I in the case of the wires. This explains the steep increase of K_I in total and the increase of K_I after each crack extension, as shown in Fig. C.6. On the contrary for the W foil K_I is always smaller after crack propagation.

In contrast to the wires, the fracture surfaces of the foil specimens show fewer but significantly larger bridges. Fig. C.9b displays a crack of a loaded foil sample, where three bridges, with a distance of about $10\,\mu$m in between, are indicated. The bridges generated while loading a foil sample exhibit a distinct plastic deformation as only thin layers of the lamellar structure are more or less peeled off and bent, therefore, leading to a smoother crack path compared to the wires. Furthermore, these bridges cause the arresting of the crack in relatively constant step sizes (see Fig. C.5).

C.5 Conclusions

In this study a successful preparation method of micro single leg bending specimens, from tungsten foils and wires in the $100\,\mu$m regime, using a femtosecond laser is presented. This micro specimens allow to test the fracture toughness in the direction

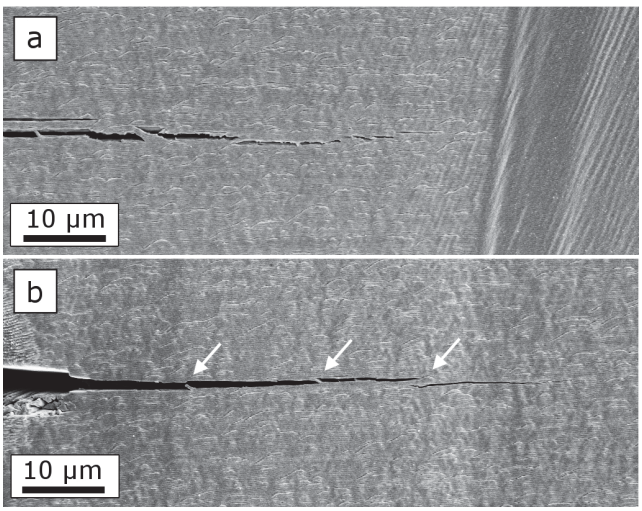

Figure C.9 (a) The arrested crack at the end of the thinned section of a wire sample displays a rough crack path, consisting of many small bridges. (b) The crack of a loaded foil sample shows the onset of few bridges (indicated by arrows) behind the crack tip. These bridges exhibit a low resistance against plastic deformation due to their flat, lamellar structure.

of the elongated microstructure, where testing is usually very challenging due to geometrical limitations of the initial materials. These challenges arise regarding the sample preparation and the respective experimental procedures. In-situ experiments revealed a significant difference of the fracture toughness in the weak specimen direction between the foil and the wire samples, although for both intergranular fracture prevails. The experimentally obtained value for the fracture toughness at crack initiation was 5.3 MPa$\sqrt{m}$ for the wires and 2.4 MPa$\sqrt{m}$ for the foils respectively.

The difference of the fracture toughness can primarily be attributed to the distinctively different microstructure of the two materials, which leads to a strongly different roughness of the fracture surfaces. Whereas the foil samples show a nearly perfectly flat fracture surface, the wire samples exhibit a jagged, rough morphology. Finite element simulations indicate that during loading the change in the local mode mixity, due to the higher roughness, mainly contributes to the higher fracture toughness of the wires. In the case of the wires the crack propagation is primarily governed by a large amount of small stiff bridges, resulting in a fast increase of the crack resistance followed by final failure. Along the crack path of the foil samples, less bridges with lower stiffness were found, therefore, this material exhibits a slower increase in crack resistance.

The results of this study deliver the fracture toughness values for intergranu-

lar fracture along a heavily deformed microstructure, hence, enabling a complete description of the anisotropic fracture behavior of ultra fine grained tungsten materials

Acknowledgments

This work has been carried out within the framework of the EUROfusion Consortium and has received funding from the Euratom research and training programme 2014-2018 and 2019-2020 under grant agreement No 633053. The views and opinions expressed herein do not necessarily reflect those of the European Commission.

Appendix C.A

The SLB specimens were fabricated using a fs-laser and a FIB. Prior to the fs-laser processing a piece of the wire with a length of about 6 mm was cut using scissors. For the foil samples a slice with dimensions of about 6 mm × 200 μm was cut from a larger piece with the fs-laser. Afterwards each of these samples was mounted in a clamp, as shown in Fig. C.A.1a. On one side the specimen protrudes approximately 1.5 mm out of the clamp to enable processing in this area. After the sample processing the specimen holder can directly be mounted into the testing device. Furthermore, the viewing directions u and v for Fig. C.A.1b are indicated. The viewing direction v corresponds to the fs-laser incidence direction.

The fabrication of the SLB samples is conducted in four steps: The first three steps are shown in Fig. C.A.1 in two different viewing directions u and v. Initially the wire or foil specimen was thinned to a lamella with a thickness b of 40 to 50 μm (step 1 and 2). After that the SLB contour is cut into the lamella. Finally, in the last step a FIB notch is introduced in the fs-laser pre-notched sample.

In the first and the second step the laser beam is scanned in meander-like manner in parallel lines towards the sample center. This is indicated by the parallel green lines and the broad arrow in (v.1) and (v.2) in Fig. C.A.1b. The goal on the one hand is a parallel thinning of the sample. On the other hand the appropriate horizontal positioning of the lamella in the specimen holder needs to be obtained to enable a proper loading of the sample (see Fig. C.A.1a.2). Therefore, the positioning during laser processing plays a critical role.

Fig. C.A.1a shows the specimen holder in its initial orientation ($\omega = 0°$), which corresponds also to the orientation during testing. In the first step the clamp is rotated around the rotation axis shown in Fig. C.A.1a for $\omega = 90° + \alpha$ (see (u.1) in Fig. C.A.1b). The additional tilting angle α accounts for the expected taper, which is a typical feature of laser processed surfaces [19]. This taper angle is compensated by appropriate overtilting. Secondly the clamp is rotated to $\omega = 90° - \alpha$ (see (u.2)

in Fig. C.A.1b). This results in the parallel orientation of the two processed surfaces. The thickness b of the fabricated lamella is indicated in detail (u.3) in Fig. C.A.1b. In the third step the sample is rotated back to its initial position with $\omega = 0°$ (see (u.3) in Fig. C.A.1b). This step is divided into three sub-steps (indicated in detail (v.3) of Fig. C.A.1b): (I) The laser notch is introduced via a single line cut. (II) One leg is shortened, to provide space on the second one for a gripper to be attached. (III) A small trench is cut into the longer leg to ensure a proper placement of the gripper during testing. Relevant dimensions of the sample are marked in detail (v.3): the crack length a, the height of the loaded leg $t1$ and the height of the shortened leg $t2$. The dimensions of the final samples were measured by means of a SEM and are listed in Tab. C.A.1. The length of the thinned section is about twice the length of the crack length to ensure enough space for a crack propagation under constant geometrical conditions. The laser parameters for the three processing steps are

Sample No.	Crack-length a [μm]	Thick-ness b [μm]	Height $t1$ [μm]	Height $t2$ [μm]	Clamp length c [μm]
Wires					
1	477	39	86	64	1190
2	458	59	70	80	1140
3	496	44	79	71	1400
Foils					
4	535	47	34	66	1380
5	500	53	46	54	1215
6	546	36	39	61	1110

Table C.A.1 The characteristic dimensions of the six in-situ tested samples: the initial crack length a on the SEM observed side, the thickness at the notch b, the height $t1$ of the loaded leg and the height $t2$ of the second leg. The dimensions are indicated in Fig. C.3 and Fig. C.A.1b.

listed in Tab. C.A.2. The fluence describes the energy density of the fs-laser pulse.

Processing step	1 & 2	3 (I-III)
Fluence [J/cm^2]	1.31	0.98
Pulse rep. rate [kHz]	25	10
Scan speed [mm/s]	3	1
Scan repetitions	100	40
Processing time [min]	≈ 10 each	≈ 3

Table C.A.2 Parameters used in the fs-laser processing steps depicted in Fig. C.A.1 and the total processing time for each step.

The scan repetitions state how often each scan pattern is repeated. In addition the processing time for each step is shown.

The final step of the sample processing is the introduction of a sharp notch using the FIB. The notch was introduced in a two step process using the line-milling mode. An acceleration voltage of 30 kV was used for all milling steps. For the first coarse step a current of 1 nA was used and for the second, fine step the current was reduced to 100 pA. This procedure is a standard technique of introducing cracks in micro-samples [39].

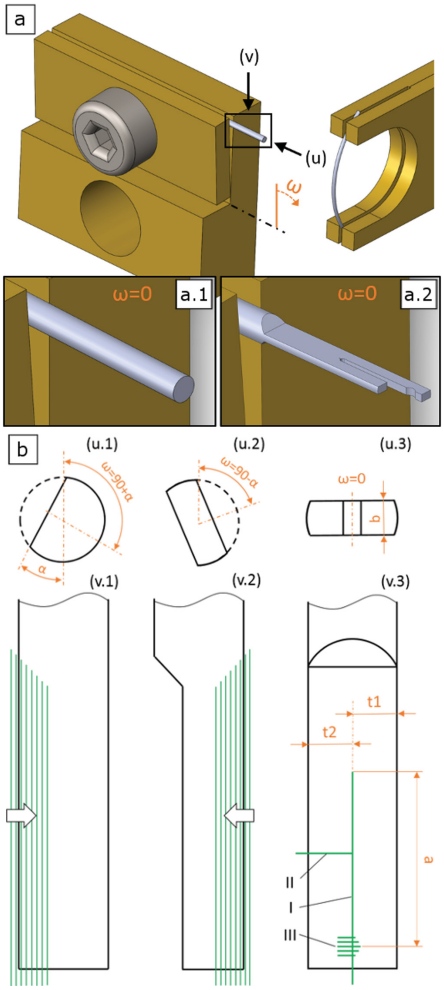

Figure C.A.1 (a) Exemplary sketch of a mounted wire sample. The direction of the tilting angle ω and the respective tilting axis are indicated (the shown orientation of the specimen holder corresponds to $\omega = 0$). The rectangular insets show the sample prior to the processing (a.1) and in its final form (a.2). (u) and (v) indicate the viewing directions for the processing steps sketched in (b). The viewing direction (v.1-3) includes the laser scan patterns. In (u.1-3) the samples are shown in the state after the respective laser processing step. In the first processing step the clamp is tilted to $\omega = 90 + \alpha$. α is the resulting taper angle of the fs-laser processed surface. In the second step the clamp is tilted to $\omega = 90 - \alpha$. To process the SLB geometry the sample is tilted to the starting position $\omega = 0$. In the next step the laser pattern consists of three elements - I.) a single line scan for the notch introduction - II.) shortening of one cantilever leg - III.) introduction of a trench to ensure a proper positioning of the loading wire. Additionally in (u.3) and (v.3) relevant sample dimension are indicated. Furthermore, in (a) the gripper for the loading is displayed on the right side.

Appendix C.B

In Sec. C.3 the onset of an early initial crack growth for sample no. 2 is mentioned. This initial crack does not commence from the notch introduced via FIB (see Fig. C.B.1). The development of this crack can most probably be connected to a pre-existing defect close to the sample surface, which leads to the crack opening due to a local higher initial stress field at this point. Nevertheless, the critical crack leading to the final failure of the sample formed at significant higher load values in front of the notch tip. The point of the first formation of the critical crack was the one considered as first crack extension and therefore for the evaluation of the stress intensity factor the respective crack length and load at the critical crack formation was used.

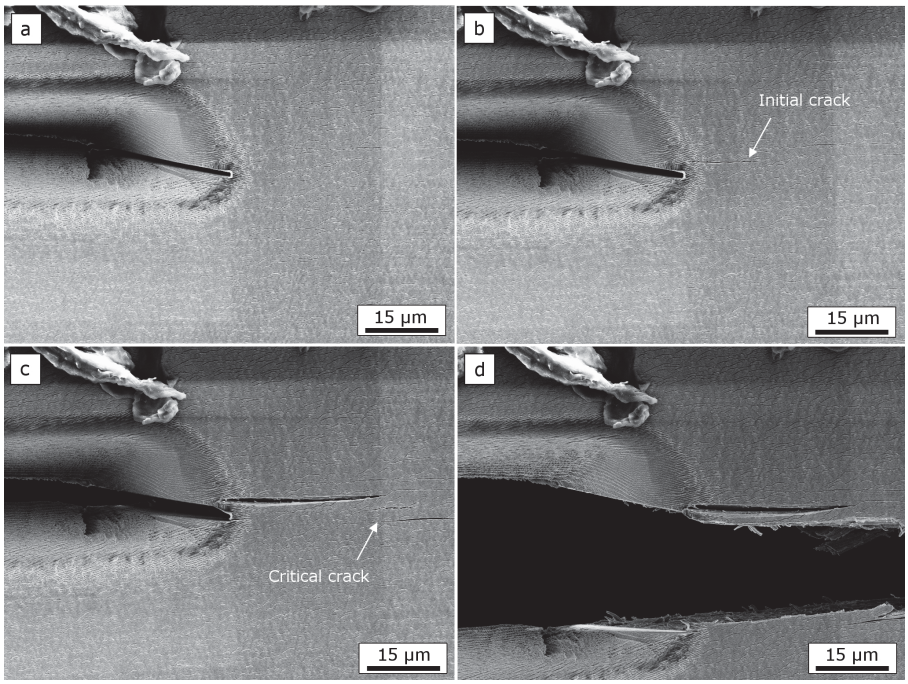

Figure C.B.1 The crack propagation of sample no. 2 during the loading process. (a) The SEM micrograph shows the notch tip of the sample prior to loading. (b) The initially observed crack does not commence from the FIB notch. (c) Further increase of the load leads to a further opening of the initial crack and also the formation of a second crack in front of the notch tip. (d) This second crack determines the location of the final failure of the specimen, whereas the initial crack is still visible on the upper leg. Only the critical crack growth was considered in the K_I evaluation.

Supplementary information to publication C

Finite element simulation

In order to describe the stress-strain fields at the vicinity of the crack front and the corresponding local k_I, k_{II} and k_{III}, several FE simulations were performed with the use of Abaqus CAE 2016 code. Each specimen was modelled as a two-stage simulation consisting of the global model representing the whole specimen and the sub-model for an evaluation of the precise stress-strain fields around the crack tip.

For the global model, each specimen type was modelled according to specimen shape and dimensions (see Fig. A.1. and Tab. 1), whereas few simplifications on the geometry were used. At first, the cross-section of the specimen was assumed to be ideally rectangular with the dimensions $b \times (t1 + t2)$ along the whole specimen length, whereas in reality the specimen becomes thicker in the unprocessed area (see Fig. A.1.). This means that the whole model is thinned-down to the thickness b, which reduces the modelling and computational time, but since this changes only the specimen stiffness far away from the area of interest, it does not influence the important results such as the occurring stress intensity factors (K-values). The second difference lies in the simplification of the rough fs-laser notch. The taper of the notch flanks (see Fig. 3) was neglected in the simulations and the mean value of the notch width was used instead along the whole specimen thickness. Contrary to this, the notch root taper (also visible in the Fig. 3(b)) was introduced to the simulations. The last geometrical assumption is connected to the sharp FIB notch forming the pre-crack. From the simulation point of view this notch was modelled as an ideal, sharp crack. The overall crack length and the crack tip shape of all specimens changed during loading in each simulation. These changes included the extension of the crack length and change of the crack front inclination (the initial pre-crack front was inclined at the same angle as was the taper angle of the fs-laser notch root but during the crack propagation, it was assumed that the crack front inclination vanished).

For the boundary conditions of the global model, one end of the specimen was fixed in all directions (see Fig. C.S.1) to simulate the rigid clamping of the real experimental setup. The loading of the specimen was performed via the point force loading on the other end of the specimen. The actual force magnitudes in simulations were used according to the experimental measurements. To correctly model the experimental loading by a thin wire (see Fig. 4(a)), all nodes along the force-loaded line were coupled to move together in the y-direction.

The global model was then discretized by approximately 600 thousand linear hexahedral elements of the type C3D8R (see [40]). As a material model only the linear-elastic material properties were assumed to mimic the W material behaviour. The used material parameters for W were a Young's modulus E of 405 GPa and a

Poisson ratio ν of 0.28 [3].

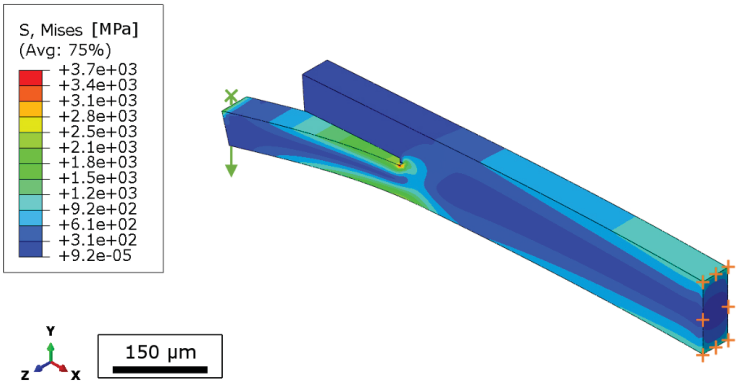

Figure C.S.1 Example of the global model of one particular specimen. The overall geometry corresponds to the real specimens, the loading force is applied at the tip of the longer leg (indicated by a green cross and arrow) and via coupling condition it is applied onto the corresponding edge of the model. The rigid fixation of the other side of the model is represented by the orange markers on the right side of the model. The overall deformation and equivalent (von-Mises) stress field in the loaded state are displayed. The showed deformation is exaggerated, the stress evolution clearly shows the need for more refinement in the area of the notch root and the crack tip itself, thus the sub-modelling procedure is justified.

Results obtained from the global model were precise enough to describe the deflection and stress evolution of the specimen as a whole, also the deflection of the model corresponded well with the initial presumptions and experimental data, but it was not sufficient to evaluate the local k-values along the crack front. For this case a sub-modelling procedure was adopted. A sub-model in general represents a small portion of the whole model and it can be meshed with a finer FE mesh and it can include some geometrical micro-changes which could not be modelled at the global model stage.

In our case the sub-model represented a small area around the crack tip. For all simulations, depending on the crack length, the general shape of the sub-model varied between a small cylinder around the crack front to box-like model cut out of the global model. For the shortest crack lengths the cylindrical shape is modelled due to the use of optimal boundary conditions in this case. The crack and notch shapes were identical as the corresponding features in the global model but its volume was meshed with a much finer FE mesh - approximately 500 thousand linear hexahedral elements of type C3D8R [40] for the smaller cylindrical sub-model and 750 thousand elements (linear hexahedral elements of type C3D8R and quadratic tetrahedral elements of type C3D10 at the ratio of 3:1) for the larger rectangular sub-model.

As a boundary condition the displacement field obtained from the corresponding global model was interpolated on the cut-faces on the sub-model which is a valid and widely used type of sub-modelling procedure. The material properties were kept the same as for the global model.

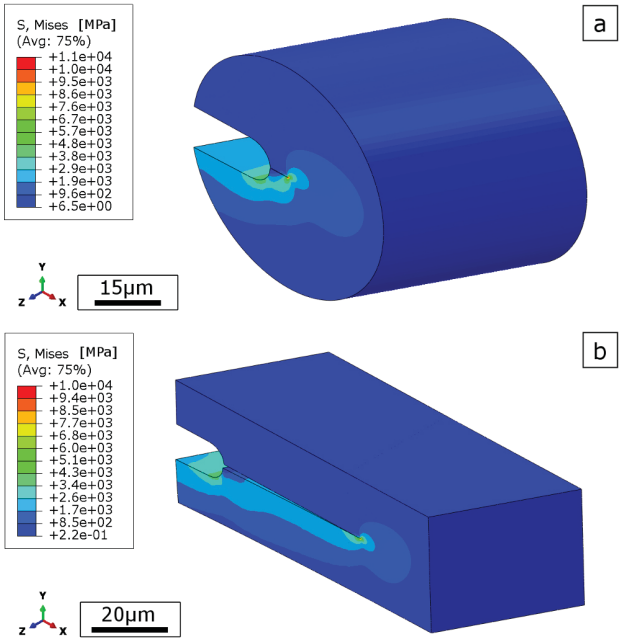

Figure C.S.2 Sub-model with plotted equivalent (von-Mises) stress: (a) circular type for the cases with shorter, inclined cracks, (b) box-like sub-model for the cases with larger crack length and a crack front perpendicular to the crack propagation direction.

Examples of both types of sub-models are shown in Fig. C.S.2 and one can clearly see that due to the higher mesh resolution the evaluated stress fields are much more precise than one obtained from the global model (Fig. C.S.1). The actual K-values along the crack fronts were evaluated using the Abaqus built-in procedure - the contour integration method. This method is based on the original J-integral approach [41] and a so-called interaction integral, which is only adapted for a numerical integration. This numerical integration is performed on specific integration paths around a point at the crack tip. Due to the numerical and FE basis of the calculation, the stress-strain singularity is not well described at the crack tip exact position, thus the first one or two integration contours are usually discarded, but for well constructed models the other integration contours should be path-independent, the same way as the original J-integral [41] (for an exact description of the contour integral method and the use of interaction integral see e.g. Abaqus detailed specifications [40] or the work of Matthew et al. [42]). From these contours Abaqus procedures evaluates the

J-integral value and it is then transformed to three k_I, k_{II} and k_{III} components [40]. The contour integration for our models was performed on each mesh node along the crack front. Only the nodes at the sides (free surfaces) of the models were excluded from the results evaluation due to observed numerical instabilities of the contour integration at the place of the free surface.

Stiffness compatibility

The verification of the overall stiffness compatibility of the model and experimental procedure was conducted by comparing CMOD and displacement data during loading process. During the in-situ experimental procedure, the CMOD was measured 100 μm behind of the initial notch tip (see Fig.4). The same procedure was replicated during the corresponding simulations.

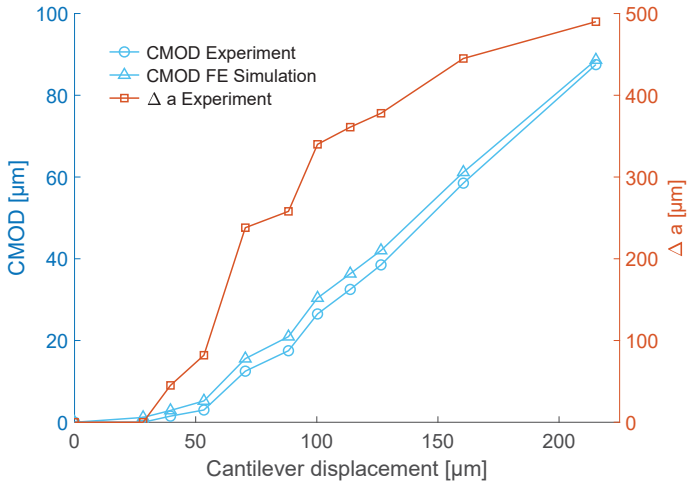

Figure C.S.3 The stiffness compatibility of the actual experimental and the modelled setup is verified by the comparison of the CMOD versus cantilever displacement curves for both cases. Further indicated is the respective crack elongation Δa. The data displayed here depicts sample no. 5.

The simulation CMOD was evaluated via the distance in y-direction of nodes located 100 μm behind of the crack tip on the sides of the modelled notch during the loading of the model. Actual values of CMOD were evaluated on the global models of respective simulation only, the more precise submodel was not used due to its small dimensions (less than 100 μm, therefore the CMOD position was not included in the submodel), but the evaluated CMOD should not be affected by this fact. This procedure was repeated for all models of the in-situ experiments (where the CMOD data were available) in several steps. In each step the loading force was increased according to its experimentally measured value and the crack lengths were

extended appropriately. This procedure enabled to model each crack propagation step and to obtain comparable CMOD values (with identical loading conditions and crack length as in the experiments).

An exemplary comparison of experimental and simulated CMOD exhibits clearly that the modelled data are almost identical with the experimental measurement (Fig. C.S.3). The slight difference can be explained by the geometrical simplifications in the numerical model. These simplifications could affect the model stiffness, but overall, the difference between model and experiment is negligible. This further validates the use of the created FE model and its compatibility with performed experiments. Qualitatively, the same results were obtained for the all in-situ tested samples.

Analytical formula for stress intensity factors

The evaluation of the stress intensity factors for SLB specimens was performed according to Davidson et al. [24]. In Fig. C.S.4 a sketch of a SLB specimen including the acting forces is shown. Additionally, the nomenclature of relevant quantities is displayed: t_1 is the height of the loaded leg, t_2 the height of the second leg and a is the initial notch length.

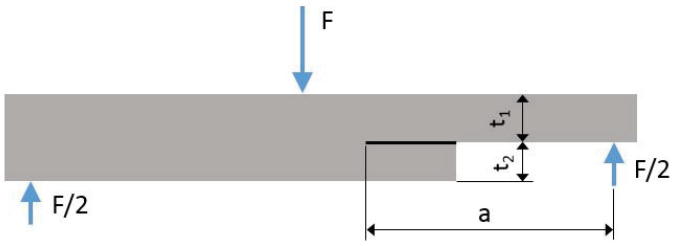

Figure C.S.4 Sketch of a SLB specimen in the loaded state including the parameter nomenclature.

The analytical formula in [24] was derived for delamination at a bimaterial interface by means of SLB experiments. The elastically isotropic and homogeneous tungsten material of the present samples does not need to consider different elastic moduli and the formula can be simplified. Therefore, the required parameters read as

$$D = \frac{E}{12}\left[t_1\left(t_1^2 + 3\,t_2^2\right) + t_2\left(t_2^2 + 3\,t_1^2\right)\right], \tag{C.S.1}$$

$$c_1 = \frac{4}{E\,t_1} + \frac{4}{E\,t_2}, \qquad c_2 = \frac{12}{E\,t_1^3} + \frac{12}{E\,t_2^3}, \tag{C.S.2}$$

$$c_{12} = \frac{6}{E\,t_2^2} - \frac{6}{E\,t_1^2}, \tag{C.S.3}$$

$$\Gamma = \sin^{-1}\left(\frac{c_{12}}{\sqrt{c_1\,c_2}}\right). \tag{C.S.4}$$

where E is the elastic modulus. The moment per unit width at the crack tip reads as

$$M = \frac{F\,(a + \Delta a_i)}{2\,b}, \tag{C.S.5}$$

where b depicts the sample width, F the maximum load prior to a crack extension and a respectively Δa_i the notch length and the crack extension. Further we need

$$a_{12} = -E\,t_1\,\frac{t_2}{2}\,\frac{1}{D}, \quad a_{22} = \frac{E\,t_1^3}{12}\,\frac{1}{D}, \tag{C.S.6}$$

and

$$N_c = a_{12}\,M, \qquad M_c = M + \left(\frac{a_{12}\,t_1}{2} - a_{22}\right)M. \tag{C.S.7}$$

The stress intensity factors for mode I and II finally read as follows

$$K_I = \sqrt{\frac{E}{2}}\,\left[-N_c\,\sqrt{c_1}\,\sin(\widehat{\Omega}) + M_c\,\sqrt{c_2}\,\cos(\widehat{\Omega} + \Gamma)\right], \tag{C.S.8}$$

$$K_{II} = \sqrt{\frac{E}{2}}\,\left[N_c\,\sqrt{c_1}\,\cos(\widehat{\Omega}) + M_c\,\sqrt{c_2}\,\sin(\widehat{\Omega} + \Gamma)\right]. \tag{C.S.9}$$

The mode mix parameter $\widehat{\Omega}$ for homogeneous and isotropic materials is given by [27]

$$\widehat{\Omega} = 23.529\,\eta - 6.8406\,\eta^3 + 1.0706\,\eta^5, \tag{C.S.10}$$

$$\text{with } \eta = \log\left(\frac{t_2}{t_1}\right). \tag{C.S.11}$$

Influence of the notch inclination

The inclined notch leads to an initial higher driving force on the side of the shorter crack length, trying to straighten the crack front. Therefore, the crack growth will start from the apex of this geometry. However, during the in-situ experiments the side of the longer crack length was observed, as shown in Fig. 4. The point of measurement for the initial crack lengths given in Tab. A.1 is also sketched in Fig. C.S.5a.

In order to assess the influence of the notch inclination on K_I, three different cases of a crack front with regard to geometry and position were evaluated and are displayed in Fig. C.S.5a: an inclined crack front with length a, and two vertical crack

fronts with crack lengths a and $a + \Delta a$. For these three cases the variation of the local K_I value across the sample thickness calculated via the FE model is shown in Fig. C.S.5b exemplarily for sample no. 2. For the case of the inclined notch, K_I increases significantly towards the short side of the notch, varying from about 2 to 9 MPa$\sqrt{m}$. However, the vertical crack fronts show the expected symmetric progress, with decreasing values towards the free surfaces of the model due to an increasing contribution of plane stress state. The mean value of each K_I curve is indicated by horizontal lines. The mean value for the inclined notch at crack initiation corresponds to the listed K_{Ii-Si} values in Tab. 2, which yield reasonable results in comparison with the analytical solution using the initial crack length. In the case of sample no. 2 the straight notch with the initial crack length yields an about 8% higher mean K_{Ii} value than for the inclined notch. A notch with a vertical front and a length of a_{short} (the point of the shortest notch length indicated in Fig. C.S.5a) leads to an about 2% higher mean K_{Ii} value than for the inclined notch. Hence, the influence of the inclined notch on the resulting K_{Ii} values is in a negligible range.

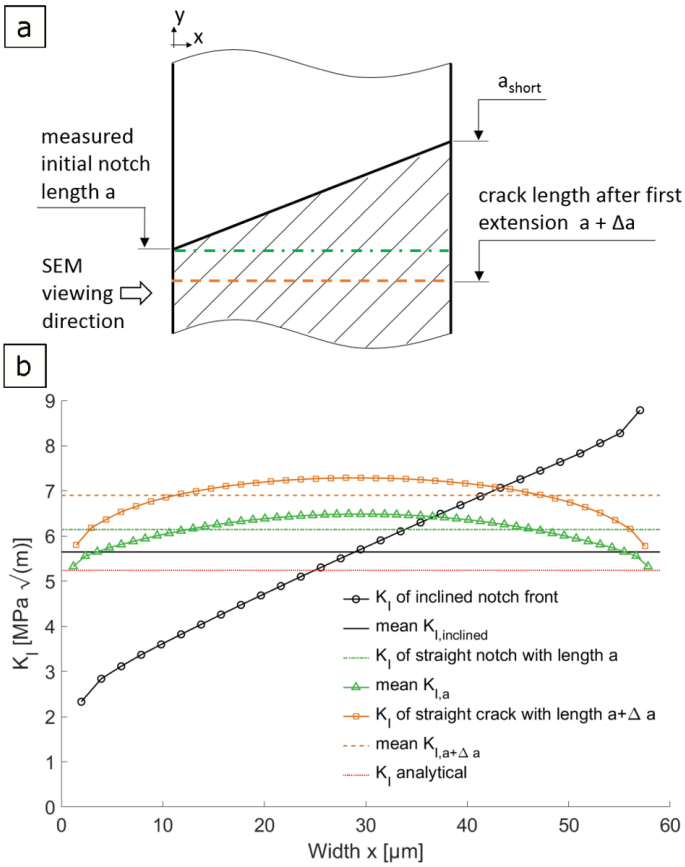

Figure C.S.5 (a) The sketch of the cross-section around the notch front displays an inclined notch with the measured initial crack length a. Further indicated are a straight notch front with the same crack length as the inclined notch front and the position of the notch front after the first crack extension Δa. After the first crack extension the front is assumed to be perpendicular to the sample surface. (b) The diagram shows the K_I value progress across the sample thickness for this three cases exemplarily for sample no.2. Additionally each mean value as well as the analytical result are indicated by horizontal lines.

Bibliography to publication C

[1] M. Rieth, S. Dudarev, S. G. de Vicente, J. Aktaa, T. Ahlgren, S. Antusch, D. Armstrong, M. Balden, N. Baluc, M. F. Barthe, W. Basuki, M. Battabyal, C. Becquart, D. Blagoeva, H. Boldyryeva, J. Brinkmann, M. Celino, L. Ciupinski, J. Correia, A. D. Backer, C. Domain, E. Gaganidze, C. García-Rosales, J. Gibson, M. Gilbert, S. Giusepponi, B. Gludovatz, H. Greuner, K. Heinola, T. Höschen, A. Hoffmann, N. Holstein, F. Koch, W. Krauss, H. Li, S. Lindig, J. Linke, C. Linsmeier, P. López-Ruiz, H. Maier, J. Matejicek, T. Mishra, M. Muhammed, A. Muñoz, M. Muzyk, K. Nordlund, D. Nguyen-Manh, J. Opschoor, N. Ordás, T. Palacios, G. Pintsuk, R. Pippan, J. Reiser, J. Riesch, S. Roberts, L. Romaner, M. Rosiński, M. Sanchez, W. Schulmeyer, H. Traxler, A. Ureña, J. van der Laan, L. Veleva, S. Wahlberg, M. Walter, T. Weber, T. Weitkamp, S. Wurster, M. Yar, J. You, and A. Zivelonghi, "Recent progress in research on tungsten materials for nuclear fusion applications in europe," *Journal of Nuclear Materials*, vol. 432, no. 1, pp. 482 – 500, 2013.

[2] C. Linsmeier, M. Rieth, J. Aktaa, T. Chikada, A. Hoffmann, J. Hoffmann, A. Houben, H. Kurishita, X. Jin, M. Li, A. Litnovsky, S. Matsuo, A. von Müller, V. Nikolić, T. Palacios, R. Pippan, D. Qu, J. Reiser, J. Riesch, T. Shikama, R. Stieglitz, T. Weber, S. Wurster, J.-H. You, and Z. Zhou, "Development of advanced high heat flux and plasma-facing materials," *Nuclear Fusion*, vol. 57, no. 9, p. 092007, 2017.

[3] E. Lassner and W. D. Schubert, *Tungsten: Properties, Chemistry, Technology of the Element, Alloys, and Chemical Compounds*. Springer US, 1999.

[4] C. Ren, Z. Fang, M. Koopman, B. Butler, J. Paramore, and S. Middlemas, "Methods for improving ductility of tungsten - a review," *International Journal of Refractory Metals and Hard Materials*, vol. 75, pp. 170 – 183, 2018.

[5] J. Reiser, L. Garrison, H. Greuner, J. Hoffmann, T. Weingärtner, U. Jäntsch, M. Klimenkov, P. Franke, S. Bonk, C. Bonnekoh, S. Sickinger, S. Baumgärtner, D. Bolich, M. Hoffmann, R. Ziegler, J. Konrad, J. Hohe, A. Hoffmann, T. Mrotzek, M. Seiss, M. Rieth, and A. Möslang, "Ductilisation of tungsten (w): Tungsten laminated composites," *International Journal of Refractory Metals and Hard Materials*, vol. 69, pp. 66 – 109, 2017.

[6] J. Riesch, T. Höschen, C. Linsmeier, S. Wurster, and J.-H. You, "Enhanced toughness and stable crack propagation in a novel tungsten fibre-reinforced tungsten composite produced by chemical vapour infiltration," *Physica Scripta*, vol. 2014, no. T159, p. 014031, 2014.

[7] B. Jasper, S. Schoenen, J. Du, T. Höschen, F. Koch, C. Linsmeier, R. Neu, J. Riesch, A. Terra, and J. Coenen, "Behavior of tungsten fiber-reinforced tungsten based on single fiber push-out study," *Nuclear Materials and Energy*, vol. 9, pp. 416 – 421, 2016.

[8] J. Riesch, M. Aumann, J. Coenen, H. Gietl, G. Holzner, T. Höschen, P. Huber, M. Li, C. Linsmeier, and R. Neu, "Chemically deposited tungsten fibre-reinforced tungsten the way to a mock-up for divertor applications," *Nuclear Materials and Energy*, vol. 9, pp. 75 – 83, 2016.

[9] M. Faleschini, H. Kreuzer, D. Kiener, and R. Pippan, "Fracture toughness investigations of tungsten alloys and spd tungsten alloys," *Journal of Nuclear Materials*, vol. 367-370, pp. 800 – 805, 2007. Proceedings of the Twelfth International Conference on Fusion Reactor Materials.

[10] Q. Wei, T. Jiao, K. Ramesh, E. Ma, L. Kecskes, L. Magness, R. Dowding, V. Kazykhanov, and R. Valiev, "Mechanical behavior and dynamic failure of high-strength ultrafine grained tungsten under uniaxial compression," *Acta Materialia*, vol. 54, no. 1, pp. 77 – 87, 2006.

[11] Q. Wei and L. Kecskes, "Effect of low-temperature rolling on the tensile behavior of commercially pure tungsten," *Materials Science and Engineering: A*, vol. 491, no. 1, pp. 62 – 69, 2008.

[12] B. Gludovatz, S. Wurster, A. Hoffmann, and R. Pippan, "Fracture toughness of polycrystalline tungsten alloys," *International Journal of Refractory Metals and Hard Materials*, vol. 28, no. 6, pp. 674 – 678, 2010. Selected papers of the 17th International Plansee Seminar 2010 in Reutte, Austria: Tungsten and Molybdenum.

[13] D. Rupp and S. Weygand, "Anisotropic fracture behaviour and brittle-to-ductile transition of polycrystalline tungsten," *Philosophical Magazine*, vol. 90, no. 30, pp. 4055–4069, 2010.

[14] J. Riesch, A. Feichtmayer, M. Fuhr, J. Almanstötter, J. W. Coenen, H. Gietl, T. Höschen, C. Linsmeier, and R. Neu, "Tensile behaviour of drawn tungsten wire used in tungsten fibre-reinforced tungsten composites," *Physica Scripta*, vol. T170, p. 014032, oct 2017.

[15] J. Reiser, M. Rieth, A. Möslang, B. Dafferner, A. Hoffmann, X. Yi, and D. Armstrong, "Tungsten foil laminate for structural divertor applications tensile test properties of tungsten foil," *Journal of Nuclear Materials*, vol. 434, no. 1, pp. 357 – 366, 2013. Special Section on Spent Nuclear Fuel.

[16] V. Nikolić, S. Wurster, D. Firneis, and R. Pippan, "Fracture toughness evaluation of UFG tungsten foil," *International Journal of Refractory Metals and Hard Materials*, vol. 76, pp. 214–225, Nov. 2018.

[17] V. Nikolić, J. Riesch, M. J. Pfeifenberger, and R. Pippan, "The effect of heat treatments on pure and potassium doped drawn tungsten wires: Part II Fracture properties," *Materials Science and Engineering: A*, vol. 737, pp. 434–447, Nov. 2018.

[18] I. Utke, S. Moshkalev, and P. Russell, *Nanofabrication Using Focused Ion and Electron Beams: Principles and Applications*. Oxford ; New York: Oxford University Press, new ed., Dec. 2011.

[19] M. J. Pfeifenberger, M. Mangang, S. Wurster, J. Reiser, A. Hohenwarter, W. Pfleging, D. Kiener, and R. Pippan, "The use of femtosecond laser ablation as a novel tool for rapid micro-mechanical sample preparation," *Materials & Design*, vol. 121, pp. 109–118, May 2017.

[20] S. Bonk, J. Reiser, J. Hoffmann, and A. Hoffmann, "Cold rolled tungsten (W) plates and foils: Evolution of the microstructure," *International Journal of Refractory Metals and Hard Materials*, vol. 60, pp. 92 – 98, 2016.

[21] V. Nikolić, S. Wurster, D. Firneis, and R. Pippan, "Improved fracture behavior and microstructural characterization of thin tungsten foils," *Nuclear Materials and Energy*, vol. 9, pp. 181 – 188, 2016.

[22] V. Nikolić, J. Riesch, and R. Pippan, "The effect of heat treatments on pure and potassium doped drawn tungsten wires: Part I - Microstructural characterization," *Materials Science and Engineering: A*, vol. 737, pp. 422–433, Nov. 2018.

[23] S. Bonk, J. Hoffmann, A. Hoffmann, and J. Reiser, "Cold rolled tungsten (W) plates and foils: Evolution of the tensile properties and their indication towards deformation mechanisms," *International Journal of Refractory Metals and Hard Materials*, vol. 70, pp. 124–133, Jan. 2018.

[24] B. D. Davidson and V. Sundararaman, "A single leg bending test for interfacial fracture toughness determination," *Int J Fract*, vol. 78, pp. 193–210, June 1996.

[25] J. Bonse, J. Krüger, S. Höhm, and A. Rosenfeld, "Femtosecond laser-induced periodic surface structures," *Journal of Laser Applications*, vol. 24, p. 042006, July 2012.

[26] B. Yang, C. Motz, W. Grosinger, W. Kammrath, and G. Dehm, "Tensile behaviour of micro-sized copper wires studied using a novel fibre tensile module," *IJMR*, vol. 99, pp. 716–724, July 2008.

[27] B. D. Davidson, H. Hu, and R. A. Schapery, "An Analytical Crack-Tip Element for Layered Elastic Structures," *J. Appl. Mech*, vol. 62, pp. 294–305, June 1995.

[28] K. Palaniswamy and W. G. Knauss, "II - On the Problem of Crack Extension in Brittle Solids Under General Loading," in *Mechanics Today* (S. Nemat-nasser, ed.), pp. 87–148, Pergamon, Jan. 1978.

[29] F. Erdogan and G. C. Sih, "On the Crack Extension in Plates Under Plane Loading and Transverse Shear," *J. Basic Eng*, vol. 85, pp. 519–525, Dec. 1963.

[30] R. W. Margevicius, J. Riedle, and P. Gumbsch, "Fracture toughness of polycrystalline tungsten under mode I and mixed mode I/II loading," *Materials Science and Engineering: A*, vol. 270, pp. 197–209, Sept. 1999.

[31] T. M. Maccagno and J. F. Knott, "The low temperature brittle fracture behaviour of steel in mixed modes I and II," *Engineering Fracture Mechanics*, vol. 38, pp. 111–128, Jan. 1991.

[32] R. C. Shah, "Fracture Under Combined Modes in 4340 Steel," *Fracture Analysis: Proceedings of the 1973 National Symposium on Fracture Mechanics, Part II*, Jan. 1974.

[33] T. Anderson, *Fracture Mechanics: Fundamentals and Applications, Second Edition*. Taylor & Francis, 1994.

[34] R. Pippan, S. Wurster, and D. Kiener, "Fracture mechanics of micro samples: Fundamental considerations," *Materials & Design*, vol. 159, pp. 252–267, Dec. 2018.

[35] B. Gludovatz, S. Wurster, A. Hoffmann, and R. Pippan, "A study into the crack propagation resistance of pure tungsten," *Engineering Fracture Mechanics*, vol. 100, pp. 76–85, Mar. 2013.

[36] J. Pokluda, P. Šandera, and J. Horníková, "Statistical approach to roughness-induced shielding effects," *Fatigue & Fracture of Engineering Materials & Structures*, vol. 27, no. 2, pp. 141–157, 2004.

[37] S. Žák, J. Horníková, P. Šandera, T. Vojtek, M. Kianicová, and J. Pokluda, "Local and equivalent stress intensity factors for tortuous cracks under remote mode II loading," *Theoretical and Applied Fracture Mechanics*, vol. 101, pp. 35–45, 2019.

[38] S. Žák, J. Horníková, and P. Šandera, "Stress intensity factors for rough cracks loaded in mode II," *Solid State Phenomena*, vol. 258, pp. 310–313, Jan. 2017.

[39] S. Wurster, C. Motz, and R. Pippan, "Characterization of the fracture toughness of micro-sized tungsten single crystal notched specimens," *Philosophical Magazine*, vol. 92, pp. 1803–1825, May 2012.

[40] "Abaqus analysis user's manual," *Dassault Systems Simulia Corp, Johnston, RI, USA*, vol. 2016.

[41] J. R. Rice, "A Path Independent Integral and the Approximate Analysis of Strain Concentration by Notches and Cracks," *J. Appl. Mech*, vol. 35, pp. 379–386, June 1968.

[42] M. C. Walters, G. H. Paulino, and R. H. Dodds, "Interaction integral procedures for 3-D curved cracks including surface tractions," *Engineering Fracture Mechanics*, vol. 72, pp. 1635–1663, July 2005.